Regeneration of iron fuel in fluidized beds

Regeneration of iron fuel in fluidized beds

Xin Liu

Regeneration of iron fuel in fluidized beds
by Xin Liu
Dissertation, Technische Universiteit Eindhoven, 2023

A catalogue record is available from the Eindhoven University of Technology Library.

ISBN: 978-90-386-5662-5
Cover design by Xin Liu
Printed by ADC Nederland

Regeneration of iron fuel in fluidized beds

PROEFSCHRIFT

ter verkrijging van de graad van doctor
aan de Technische Universiteit Eindhoven,
op gezag van de rector magnificus prof.dr.ir. F.P.T. Baaijens,
voor een commissie aangewezen door het College voor Promoties,
in het openbaar te verdedigen op dinsdag 7 februari 2023 om 13:30 uur

door

Xin Liu

geboren te Xi'an, China

Dit proefschrift is goedgekeurd door de promotoren en de samenstelling van de promotiecommissie is als volgt:

voorzitter:	prof.dr.ir. P. D. Anderson
promotor:	prof.dr.ir. N. G. Deen
copromotor:	dr. Y. Tang
leden:	prof.dr. Y. He (Harbin Institute of Technology)
	Prof. Dr.-Ing. habil. S. Heinrich (Technische Universität Hamburg)
	Prof. Dr. S. Pirker (Johannes Kepler Universität Linz)
	prof.dr.ir. M. van Sint Annaland

Het onderzoek of ontwerp dat in dit proefschrift wordt beschreven is uitgevoerd in overeenstemming met de TU/e Gedragscode Wetenschapsbeoefening.

To my parents

Contents

Summary

Regeneration of iron fuel in fluidized beds

Iron powder is a sustainable, carbon-neutral fuel as it offers multiple advantages over other clean energy storage media, including ease of transportation, storage, and higher energy density. Iron fuels combust, i.e., they react energetically with oxygen in air releasing a huge amount of heat. The resulting iron oxides can be collected and reduced back to iron powder closing the iron fuel cycle. To fulfill a carbon-neutral fuel cycle, regeneration of the metallic iron from the combustion product (iron oxides) using renewable energy (e.g. green hydrogen) is crucial. Direct reduced iron (DRI) using renewable energy (e.g. green hydrogen) using fluidized bed technology has been primarily considered. However, agglomeration of fine powder at elevated temperatures is one key issue hindering technological development. Better understanding the agglomeration/sintering phenomenon of iron/iron oxide particles in a fluidized bed is an essential step towards the technological development of direct iron reduction in the metal fuel cycle. Therefore, in this dissertation, the (de-)fluidization and the reduction of micron-sized combusted iron powder are studied.

The (de-)fluidization behavior of micron-sized combusted iron particles is first experimentally studied. Effects of temperature, gas flow rate, and particle size on the fluidization and agglomeration behavior are investigated. Different fluidization regimes (e.g. stable fluidization, unstable fluidization, fast defluidization) are categorized. Transitions between stable fluidization, unstable fluidization, and defluidization have been identified and are characterised by two critical temperatures: the transition temperature (T_t) and the defluidization temperature (T_d). These critical temperatures are found almost insensitive to the gas flow rate but they highly depend on the particle size.

Based on the outcome of the defluidization study, reduction experiments of micron-sized combusted iron powders using hydrogen are subsequently conducted at temperature of $500-650\,^{\circ}C$. Effects of temperature, hydrogen velocity and concentration on the reduction performance and sintering/defluidization behavior are investigated. Overall, a reduction degree higher than 90% is reached at a lower temperature of $500\,^{\circ}C$ whereas at higher temperatures severe particle sintering is encountered, which leads to quick defluidization and thus a relatively low reduction degree. These experimental findings provide insights for the design of the industrial process of hydrogen-based regeneration of iron fuels.

To obtain a better understanding of the fluidization/agglomeration phenomenon inside a fluidized bed, the (de-)fluidization/agglomeration behavior of micron-sized iron oxide particles in a 3D fluidized bed using Computational Fluid Dynamics coupled with Discrete Element Method (CFD-DEM) is subsequently investigated. Agglomeration usually occurs at elevated temperatures, where heat transfer plays a critical role. Therefore, before concentrating on the sintering/agglomeration study, it is necessary to properly model the

heat transfer inside the bed, particularly the heat exchange through confining walls due to the large temperature gradient in the thin thermal boundary layer. Thus, two approaches are adopted and compared in detail to study such heat transfer near the confining walls in fluidized beds, i.e., by imposing a thermal boundary condition for the gas phase thermal energy equation and by implementing a particle-wall conduction model for the discrete particle phase. It is found that the latter method provides the best description.

With confidence in the heat transfer study, the (de-)fluidization behavior of micron-sized iron oxide particles in a 3D fluidized bed is finally investigated using CFD coupled with coarse-grained DEM (CFD-cgDEM). The temperature-dependent solid bridge force is considered as the cohesive force. The cgDEM model is first verified by comparing the results at different scaling factors with experimental observations. Subsequently, effects of temperature on the bed dynamics are investigated. In conclusion, the developed model shows the capacity to reliably predict particle agglomeration behavior, which can shed light on the design of the DRI process in high-temperature fluidized beds.

This thesis reports an experimental and numerical modeling study focused on direct iron reduction in the metal fuel cycle, the findings of which are crucial for closing the iron fuel cycle. The work provides insights in the design of the industrial process of hydrogen-based regeneration of iron fuels. Furthermore, it brings new insights to dense energy carrier research for future storage and transport of renewable energy.

Samenvatting

Regeneratie van ijzerbrandstof in wervelbedden

IJzerbrandstof is een duurzame, koolstofneutrale brandstof die meerdere voordelen biedt ten opzichte van andere duurzame energie opslagmethodes, zoals gemakkelijk vervoer en opslag, en een hoge energiedichtheid. IJzerbrandstoffen reageren energetisch met zuurstof in de lucht, waarbij een enorme hoeveelheid warmte vrijkomt. Het resulterende ijzeroxide poeder kan worden opgevangen en teruggebracht tot ijzerpoeder, waarmee de cyclus van ijzerbrandstoffen wordt volbracht. Voor een koolstofneutrale brandstofcyclus is regeneratie van het metallisch ijzer uit het verbrandingsproduct (ijzeroxide poeder) met behulp van duurzame energie (bv. groene waterstof) van cruciaal belang. Voornamelijk direct gereduceerd ijzer (DRI) met behulp van duurzame energie (bv. groene waterstof) op basis van wervelbedtechnologie is onderzocht. Agglomeratie van fijn ijzer poeder bij hoge temperatuur is echter een belangrijk probleem dat de technologische ontwikkeling belemmert. Een beter begrip van het agglomeratie/sintering gedrag van ijzer/ijzeroxidedeeltjes in een wervelbed is essentieel voor de technologische ontwikkeling van directe ijzerreductie in de metaalbrandstofcyclus. Daarom worden in dit proefschrift de (de-)fluïdisatie en de reductie van fijn verbrand ijzerpoeder bestudeerd.

Het (de-)fluïdisatiegedrag van microngrootte verbrande ijzerdeeltjes is eerst experimenteel bestudeerd. Effecten van temperatuur, gasstroom en deeltjesgrootte op het fluïdisatie- en agglomeratiegedrag zijn onderzocht. Verschillende fluidizatie-regimes (bv. stabiele fluïdisatie, onstabiele fluïdisatie, snelle defluïdisatie) zijn gecategoriseerd. Overgangen tussen stabiele fluïdisatie, onstabiele fluïdisatie en defluïdisatie zijn geïdentificeerd met behulp van twee bijbehorende kritische temperaturen: de overgangstemperatuur (T_t) en de defluïdisatietemperatuur (T_d). Deze kritische temperaturen zijn vrijwel ongevoelig voor de gasstroom, maar hangen sterk af van de deeltjesgrootte.

Op basis van de resultaten van de defluïdisatiestudie zijn vervolgens reductie-experimenten uitgevoerd voor micrometer-formaat verbrand ijzerpoeder met waterstof bij temperaturen van $500-650\,^{\circ}C$. De effecten van temperatuur, waterstofsnelheid en concentratie op de reductieprestaties en het sinter-/defluidisatiegedrag zijn onderzocht. In het algemeen wordt een reductiegraad van meer dan 90% bereikt bij een lagere temperatuur van $500\,^{\circ}C$, terwijl bij hogere temperatuur sintering van de deeltjes optreedt, wat leidt tot snelle defluïdisatie en daardoor een relatief lage reductiegraad. Deze experimentele bevindingen bieden inzichten voor het ontwerp van het industriële proces van regeneratie van ijzerbrandstoffen op basis van waterstof.

Om een beter inzicht te krijgen in het fluïdisatie-/agglomeratiegedrag in een wervelbed, is het (de-)fluïdisatie-/agglomeratiegedrag van ijzeroxidedeeltjes van micrometer-formaat in een 3D wervelbed numeriek onderzocht met behulp van “Computational Fluid Dynamics" gekoppeld aan de “Discrete Element Method" (CFD-DEM). Agglomeratie treedt voornamelijk op bij hoge temperatuur, waarbij warmteoverdracht een kritische rol speelt.

Daarom is het noodzakelijk de warmteoverdracht in het bed goed te modelleren, voordat men zich concentreert op het bestuderen van het sinter-/agglomeratiegedrag. Met name de warmte-uitwisseling met de reactorwanden is belangrijk, als gevolg van de hoge temperatuurgradiënt in de dunne thermische grenslaag. Twee benaderingen zijn geselecteerd en in detail vergeleken om de warmteoverdracht met de reactorwanden te bestuderen: door een thermische randvoorwaarde op te leggen voor warmteoverdracht in de gasfase en door een deeltjes-wand warmtegeleidingsmodel toe te passen voor de discrete deeltjesfase. Het laatste model blijkt de beste beschrijving te geven.

Met vertrouwen in de warmteoverdrachtsstudie is uiteindelijk het (de-)fluïdisatiegedrag van micrometer-formaat ijzeroxidedeeltjes in een 3D gefluïdiseerd bed onderzocht met behulp van CFD gekoppeld aan “coarse-grained" DEM (CFD-cgDEM). De cohesie tussen de deeltjes is gemodelleerd als de temperatuursafhankelijke vaste brugkracht. Het cgDEM-model is eerst geverifieerd door de resultaten bij verschillende schaalfactoren te vergelijken met experimentele waarnemingen. Vervolgens zijn de effecten van de temperatuur op de beddynamica onderzocht. De conclusie is dat het ontwikkelde model een betrouwbare voorspelling kan geven van het agglomeratiegedrag van de deeltjes, hetgeen licht kan werpen op het ontwerp van het DRI-proces in wervelbedden op hoge temperatuur.

Dit proefschrift raporteert een experimentele en numerieke modelstudie gericht op directe ijzerreductie in de metaalbrandstofcyclus, waarvan de bevindingen cruciaal zijn voor het sluiten van de ijzerbrandstofcyclus. Het werk biedt inzicht in het ontwerp van het industriële proces van ijzerbrandstofregeneratie met behulp van waterstof. Bovendien brengt het nieuwe inzichten op het gebied van dichte energiedragers voor toekomstige opslag en transport van duurzame energie.

1

INTRODUCTION

1

1.1. Background and motivation

1.1.1. The role of metal fuels

The consumption and generation of energy are two of the most significant features of modern society. Globally, fossil fuels, such as coal, oil, and natural gas, still play a dominant part in the energy system, accounting for around 80% of the total energy supply [1, 2]. Such massive consumption of fossil fuels brings various challenges to our society. One of the most important effects is accelerating climate change [3, 4]. Even though countries worldwide have launched regulations in response to the growing concerns about traditional energy generation, unexpected situations such as the COVID-19 pandemic and geopolitical conflicts exert unprecedented shocks across the entire energy sector. Therefore, successfully transiting from traditional hydrocarbon fuel sources to sustainable carbon-free energy carriers via a safe, stable, and high-density energy storage technology is urgently required [5].

For displacing or supplementing traditional hydrocarbon fuel sources, future low-carbon energy carriers should exhibit high energy densities for convenient trade and storage, and be consumable within efficient high-power density engines for transportation, heavy machinery, and other off-grid energy applications. Metal fuels have been proposed as a promising energy carrier in the future low-carbon economy [6, 7]. On the one hand, it offers comparable energy density as hydrocarbon fuels (as shown in Figure 1.1) and safe/ease transportation; on the other hand, it meets climate mitigation goals due to zero carbon emissions.

The metal-fuel energy cycle is depicted in Figure 1.2. Metal fuels, usually in micron size, can either be reacted with water [8] or burned in air [7] to release their chemical energy. The only products, metal oxides, can be collected and reduced back to metal fuel using clean primary energy produced locally. High-density metal powders are already widely used in many aspects, for example, within chemical-looping combustion systems [9, 10], been added to propellants used in commercial or military applications [11], or been added to pyrotechnics used in fireworks demonstrations [12]. From these points of view, metal fuels are desirable alternatives, which are of great interest for scientific study.

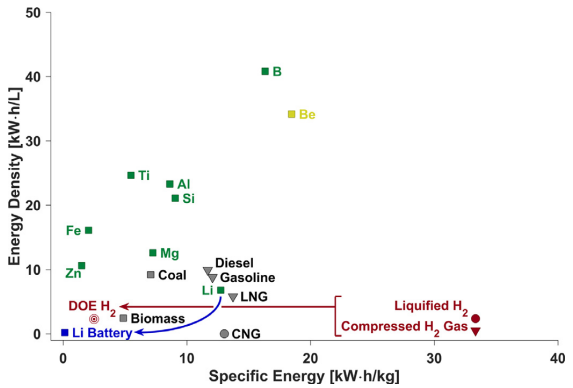

Figure 1.1: Energy density and specific energy of various metals compared with batteries, hydrogen and fossil fuels. Adapted from [13].

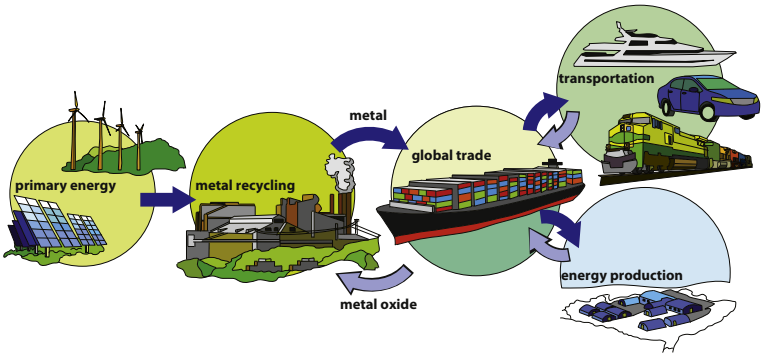

Figure 1.2: Metal fuel cycle. Adapted from [7].

1.1.2. Regeneration of iron fuel

The primary candidate fuel is considered iron as it offers multiple advantages, including i) its moderate combustion temperature minimizing the formation of nano-particles; ii) abundance and low cost of resources; iii) possible recyclability based on well-established technologies from the reduction process of iron ore; iv) high energy density (i.e. 16 kW·h/L). Thus, the energy-dense metal carrier in this thesis focuses on iron powder. In the iron-fuel cycle, iron powder reacts energetically with the oxygen in air releasing a huge amount of heat. The resulting iron oxides can be captured and reduced back to iron powder using a green reducing agent (e.g. hydrogen) generated by clean primary energy to close the iron fuel cycle.

In order to fulfill a carbon-neutral fuel cycle, regeneration of the metallic iron from the combustion product (iron oxides) using renewable energy (e.g. green hydrogen) is an essential step [14, 15]. Therefore, a fundamental understanding of the reduction mechanisms or phenomena associated with the reduction process of combusted iron powders becomes crucial. In this dissertation, the fluidization and reduction performance of micron-sized combusted iron powder in a fluidized bed are comprehensively studied, with the ultimate goal to guide the practical design of hydrogen-based direct reduction of combusted iron powders.

1.2. Gas-fluidized beds

1.2.1. The concept of using fluidized beds

Gas-fluidized bed reactors are widely employed in industry for the production or treatment of large amounts of granular materials. The movement of the gas phase and solids phase highly depends on the fluid and solid properties [16]. As shown in Figure 1.3, with increasing gas velocities, the bed exhibits distinct behavior. The gas is introduced from the bottom of the bed and moves upwards through the interstitial spaces between the particles. By increasing the gas velocity to a critical value, the drag force applied by the upwards-flowing fluid becomes equal to the weight of the particles in the bed, and the bed starts to fluidize. Such a critical point is commonly referred to as the minimum fluidization velocity (u_{mf}),

which is one of the most important parameters associated with a fluidized bed system. By further increasing the gas velocity, the granular phase shows fluid-like behavior with gas bubbles generated in the bed. At even higher gas velocity, the bed is characterized by a turbulent regime. This process is called fluidization, which is a promising technology for the thermochemical reduction of iron oxide powder due to its high fluid-solid contact efficiency, and excellent heat and mass transfer characteristics. Therefore, direct reduced iron (DRI) using renewable energy (e.g. hydrogen) based on gas-fluidized bed technologies has been primarily considered.

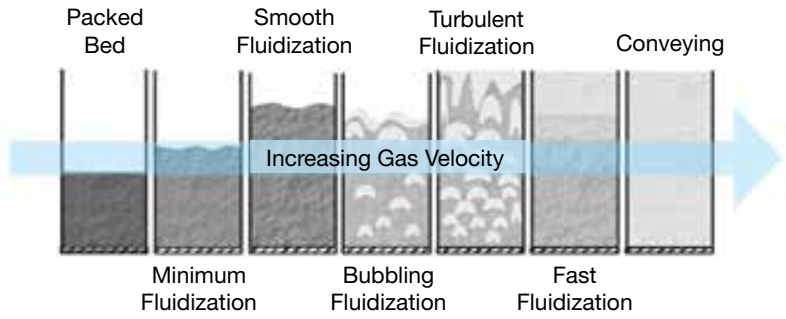

Figure 1.3: As the gas velocity through the bed increases, the type of fluidization shifts. Adapted from [17].

1.2.2. Challenges in fluidized beds

Within a gas-fluidized bed, particles are subject to gravity and drag due to the flow of gas. On top of that, particles also experience interactions with neighboring particles and/or the walls (i.e. collision forces and cohesive forces). All of these forces are relevant to fluidization behavior. Even though fluidized beds are one of the ideal reactors for metal fuel processes, fluidization of micron-sized iron oxides may encounter undesirable behavior like agglomeration/sintering and/or channelling because of particle cohesion under certain operating conditions. Such undesirable feature highly affects the fluidization regimes in the bed and possibly reduces the efficiency of the regeneration of iron fuel.

Important factors which influence the sintering issue include the physical particle properties (e.g. composition, geometry, size, and morphology), and operation conditions (e.g. reducing gas, temperature, and velocity) [18–20]. Better understanding of the agglomeration/sintering phenomenon of combusted iron particles in a fluidized bed is a crucial step towards the technological development of direct iron reduction in the metal fuel cycle.

1.3. Approaches

The main goal of this research is to obtain a detailed understanding of the phenomena (including both fluidization and reduction) during the regeneration of iron fuel. Thus, both experimental study and numerical investigation are carried out in this dissertation.

1.3.1. Experimental study

Literature studies have concentrated on the analysis of the reduction/sintering of iron ore, which possesses different characteristics from the iron/iron oxide powder applicable for the metal fuel application including particle size (μm size), morphology, and composition [21–23]. In order to better understand the phenomena associated with the reduction of iron oxide powder directly resulting from iron powder combustion, an experimental study in a lab-scale gas-fluidized bed reactor is first carried out, with the ultimate goal to guide the practical design of hydrogen-based direct reduction of combusted iron.

Two series of experiments are designed, i.e., fluidization and reduction. As such, experimental test with micron-sized iron oxide powder, produced by iron powder combustion, under N_2/H_2 atmosphere in a lab-scale fluidized bed reactor is carried out. A comprehensive study has been conducted to investigate the effect of operating parameters (including temperature, gas velocity, and particle size) on the fluidization characteristics and the reduction process.

1.3.2. Modeling strategy

Detailed Computational Fluid Dynamics coupled with the Discrete Element Method (CFD-DEM) provides a powerful tool to understand the detailed phenomena (e.g. agglomeration and reduction) in a fluidized bed [24, 25], which has been extensively used to predict and study hydrodynamics and heat transfer taking place in fluidized beds [26–28].

In the regeneration of iron fuel, the studied powders are of an average size of about 40 microns and a density of around 5000 kg/m^3, which belongs to the Geldart A group. The micron-sized cohesive iron/iron oxide powder provides a challenge for the computational simulation cost due to the very large number of particles, particularly for modeling realistic industrial processes. To reduce the number of computational entities, the so-called coarse-grained DEM (cgDEM) models have been developed [29, 30]. The concept of coarse graining is that a group of the original particles is represented by large-sized coarse-grained particles (often called “parcels"), whose behavior is kept equivalent to the original particles. This approach requires a scaling law which can ensure that the total energy of the coarse-grained parcels is equal to that of the original particles that they represent.

1.4. Outline of the thesis

The thesis consists of two main parts: 1) experimental investigation on the defluidization/agglomeration and reduction performance of combusted iron fines in a lab-scale fluidized bed reactor; 2) numerical modeling on the heat transfer and sintering/agglomeration behavior using Computational Fluid Dynamics coupled with Discrete Element Method (CFD-DEM).

In Chapter 2, the (de-)fluidization behavior of micron-sized combusted iron particles is experimentally studied. Effects of various operating and material variables (temperature, gas flow rate, and particle size) on the fluidization regimes and agglomeration behavior are investigated. A theoretical model based on a force balance is finally developed to predict the regime boundaries of fluidization. The obtained knowledge from this chapter is applied to the experimental design of the hydrogen-based iron direct reduction process

in Chapter 3.

In Chapter 3, based on the outcomes from the (de-)fluidization experimental study in Chapter 2, reduction experiments of micron-sized combusted iron powders using hydrogen in a lab-scale gas-fluidized bed are conducted at a temperature range of 500 – 650 °C. The effects of operating parameters including temperature, hydrogen velocity, and hydrogen concentration on the reduction performance (including reduction degree, particle morphology, and size change) and sintering/defluidization behavior are investigated. The reduction performance characterized by reduction degree, particle morphology, and size change is analyzed by means of a titration method, XRD, SEM, and a Particle Size Analyzer.

Chapter 4 focuses on the heat transfer modeling in a fluidized bed, particularly the heat loss from the confining walls. A comprehensive review is given on the treatments for modeling bed-to-wall heat transfer in CFD-DEM simulations. Two modeling approaches are investigated: a thermal boundary condition and particle-based conduction. Recommendation on the treatments of bed-to-wall heat transfer is finally given after a detailed comparison of both approaches.

In Chapter 5, the (de-)fluidization behavior of micron-sized iron oxide particles in a 3D fluidized bed is investigated using CFD-cgDEM. The temperature-dependent solid bridge force is considered as the dominant inter-particle cohesive force. The cgDEM model is first verified by comparing the results at different scaling factors. Subsequently, the effects of temperature and the magnitude of the solid bridge force on the bed hydrodynamics are investigated. The developed model shows its capacity for reliable prediction of particle agglomeration behavior. The obtained knowledge helps to develop strategies to counteract agglomeration in the hydrogen-based iron direct reduction and provides insights for the design of the industrial process of regeneration of iron fuels.

Finally, the main conclusions drawn from this thesis and recommendations for future work are presented in Chapter 6.

Bibliography

[1] IEA. “World Energy Outlook 2021”. In: (2021).

[2] “BP Statistical Review of World Energy 2022”. In: (2022).

[3] D. J. Wuebbles and A. K. Jain. “Concerns about climate change and the role of fossil fuel use”. In: *Fuel processing technology* 71.1-3 (2001), pp. 99–119.

[4] M. Höök and X. Tang. “Depletion of fossil fuels and anthropogenic climate change—A review”. In: *Energy policy* 52 (2013), pp. 797–809.

[5] T. Nakata, D. Silva, and M. Rodionov. “Application of energy system models for designing a low-carbon society”. In: *Progress in Energy and Combustion Science* 37.4 (2011), pp. 462–502.

[6] P. Julien and J. M. Bergthorson. “Enabling the metal fuel economy: green recycling of metal fuels”. In: *Sustainable Energy & Fuels* 1.3 (2017), pp. 615–625.

[7] J. M. Bergthorson, S. Goroshin, M. J. Soo, P. Julien, J. Palecka, D. L. Frost, and D. J. Jarvis. “Direct combustion of recyclable metal fuels for zero-carbon heat and power”. In: *Applied Energy* 160 (2015), pp. 368–382.

[8] J. M. Bergthorson, Y. Yavor, J. Palecka, W. Georges, M. Soo, J. Vickery, S. Goroshin, D. L. Frost, and A. J. Higgins. “Metal-water combustion for clean propulsion and power generation”. In: *Applied Energy* 186 (2017), pp. 13–27.

[9] T. Mattisson, A. Lyngfelt, and P. Cho. “The use of iron oxide as an oxygen carrier in chemical-looping combustion of methane with inherent separation of CO_2”. In: *Fuel* 80.13 (2001), pp. 1953–1962.

[10] H. Gu, L. Shen, J. Xiao, S. Zhang, and T. Song. “Chemical looping combustion of biomass/coal with natural iron ore as oxygen carrier in a continuous reactor”. In: *Energy & Fuels* 25.1 (2011), pp. 446–455.

[11] K. Ishitha and P. Ramakrishna. “Studies on the role of iron oxide and copper chromite in solid propellant combustion”. In: *Combustion and Flame* 161.10 (2014), pp. 2717–2728.

[12] N. Selvakumar, A. Azhagurajan, P. Sheikmohamed, and A. Suresh. “Ballistic behaviour of gun powder and flash powder for firework chemicals as a function of particle sizes”. In: *Measurement* 46.9 (2013), pp. 3202–3210.

[13] J. M. Bergthorson. “Recyclable metal fuels for clean and compact zero-carbon power”. In: *Progress in Energy and Combustion Science* 68 (2018), pp. 169–196.

[14] C. J. M. Hessels, T. A. M. Homan, N. G. Deen, and Y. Tang. “Reduction kinetics of combusted iron powder using hydrogen”. In: *Powder Technology* (2022), p. 117540.

[15] X. Liu, X. Zhang, J. Li, Q. Zhu, N. G. Deen, and Y. Tang. “Regeneration of iron fuel in fluidized beds Part II: reduction experiments”. In: *Powder Technology, (Accepted)* (2023).

[16] D. Kunii and O. Levenspiel. *Fluidization engineering*. Butterworth-Heinemann, 1991.

[17] R. Cocco, S. R. Karri, T. Knowlton, et al. "Introduction to fluidization". In: *Chem. Eng. Prog* 110.11 (2014), pp. 21–29.

[18] S. Hayashi and Y. Iguchi. "Factors affecting the sticking of fine iron ores during fluidized bed reduction". In: *ISIJ international* 32.9 (1992), pp. 962–971.

[19] Y. Zhong, Z. Wang, Z. Guo, and Q. Tang. "Defluidization behavior of iron powders at elevated temperature: Influence of fluidizing gas and particle adhesion". In: *Powder technology* 230 (2012), pp. 225–231.

[20] M. Gluckman, J. Yerushalmi, and A. Squires. "Defluidization characteristics of sticky or agglomerating beds". In: *Fluidization technology*. Vol. 2. Hemisphere Washington DC, 1976, pp. 395–422.

[21] D. Ning, Y. Shoshin, M. van Stiphout, J. van Oijen, G. Finotello, and P. de Goey. "Temperature and phase transitions of laser-ignited single iron particle". In: *Combustion and Flame* 236 (2022), p. 111801.

[22] S. Li, D. Sanned, J. Huang, E. Berrocal, W. Cai, M. Aldén, M. Richter, and Z. Li. "Stereoscopic high-speed imaging of iron microexplosions and nanoparticle-release". In: *Optics Express* 29.21 (2021), pp. 34465–34476.

[23] P. Tóth, Y. Ögren, A. Sepman, P. Gren, and H. Wiinikka. "Combustion behavior of pulverized sponge iron as a recyclable electrofuel". In: *Powder Technology* 373 (2020), pp. 210–219.

[24] S. Golshan, R. Sotudeh-Gharebagh, R. Zarghami, N. Mostoufi, B. Blais, and J. Kuipers. "Review and implementation of CFD-DEM applied to chemical process systems". In: *Chemical Engineering Science* 221 (2020), p. 115646.

[25] D. Jajcevic, E. Siegmann, C. Radeke, and J. G. Khinast. "Large-scale CFD–DEM simulations of fluidized granular systems". In: *Chemical Engineering Science* 98 (2013), pp. 298–310.

[26] T. Lichtenegger, E. Peters, J. Kuipers, and S. Pirker. "A recurrence CFD study of heat transfer in a fluidized bed". In: *Chemical Engineering Science* 172 (2017), pp. 310–322.

[27] X. Liu, N. G. Deen, and Y. Tang. "On the treatment of bed-to-wall heat transfer in CFD-DEM simulations of gas-fluidized beds". In: *Chemical Engineering Science* 236 (2021), p. 116492.

[28] A. Patil, E. Peters, and J. Kuipers. "Comparison of CFD–DEM heat transfer simulations with infrared/visual measurements". In: *Chemical Engineering Journal* 277 (2015), pp. 388–401.

[29] J. Tausendschön, J. Kolehmainen, S. Sundaresan, and S. Radl. "Coarse graining Euler-Lagrange simulations of cohesive particle fluidization". In: *Powder Technology* 364 (2020), pp. 167–182.

[30] S. Wang and Y. Shen. "Coarse-grained CFD-DEM modelling of dense gas-solid reacting flow". In: *International Journal of Heat and Mass Transfer* 184 (2022), p. 122302.

2

EXPERIMENTS ON DEFLUIDIZATION

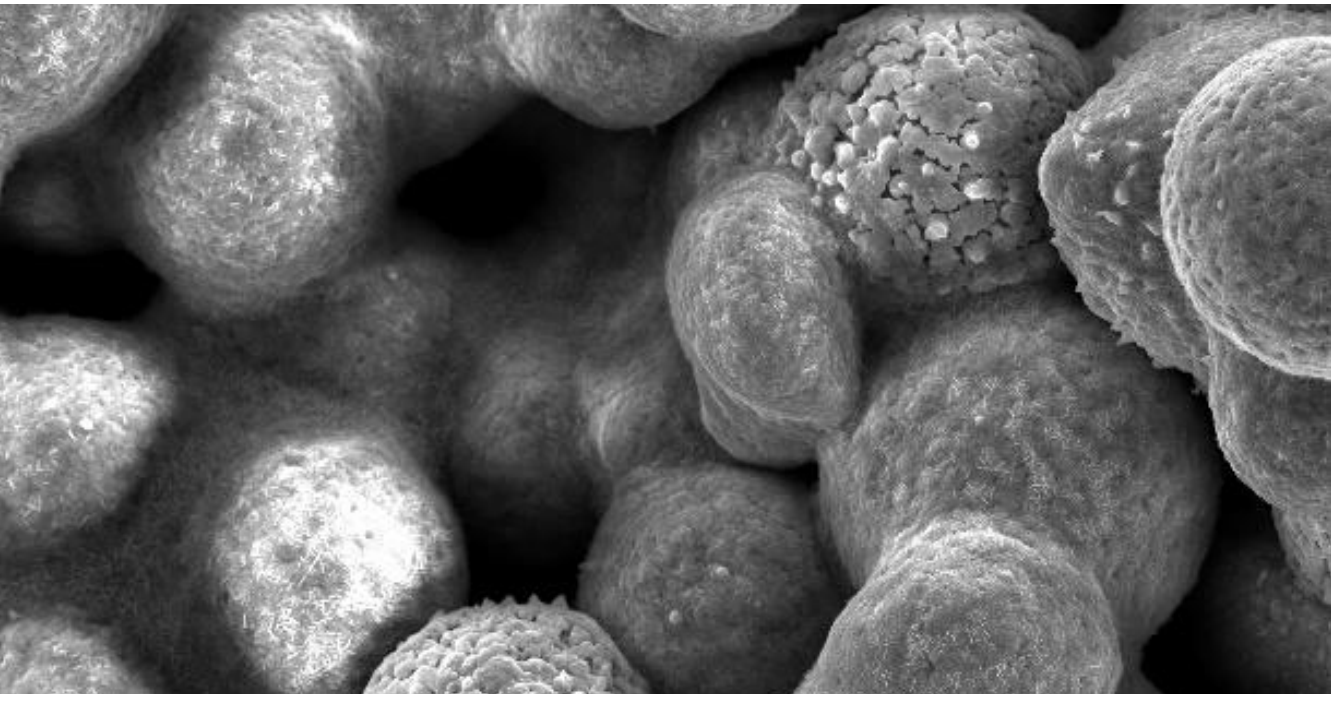

Acknowledgment: Thanks to C. J. M. Hessels for contributing this SEM image of sintering.
This chapter is based on: X. Liu, X. Zhang, J. Li, Q. Zhu, N. G. Deen, Y. Tang:
Regeneration of iron fuel in fluidized beds Part I: defluidization experiments and theoretical prediction model.
Powder Technology, 2023. (Accepted)

Abstract

Hydrogen-based direct reduction of iron oxide powder in gas-fluidized beds has become an emerging technology. Agglomeration of fine powder at elevated temperatures is however one key issue hindering the technological development. To obtain better knowledge of the high-temperature agglomeration mechanism, the (de-)fluidization behavior of micron-sized combusted iron particles is experimentally studied in this Chapter. Effects of various operating and material variables (temperature, gas flow rate, and particle size) on the fluidization and agglomeration behavior are investigated. Different fluidization regimes (e.g. stable fluidization, agglomerating fluidization, fast defluidization) are categorized based on the experimental results. A theoretical model based on the force balance is developed to predict the regime boundaries of fluidization. The obtained knowledge is applied for experimental design of the hydrogen-based iron direct reduction process in Chapter 3.

2.1. Introduction

Energy is an important component of modern economy. So far, it has mainly been driven by fossil fuels such as coal, oil, and natural gas as the main fuel. However, due to the negative consequences of climate change on the global environment and the limited fossil-fuel resources, energy and transportation systems must transit away from fossil-fuel sources to zero-carbon clean and renewable energy sources. Recently, metal fuels have been proposed as a promising clean energy storage system due to the high energy density of metal powder and low or even negative net carbon dioxide emissions [1–3]. Metal particles can be ignited easily and release a large amount of thermal energy, and the only solid product (metal oxides) can be collected and reused by reducing it back to metal powders using clean reducing agents. In this way, metal fuels are fully recyclable and, therefore, resource efficient.

With its high volumetric energy density (e.g. 16 kWh/L for iron [4]) and abundant availability, micron-sized iron powder has attracted a lot of interest in energy applications [3, 5, 6]. To fulfill a carbon-neutral fuel cycle, regeneration of the metallic iron powder from the combustion product (iron oxides) using renewable energy (e.g. green hydrogen) is crucial. The reduction of iron oxides by hydrogen proceeds in two or three steps, under and above 570 °C, respectively. Below 570 °C, the reduction follows the sequence: Fe_2O_3 to Fe_3O_4, and continues to Fe since wüstite is unstable below 570 °C. When the reduction temperature is higher than 570 °C, the reduction occurs stepwise from Fe_2O_3 via Fe_3O_4 to FeO and continues to Fe. For this reduction process, gas-fluidized bed reactors have been primarily considered due to their effective gas-solid mixing, and excellent heat and mass transfer characteristics [7, 8]. Previous efforts have been made for understanding the reduction process of iron oxides in fluidized beds [9–11]. However, most of the studies reported a technical issue, i.e., agglomeration due to particle sintering at elevated temperatures, causing severe operational problems or defluidization [12–15]. Therefore, better understanding the agglomeration or sintering phenomenon of iron/iron oxide particles in a fluidized bed is a crucial step towards the technological development of direct iron reduction in the metal fuel cycle.

It is generally accepted that the agglomeration/sticking occurs mostly during the emergence of the metallic iron, and highly depends on the type of iron ore [13, 16, 17]. Furthermore, previous studies reported that the agglomeration/sticking increases with increasing temperature, decreasing particle size and gas flow rate [15, 18–20]. Experimental efforts have been made to prevent such problem from the perspective of reactor geometry, particle coating, and the reduction process [14, 21–23]. There is one problem, i.e., the majority of these studies using gas-fluidized bed reactors in literature focuses on iron ore, which is the raw material in iron/steel industries. However, the iron/iron oxide powder applicable for the metal fuel application possesses different physical properties from the iron ore [5, 24, 25], e.g., purity, size, and morphology. Specifically, natural iron ore contains more elements, i.e., Fe, O, Si, Al, Mg, S, etc. The inclusion of a small number of other elements (except Fe and O) can exhibit significantly different characteristics from the high purity of iron/iron oxides. On the other hand, the particle size (μm size) and the surface morphology (rather smooth) of combusted iron powders have profound effects on the sticking between contact particles, which makes it distinctly different from iron ore (cm size and non-spherical). Therefore, in order to better understand the fluidization

performance of iron oxide powder directly resulting from iron powder combustion, further studies are required.

In addition to experimental studies, theoretical analysis to predict the (de-)fluidization behavior of iron/iron oxides is also crucial. Xu et al. [26] established a model to predict the agglomeration size on the basis of an energy balance, considering the van der Waals force as the dominating cohesive force. They found that the agglomerate size decreases with the increase of gas velocity. Zhong et al. [27] proposed a mathematical model to predict the defluidization temperature using a balance between the drag acting on the particles and the cohesive force. Later, Lei et al. [17] derived a force balance model by considering the collision force and the cohesive force between particles. These models are reported to perform well for respectively experimental conditions, and can represent a relatively clear boundary between fluidization and defluidization. However, it is still hard to distinguish the boundary between stable and unstable/agglomerating fluidization. Additionally, models still need to be developed further due to the complicated overall flow motion in the fluidized bed.

The present work is concerned with studying the fluidization and reduction performance of micron-sized combusted iron powder in a fluidized bed, with the ultimate goal to guide the practical design of hydrogen-based direct reduction of combusted iron. In Chapter 2, we focus on (de-)fluidization behavior of these iron/iron oxide particles in a fluidized bed, while in Chapter 3 we will experimentally study the reduction performance with the insight learned from the present (de-)fluidization study. Therefore, the experiments presented in this work are carried out under N_2 atmosphere in a lab-scale fluidized bed, i.e., without reaction. Different operation parameters including gas flow rate, temperature, and particle size are investigated to understand their effects on the transition of fluidization regimes and particle sintering phenomenon.

In this Chapter we will first introduce the (inter)-particle forces and theoretical description (Section 2.2). Subsequently, we present the experimental setup and conditions in Section 2.3. In Section 2.4, the effects of the particle size, temperature and gas flow rate on the fluidization behavior are discussed. Furthermore, the results of SEM images and the performance of the theoretical model are presented. Finally, critical conclusions are drawn in Section 2.5.

2.2. Particle forces

In gas-fluidized beds, particles are subject to gravity and drag due to the flow of gas. In some circumstances, some interparticle forces may also become noticeable [28]. In the current study, we consider interparticle forces related to cohesion behavior for combusted micron-sized iron particles at elevated temperatures. Thus, we mainly consider the solid bridge or sintering force, which is usually orders of magnitude larger than e.g., the van der Waals force at high temperatures. The solid bridge force is the attractive force which contributes to the formation of agglomerates, while the drag and the collisional contact forces are the mechanisms to break or prevent the agglomerates. Agglomeration only occurs in the case when the attractive cohesion force is larger than the breaking forces.

2.2.1. Solid bridge force

The solid bridge force, also known as sintering force, usually occurs in systems where the bonding of two or more particles takes place at elevated temperatures below the melting point of the particles [29]. The thermochemical reduction of iron oxides is normally conducted at high temperatures (≥ 500°C), at which the particle surface becomes soft and sticky. When these sticky particles come into contact, a permanent solid bridge can form between the colliding particles.

Four categories of sintering mechanisms may be discerned, in which the relation between the neck size x formed due to sintering and the contact time t is described: plastic and viscous flow ($x^2 \sim t$); evaporation and condensation ($x^3 \sim t$); volume diffusion ($x^5 \sim t$); surface diffusion ($x^7 \sim t$). The formation of the interface between two particles can occur by one or a combination of the above-mentioned mechanisms. Specific sintering mechanisms can be determined by measuring the neck size growth as a function of time and temperature. Kuczynski et al. [29] experimentally investigated the sintering mechanisms for metals and pointed out that the sintering mechanism for metals of low vapor pressure is predominantly that of surface diffusion in the early stage and of volume diffusion in the later stage. The volume diffusion mechanism occurs in the situation when there exists higher hole concentration in the area near the interface, which causes the flow of atoms from the main part to the junction. The surface diffusion mechanism is very similar to the volume diffusion mechanism. In this situation, the atoms migrate from the particle surface to a neck connecting the particles. In a gas-fluidized bed, the particle's contact updates frequently, assuming the sintering occurring in the early stage and following a surface diffusion mechanism is reasonable. Previous studies also showed that the sintering mechanism of iron powder follows surface diffusion [30]. Based on Kuczynski's [29] surface diffusion model, the solid bridge force between two particles i and j can be expressed as:

$$F_{\mathrm{sb,ij}} = \pi \sigma x^2 \tag{2.1}$$

where σ is the tensile strength of particle material. x is the neck radius (see Figure 2.1), which can be calculated based on the surface diffusion mechanism:

$$x = \left(\frac{56 \gamma \delta^4}{KT} D_s a^3 t \right)^{1/7} \tag{2.2}$$

with:

$$D_s = D_{o,s} \exp\left(\frac{-E_{\mathrm{s}}}{RT} \right) \tag{2.3}$$

where γ is the surface tension; δ is the lattice constant; D_s is the surface diffusion coefficient; a is the curvature radius; $D_{o,s}$ and E_{s} are the frequency factor and activation energy of surface diffusion; K is the Boltzmann constant; T is the particle temperature, and t is the contact time.

Note that the curvature radius is depending on the particle's geometry. Kuwagi et al. [31] reported that for a smooth surface, the particle radius can be used as the curvature radius, while for rough particles, the surface roughness is chosen as the curvature radius, which is about one tenth of particle radius. When surface roughness exists, instead of a macroscopic contact point, there may be multiple microcontact points. As reported

in the work of Kuwagi et al. [31], the number of contact points can be either three or nine. Considering all options, the solid bridge force models can be expressed by a general equation:

$$F_{\mathrm{sb,ij}} = \mathrm{C}\pi\sigma\left(\frac{56\gamma\delta^4}{KT}D_s\mathrm{r_p^3}t\right)^{2/7} \tag{2.4}$$

with C = 0.417, 1, and 1.251 representing the three-microcontact-point model, the smooth surface model, and the nine-microcontact-point model, respectively. Note that the solid bridge force is directed along the line connecting the particle centers.

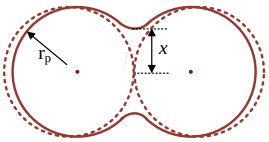

Figure 2.1: Schematic overview of sintering behavior between two smooth particles.

2.2.2. Contact force

For two colliding particles, a repulsive force of F_{n} along the normal direction occurs, which tends to counteract the effect of particle attraction. A maximum repulsive force can be estimated according to the maximum deformation during the contact period:

$$F_{\mathrm{n}} = k_{\mathrm{n}}\delta_{\mathrm{max}} \tag{2.5}$$

with:

$$k_{\mathrm{n}} = \frac{4}{3}\mathrm{Y^*}\sqrt{\mathrm{r^*}\delta_{\mathrm{max}}} \tag{2.6}$$

The maximum overlap can be estimated by:

$$\delta_{\mathrm{max}} = \left(\frac{15\mathrm{m^*}v_{\mathrm{n,ij}}^2}{16\mathrm{Y^*}\mathrm{r^{*\,1/2}}}\right)^{2/5} \tag{2.7}$$

where $v_{\mathrm{n,ij}}$ is the particle relative velocity; k_{n} refers to the stiffness constant; δ_{max} is the maximum normal overlap. An effective particle radius ($\mathrm{r^*}$), effective elastic moduli ($\mathrm{Y^*}$), and effective particle mass ($\mathrm{m^*}$) are defined by:

$$\frac{1}{\mathrm{r^*}} = \frac{1}{\mathrm{r_i}} + \frac{1}{\mathrm{r_j}}, \frac{1}{\mathrm{Y^*}} = \left(\frac{1-\nu_i^2}{\mathrm{Y}_i}\right) + \left(\frac{1-\nu_{\mathrm{j}}^2}{\mathrm{Y_j}}\right), \frac{1}{\mathrm{m^*}} = \frac{1}{\mathrm{m_i}} + \frac{1}{\mathrm{m_j}} \tag{2.8}$$

where ν is the Poisson's ratio.

2.2.3. Drag force

Besides the interparticle normal contact force, the drag force is another force to disturb the cohesive behavior. In a dense system, the Ergun equation [32] can be used to predict the particle's drag:

$$\mathbf{F}_d = \frac{\beta V_p}{1-\varepsilon_f}(\mathbf{u}_g - \mathbf{v}_p) \tag{2.9}$$

with:

$$\beta = 150\frac{(1-\varepsilon_f)^2\mu_f}{\varepsilon_f d_p^2} + 1.75\frac{(1-\varepsilon_f)\rho_f|\mathbf{u}_g - \mathbf{v}_p|}{d_p} \tag{2.10}$$

where V_p is the particle volume; $\mathbf{u}_g$ and $\mathbf{v}_p$ are the interstitial gas and particle velocity; β is the gas-particle momentum exchange coefficient; ρ_f is the gas density; ε_f is gas phase voidage; d_p is the particle diameter.

2.3. Experiments

2.3.1. Experimental materials

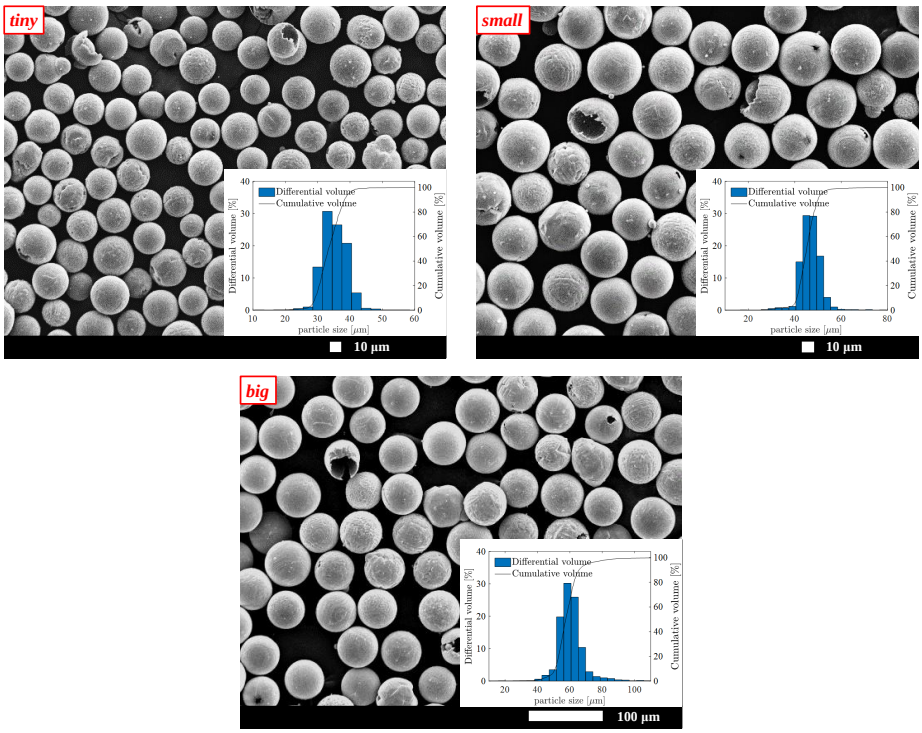

Figure 2.2: SEM image and the particle size distribution of the raw materials.

The iron oxide powder used in current study is produced by a combustion process of high purity (> 99% Fe) iron powder which is originally purchased from Quebec Metal Powders LTD (grade: Atomet 95). Iron combustion is conducted in a pilot scale industrial burner, and the resulting combusted (iron oxide) powder is captured using a cyclone after a long

horizontal cooling section. The combusted iron powder is sieved into three size ranges i.e., 29.6 – 38.6 μm, 41.2 – 50.3 μm, and 51.4 – 66.2 μm (d10 – d90), with d50 of 33.7 μm, 45.5 μm, and 58.0 μm, respectively. In this work, we refer to these fractions as *tiny*, *small* and *big*. Figure 2.2 shows the particle morphology recorded with SEM (scanning electron microscope). Most of the particles are spherical and have a rather smooth surface. XRD (X-ray diffraction) analysis shows that the powder is composed of hematite and magnetite in a weight ratio of roughly 40:60. The particle bulk densities are 2550 kg/m^3, 2500 kg/m^3, and 2420 kg/m^3 for *tiny*, *small*, and *big* powder respectively.

2.3.2. Apparatus and procedures

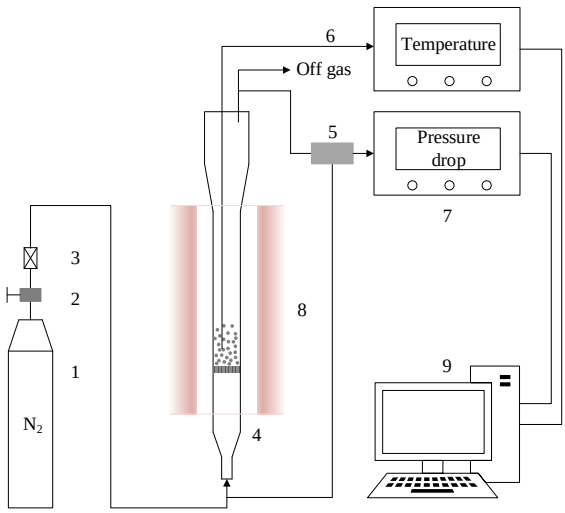

Figure 2.3: Schematic overview of the experimental setup (1-Gas cylinder; 2-Shut-off valve; 3-Mass flow controller; 4-Fluidized bed reactor; 5-Differential pressure sensor; 6-Thermocouple; 7-Display instruments; 8-Electric resistance furnace; 9-Data acquisition system).

The fluidization experiments are conducted in a laboratory-scale quartz cylindrical fluidized bed. Figure 2.3 shows a schematic overview of the setup. The cylinder has a height of 960 mm with an inner diameter of 16 mm. A porous quartz plate with a uniform pore diameter of 0.15 mm is used as the gas distributor at the bottom of the reactor.

We first measure the minimum fluidization velocity for different powders under N_2 atmosphere at room temperature. The measured results are given in Table 2.1 and compared to Ergun's predictions [32] using $\varepsilon_{mf} = 0.4$ and d50. Small difference between the measured and predicted values may be attributed to the particle size distribution.

Then the fluidization experiments are conducted with the conditions specified in Table 2.2. The flow rates of nitrogen (u_0) in this table correspond to $2u_{mf}$ to $8u_{mf}$ at room temperature. Note that at high temperatures, u_0 and u_{mf} differ from those at room temperature due to the gas/particle property change. For all fluidization experiments, 10.0 g of combusted iron powder is first fed into the fluidized bed reactor at room temperature with supplying N_2. Then the fluidized bed reactor is heated to the desired temperature by

a vertical furnace. The temperature of the bed is monitored by a plug-in thermocouple (component #6 in Figure 2.3). The heating process is conducted under N_2 atmosphere with a specific gas flow rate according to the specific experimental conditions. After the temperature reaches the pre-set value, the combusted iron powder is fluidized for a fixed time or till defluidization occurs. During the experiments, a differential pressure sensor is used to monitor the bed pressure drop. When the experiment is finished, the reactor is removed from the furnace and quenched directly by spraying water on its outer surface until room temperature is reached. The powder sample is stored in a ziplock bag and prepared for further measurements.

Table 2.1: Results of the minimum fluidization velocity measured under N_2 atmosphere at room temperature.

Particle size [−]	tested u_{mf,N_2} [m/s]	u_{mf} calculated by Ergun equation [m/s]
tiny	0.0028	0.0027
small	0.0050	0.0050
big	0.0091	0.0080

Table 2.2: Experimental conditions.

Particle size [-]	u_0/u_{mf} [-]	T_b [°C]
tiny	2 – 8	20 – 850
small	2 – 8	20 – 950
big	2 – 8	20 – 1000

2.4. Results and discussions

In this section, the (de-)fluidization behavior of combusted iron powder with three size distributions fluidized at different temperatures and gas velocities is presented and discussed. Subsequently the theoretical prediction of the defluidization temperature is presented based on the force balance of a single particle.

2.4.1. (De-)fluidization experiments

Transition of fluidization regimes

Figure 2.4 shows a typical bed pressure drop profile vs. operating time during the fluidization experiments. In such experiments, the powder is first fluidized at a pre-set gas flow rate and then the fluidized bed is linearly heated up until the occurrence of defluidization. Note that the bed pressure drop in the figure is indirectly obtained by subtracting the distributor pressure drop from the measured total pressure drop of the reactor. We define t = 0 as the point when the bed temperature reaches to 200 °C. It can be seen that, during the heating process the bed pressure almost stays constant but after a certain time the pressure drop decreases first slowly and then sharply till almost zero, indicating a defluidization with a full dead bed. We define two critical temperatures from this figure: 1) the defluidization temperature (T_d) at which the defluidization occurs; 2) the transition

temperature (T_t) at which the pressure drop starts to decrease. Since the heating process is linear, these temperatures also reflect the corresponding duration of different fluidization regimes. Accordingly, three fluidization regimes are distinguished: 1) stable fluidization where the mean bed pressure drop stays constant; 2) unstable fluidization where the pressure drop slowly decrease (between T_t and T_d); 3) defluidization ($T > T_d$). The transition from stable to unstable fluidization is attributed to the formation of agglomerates due to particle sintering. As the experiment continues, the extent of agglomeration gradually increases and it penetrates throughout the bed. Finally, one big particle agglomerate with a size equivalent to the bed diameter is formed above the distributor, leading to a complete defluidization.

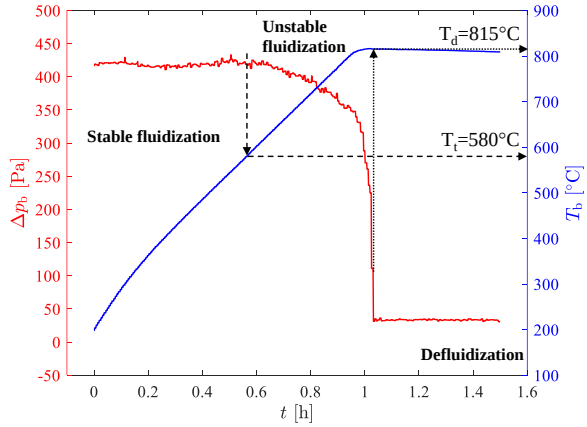

Figure 2.4: The bed pressure drop vs. time for fluidization of *tiny* powder at $u_0/u_{mf} = 4$ with a linear temperature increase to 815 °C.

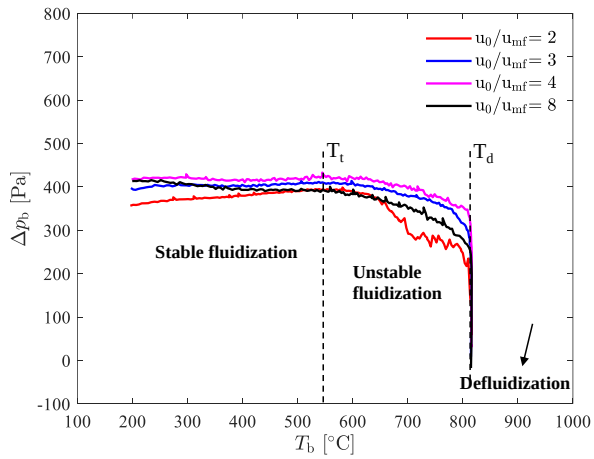

Figure 2.5: The bed pressure drop against the bed temperature with $u_0/u_{mf} = 2-8$ (*tiny* powder).

Figure 2.5 shows the bed pressure drop against the bed temperature at various gas flow rates for the *tiny* particles. Similar to Figure 2.4, the two critical temperatures and three fluidization regimes can be clearly identified. It can be seen that the transitions between the different regimes and corresponding critical temperatures are almost insensitive to the gas flow rate. For all the experiments with increasing gas flow rate from $2u_{mf}$ to $8u_{mf}$, the transition to unstable fluidization occurs at $T_t = 580\,^{\circ}C$ and the defluidization occurs at $T_d = 815\,^{\circ}C$.

Similar experiments are performed using *small* and *big* particles, and the results are shown in Figures 2.6 and 2.7. Again, the three fluidization regimes associating with two critical temperatures can be clearly distinguished. Regarding the effect of gas flow rate, we see that for these two sizes of powder the transition temperature T_t is also independent of the gas flow rate, similar to the *tiny* powder. However, a slight difference appears to the defluidization temperature T_d, especially for *small* powder. As the gas flow rate increases, T_d slightly increases as well, corresponding to a longer defluidization time. In principle, the mean bed pressure drop in stable fluidization regime should be identical at different gas flow rates due to the same weight of powder fed into the bed. The small difference in Figures 2.5-2.7 can be attributed to the measurement error. As mentioned above, the bed pressure drop is indirectly obtained from the measured total pressure drop including the pressure drop over the distributor. Since the bed pressure is much smaller than the distributor pressure drop, small fluctuations in the measured total and/or distributor pressure drops may introduce noticeable errors in the calculated pressure drop value of the fluidized bed.

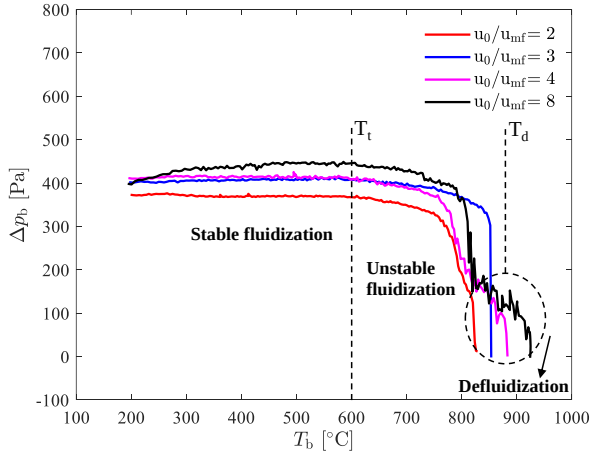

Figure 2.6: The bed pressure drop against the bed temperature with $u_0/u_{mf} = 2-8$ (*small* powder).

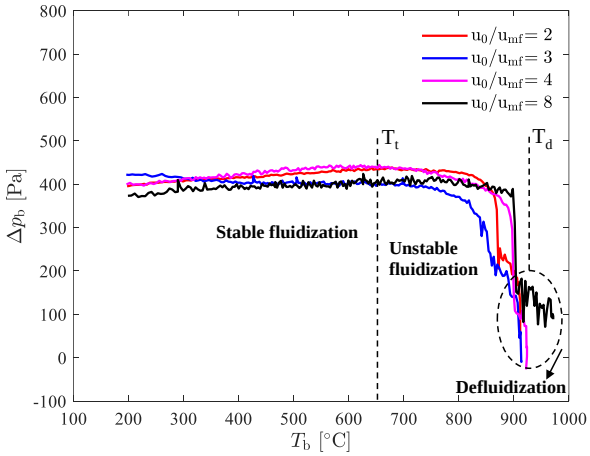

Figure 2.7: The bed pressure drop against the bed temperature with $u_0/u_{mf} = 2-8$ (*big* powder).

Two additional experiments are conducted at the pre-set temperatures below T_d for *tiny* powder at $u_0/u_{mf} = 3$. These experiments are meant to provide further insight on the unstable regime. Figure 2.8 shows the bed pressure drop and the bed temperature profiles against the operating time with pre-set temperatures of 550 °C and 700 °C. It can be seen that in the experiment conducted at 550 °C, a temperature below the transition temperature $T_t = 580$ °C, the fluidization of the powder bed stays stable indicated by a constant mean bed pressure drop. In contrast, if the bed temperature exceeds T_t, as for the test at 700 °C, the bed always transits to unstable fluidization regime. In this case, even if the temperature is no longer increased, defluidization of the bed still takes place after a longer period of operation. This indicates that when the bed temperature is higher than the transition temperature, the bed eventually defluidizes. This can be understood from the solid bridge force eq. (2.4), which is highly temperature dependent.

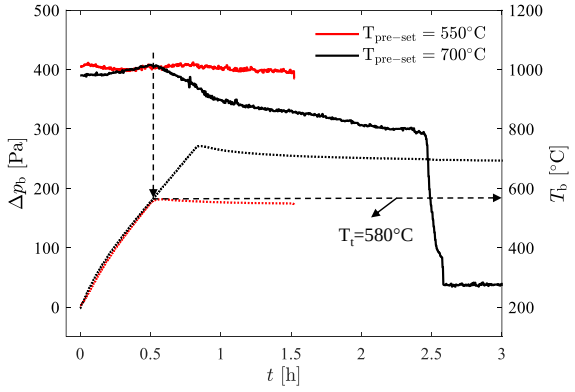

Figure 2.8: The bed pressure drop and bed temperature profiles against the operating time when $u_0/u_{mf} = 3$ with pre-set temperature of 550 °C and 700 °C (*tiny* powder). Solid lines: bed pressure drop (Δp_b); dotted lines: bed temperature (T_b).

Effect of particle size

The obtained transition temperature (T_t) and defluidization temperature (T_d) from Figures 2.5-2.7 for different powder sizes are compared in Table 2.3. Clearly, larger particles show both higher T_t and higher T_d. This dependency can be possibly explained by the following reasons. First, smaller particles have larger specific surface area, which increases the interparticle contact chances. Consequently, it increases the possibility of agglomeration, thus accelerating the transition from stable to unstable fluidization and finally defluidization. Additionally, bigger particles have a higher kinetic energy with a larger mass and momentum, and therefore a lower tendency to form agglomerates [20]. Secondly, smaller particles have been shown to exhibit lower melting temperatures due to a larger surface-to-volume ratio than bulk materials, thus altering their thermodynamic and thermal properties [33, 34]. This melting temperature is linearly correlated to the so-called Hütting and Tamman temperatures [34, 35]. At the Hütting temperature, atoms at defects (e.g. edges and corner sites) of solids start to exhibit mobility. When the Tamman temperature is reached, atoms from the bulk show mobility and the bulk diffusion becomes appreciable. Therefore, lower melting temperature of smaller particles leads to the fact that sintering of smaller particles happens at a lower temperature, thus smaller T_t and T_d.

Table 2.3: The summary of the defluidization behavior study based on different sizes of particle.

Particle size	T_t [°C]	T_d [°C]
tiny	580	815
small	600	824 – 924
big	650	911 – 972

Agglomeration behavior

Figure 2.9 shows an image of *tiny* powders fluidized for 1h at a pre-set temperature of 650°C, corresponding to the unstable fluidization regime. From the picture, some agglomerates of intermediate size can be identified. The presence of these agglomerates dampens the fluidization, and thus the bed pressure decreases. In contrast, the majority of the powder in the bed remains dispersed particles as shown in the SEM image. Thus the fluidization can still last, but in an unstable manner.

To get more information of the powder's morphology after a defluidization process, one additional experiment using *small* powder is conducted. The pre-set temperature is 850°C and the pre-set fluidization time after reaching the pre-set temperature is 1h. Figure 2.10 shows images of *small* powder after defluidization. We can clearly see a big honeycomb-like block of sintered particles with a size equivalent to the bed diameter. As mentioned earlier, this big block is usually formed just above the distributor, obstructing the fluidization. Again, the SEM image shows that most of the powder is still in the form of dispersed particles, although some small agglomerates are also present. Therefore, we believe that developing strategies to prevent the expansion of particle sintering/agglomeration above the distributor is the key to solving the defluidization issue at elevated temperatures. It is also worthwhile to mention that agglomerates present in these experiments in the beginning stage of the unstable region are fragile, meaning that they are easy to break with a small mechanical force.

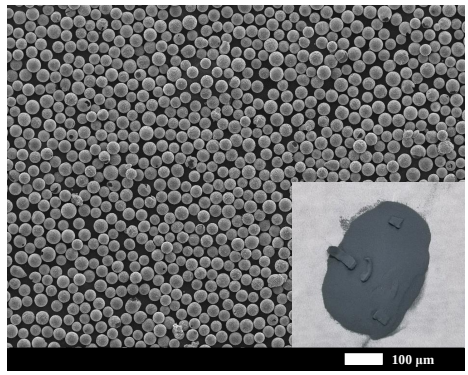

Figure 2.9: Image of combusted iron powders fluidized for 1h in an unstable fluidization regime. (operating condition: *tiny* powder, $u_0/u_{mf} = 3$, $T_{pre-set} = 650\,^{\circ}C$)

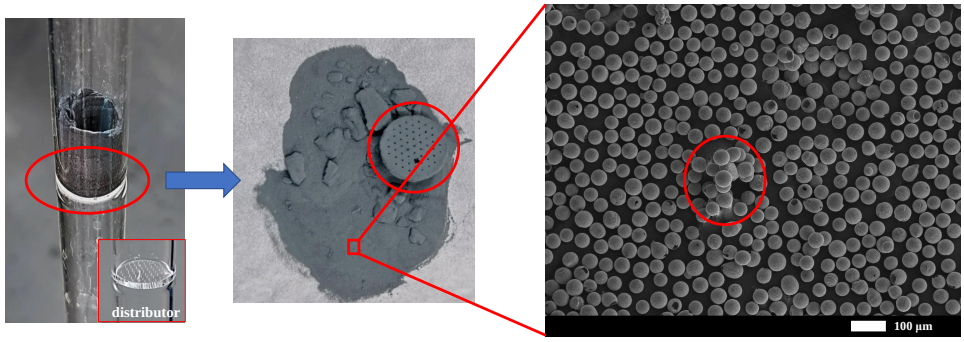

Figure 2.10: Images of combusted iron powders after defluidization. (operating condition: *small* powder, $u_0/u_{mf} = 4$, $T_{pre-set} = 850\,^{\circ}C$)

2.4.2. Prediction of defluidization

The fluidization behavior depends on the gas-solid and inter particle forces. Therefore, we can employ a force balance of cohesive and breaking forces (as described in Section 2.2) to predict the fluidization regime transitions and the corresponding temperatures.

Determination of solid bridge force

Determination of the solid bridge force (eq. (2.4)) requires the knowledge of solid properties. The combusted iron powder is composed of hematite and magnetite. The material properties of both hematite and magnetite used in this work are listed in Table 2.4. The material tensile strength depends on temperature is chosen from the work of Hidaka et al. [36]. As can be seen in Table 2.4, the frequency factor $D_{o,s}$ of both materials differs nine orders. However, we know from the iron combustion mechanism that the outer layer of the particles primarily consists of hematite [37]. As the sintering of iron oxide particles is

a surface diffusion mechanism, we can therefore use the parameters based on hematite for the calculation of the solid bridge force. Another model parameter in eq. (2.4) is the contact time (t). Since the collision between particles in a fluidized bed is frequent and occurs in a very short time, we assume it is equivalent to the collision contact time of two particles [38]:

$$t = 2.868\left(\frac{\mathrm{m}^{*2}}{\mathrm{Y}^{*2}\mathrm{R}^{*}\,v_{\mathrm{n,ij}}}\right)^{1/5} \tag{2.11}$$

In a gas-fluidized bed, the particle relative velocity ($v_{\mathrm{n,ij}}$) exhibits a distribution of a wide range in values, particularly for a cohesive system. In a non-cohesive bubbling fluidized bed of micron-sized particles, CFD-DEM simulations show that the particle relative velocity ranges between 10^{-4} m/s to 10^{-2} m/s. When predicting fast defluidization behavior, it makes more sense to use the lower threshold of the collision velocity. Thus, we will take $v_{\mathrm{n,ij}}$ in the range of $(1-5)\cdot 10^{-4}$ m/s for the calculation of interparticle forces (i.e. in eqs. (2.7) and (2.11)).

Table 2.4: Material property dependent parameters for calculating the solid bridge force.

Property	Value (hematite)	Value (magnetite)
Surface tension γ (N/m)	$1^{(a)}$	$1^{(a)}$
Lattice constant δ (m)	1.38×10^{-9}	8.39×10^{-10}
Frequency factor $D_{o,s}$ (m^2/s)	$2.8\times10^{-13(b)}$ ($\leq 900\,^{\circ}$C)	$5.2\times10^{-4(c)}$
	$1.6\times10^{5(b)}$ ($>900\,^{\circ}$C)	$5.2\times10^{-4(c)}$
Activation energy E_s (J/mol)	$1.74\times10^{5(b)}$ ($\leq 900\,^{\circ}$C)	$2.30\times10^{5(c)}$
	$5.79\times10^{5(b)}$ ($>900\,^{\circ}$C)	$2.30\times10^{5(c)}$
Poisson's ratio ν (−)	$0.12^{(d)}$	$0.37^{(d)}$
Young's modulus E (GPa)	$359^{(d)}$	$175^{(d)}$
Density ρ_{a} (kg/s^3)	5240	5180

(a), (b), (c), and (d) are from the literature of [39], [40], [41], and [42].

Model prediction of defluidization temperature

When a fluidized bed operates at elevated temperature, the solid bridge force is the attractive interparticle force letting the particles stick together, whereas the drag force and the collision force are the driving forces which would potentially break the agglomerates. Thus, the criterion of fast defluidization would be the balance between the attractive force and the maximum breaking force.

Figure 2.11 presents the results of drag, collision and sintering forces normalized by the gravity force of the particle as a function of bed/particle temperature. Note that the dotted lines represent the calculation of sintering and collision forces using $v_{\mathrm{n,ij}}$=$1\cdot10^{-4}$ m/s, whereas the solid lines represent the calculation using $v_{\mathrm{n,ij}}$=$5\cdot10^{-4}$ m/s. Shadow regions represent the drag forces calculated based on the actual gas flow rates used in our experiments. For a typical defluidization process, it often starts with agglomeration at dense regions where the solid particles possess relatively low velocities, which corresponds to the onset of unstable fluidization as observed in Figures 2.5-2.7. Subsequently, the agglomeration will expand and penetrate through the entire bed, leading to the defluidization.

Furthermore, all the three solid bridge force models (given by the general expression eq. (2.4)) are presented in Figure 2.11. Note that the models only differ by the value of C, and the determined solid bridge force by the smooth surface model and the nine-microcontact-point model is very close. As shown by the SEM images in Figure 2.2, the surface morphology of combusted iron particles is rather smooth or little rough. Considering the predicted results using the nine-microcontact-point model is reasonable. The transition of the solid bridge curve shown in Figure 2.11 is caused by the different diffusion coefficients below and above 900 °C. Finally, we can see that the drag force is generally one order smaller in magnitude than the collision force. Thus in the fluidization systems in current study, particle collisions are the dominating mechanism of breakage. This explains the observation from experimental results in Table 2.3, i.e., the two critical temperatures for transitions from stable to unstable to defluidization regimes are almost insensitive to the increasing gas velocity.

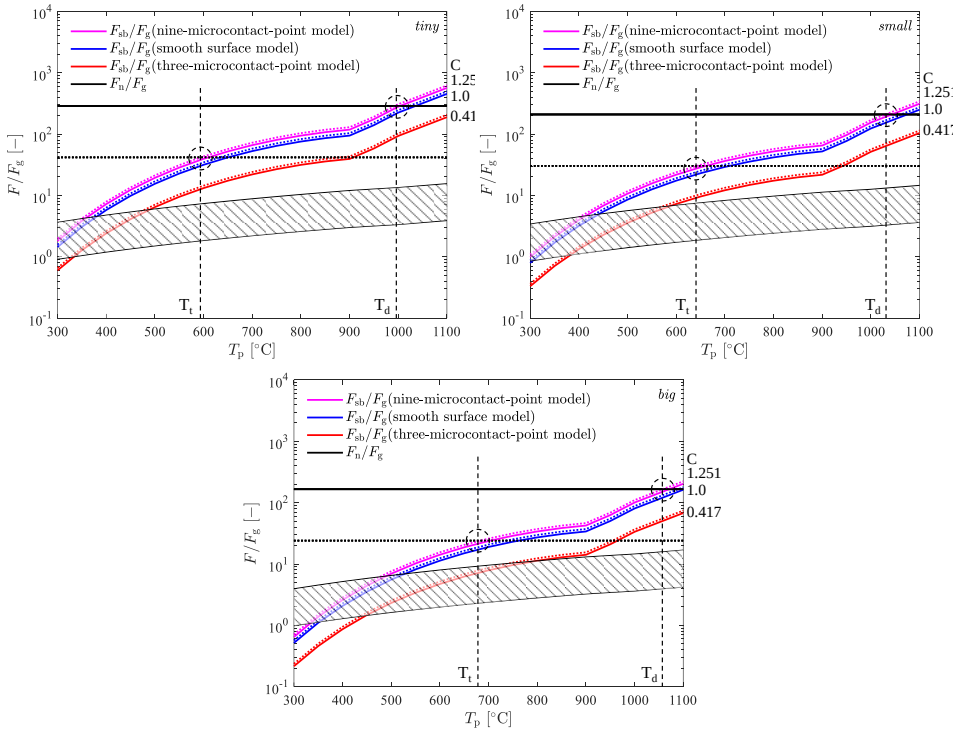

Figure 2.11: Normalized forces as a function of temperature: Solid lines represent the calculation using $v_{n,ij}$ = 5e-4 m/s; dotted lines represent the calculation using $v_{n,ij}$ = 1e-4 m/s; shadow regions represent the drag forces calculated based on the range of gas flow rates using in our experiments. The balance points (circles) represent the predicted transition temperature (T_t) (via dotted lines) and the predicted defluidization temperature (T_d) (via solid lines).

Table 2.5: The summary of the predicted and tested temperatures based on different sizes of particle.

Particle size	Predicted T_t [°C]	Tested T_t [°C]	Predicted T_d [°C]	Tested T_d [°C]
tiny	594	580	993	815
small	642	600	1030	824 – 924
big	683	650	1058	911 – 972

According to the criteria for unstable fluidization and defluidization, the temperature corresponding to the intersections of the curves of the maximum breaking force, i.e., the collision force and the solid bridge force, are the transition temperature (T_t) (via dotted lines) and the defluidization temperature (T_d) (via solid lines). Therefore, we summarize the predicted temperatures obtained by the nine-microcontact-point model in Table 2.5, including the actual temperatures obtained from experiments. The applied relative velocities range roughly coincides with the temperature window in which agglomeration is important, i.e., between the transition temperature (T_t) and the defluidization temperature (T_d). In this window the solid bridge force has a similar order of magnitude as the contact force, meaning that agglomeration can no longer be neglected. In general, the model gives a fair estimate showing an increase of the critical temperatures as the particle size increases.

Regarding the general overprediction, we think the possible explanation is because of the material properties. The determination of the solid bridge force shown in Figure 2.11 is based on the material properties of hematite. As mentioned earlier, the hematite would mostly present on the outer surface of the particles due to the combustion mechanism. However, the possibility that the presence of magnetite on and near the outer surface cannot be excluded. If the material property dependent parameters are based on magnetite, the determined solid bridge forces will be much larger, thus resulting in lower critical temperatures (see Figure 2.12 as an example for *tiny* particles). In general, the deviation between the predicted defluidization temperature and the defluidization temperature obtained experimentally is less than 25%, indicating that using the current modeling method can give a fair prediction of kinds of fluidization phases.

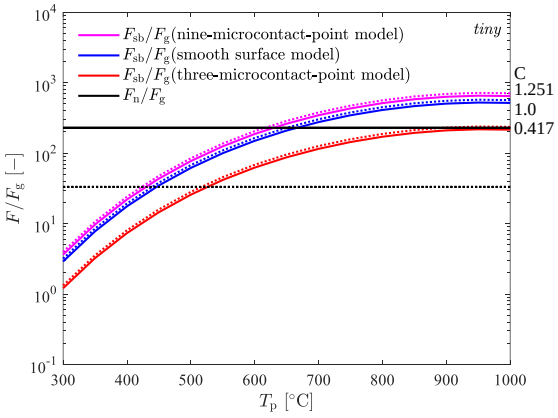

Figure 2.12: Comparison of breaking forces and solid bridge force for *tiny* magnetite particles. Solid lines represent the calculation using $v_{n,ij}$ = 5e-4 m/s; dotted lines represent the calculation using $v_{n,ij}$ = 1e-4 m/s.

2.5. Conclusions

In this work, we studied (de-)fluidization of combusted micron-sized iron powders under N_2 atmosphere at elevated temperatures. Transitions between stable fluidization, unstable fluidization, and defluidization have been identified with two critical temperatures T_t and T_d. These critical temperatures are found almost insensitive to gas flow rate, but highly depend on particle size. Furthermore, once unstable fluidization due to the formation of agglomerates occurs, either further increasing the bed temperature or increasing the operation time will eventually lead to defluidization of the bed.

Based on a simple force balance, a quantitative model for the fluidization characteristics of combusted iron powder is developed for the prediction of (de-)fluidization behavior at elevated temperatures. The theoretical model provides a reasonable prediction of the dependence of the transition temperature (T_t) and the defluidization temperature (T_d) on the particle size. The predicted critical temperatures show fair agreement with the experimental results, with a relative error in the order of 25%. The model also reflects the sintering mechanism of the studied powder to be a sintering force model based on rather smooth or little rough surface, and the particle collisions as the agglomeration breaking mechanism. We further use these gained experimental insights to design reduction experiments of combusted iron powder in Chapter 3.

Bibliography

[1] J. M. Bergthorson, S. Goroshin, M. J. Soo, P. Julien, J. Palecka, D. L. Frost, and D. J. Jarvis. “Direct combustion of recyclable metal fuels for zero-carbon heat and power”. In: *Applied Energy* 160 (2015), pp. 368–382.

[2] J. M. Bergthorson. “Recyclable metal fuels for clean and compact zero-carbon power”. In: *Progress in Energy and Combustion Science* 68 (2018), pp. 169–196.

[3] P. Julien and J. M. Bergthorson. “Enabling the metal fuel economy: green recycling of metal fuels”. In: *Sustainable Energy & Fuels* 1.3 (2017), pp. 615–625.

[4] S. H. Fischer and M. Grubelich. *Theoretical energy release of thermites, intermetallics, and combustible metals*. Tech. rep. Sandia National Lab.(SNL-NM), Albuquerque, NM (United States), 1998.

[5] D. Ning, Y. Shoshin, M. van Stiphout, J. van Oijen, G. Finotello, and P. de Goey. “Temperature and phase transitions of laser-ignited single iron particle”. In: *Combustion and Flame* 236 (2022), p. 111801.

[6] N. Poletaev and M. Khlebnikova. “Combustion of iron particles suspension in laminar premixed and diffusion flames”. In: *Combustion Science and Technology* 194.7 (2022), pp. 1356–1377.

[7] X. Liu, N. G. Deen, and Y. Tang. “On the treatment of bed-to-wall heat transfer in CFD-DEM simulations of gas-fluidized beds”. In: *Chemical Engineering Science* 236 (2021), p. 116492.

[8] S. E. Lehmann, E.-U. Hartge, A. Jongsma, I.-M. deLeeuw, F. Innings, and S. Heinrich. “Fluidization characteristics of cohesive powders in vibrated fluidized bed drying at low vibration frequencies”. In: *Powder technology* 357 (2019), pp. 54–63.

[9] X. Zhang, S. He, H. Sun, Q. Zhu, J. Li, and H. Li. “Mechanism of surface morphology evolution in the reduction of fine iron ore in a conical fluidized bed reactor”. In: *Chemical Engineering Science* 220 (2020), p. 115468.

[10] J. Li, J. Kong, S. He, Q. Zhu, and H. Li. “Self-agglomeration mechanism of iron nanoparticles in a fluidized bed”. In: *Chemical Engineering Science* 177 (2018), pp. 455–463.

[11] D. Spreitzer and J. Schenk. “Iron ore reduction by hydrogen using a laboratory scale fluidized bed reactor: kinetic investigation—experimental setup and method for determination”. In: *Metallurgical and Materials Transactions B* 50.5 (2019), pp. 2471–2484.

[12] Y. Zhong, Z. Wang, Z. Guo, and Q. Tang. “Defluidization behavior of iron powders at elevated temperature: Influence of fluidizing gas and particle adhesion”. In: *Powder technology* 230 (2012), pp. 225–231.

[13] S. Hayashi and Y. Iguchi. “Factors affecting the sticking of fine iron ores during fluidized bed reduction”. In: *ISIJ international* 32.9 (1992), pp. 962–971.

[14] S. Hayashi, S. Sawai, and Y. Iguchi. “Influence of coating oxide and sulfur pressure on sticking during fluidized bed reduction of iron ores”. In: *ISIJ international* 33.10 (1993), pp. 1078–1087.

[15] L. Guo, Q. Bao, J. Gao, Q. Zhu, and Z. Guo. “A review on prevention of sticking during fluidized bed reduction of fine iron ore”. In: *ISIJ International* 60 (2020), pp. 1–17.

[16] J. Gransden and J. Sheasby. “The sticking of iron ore during reduction by hydrogen in a fluidized bed”. In: *Canadian Metallurgical Quarterly* 13.4 (1974), pp. 649–657.

[17] C. Lei, Q. Zhu, and H. Li. “Experimental and theoretical study on the fluidization behaviors of iron powder at high temperature”. In: *Chemical Engineering Science* 118 (2014), pp. 50–59.

[18] Y. Zhong, J. Gao, Z. Wang, and Z. Guo. “Influence of particle size distribution on agglomeration/defluidization of iron powders at elevated temperature”. In: *ISIJ International* (2017), ISIJINT–2016.

[19] B. Zhang, Z. Wang, X. Gong, and Z. Guo. “A comparative study of influence of fluidized conditions on sticking time during reduction of Fe2O3 particles with CO”. In: *Powder technology* 225 (2012), pp. 1–6.

[20] M. Komatina and H. W. Gudenau. “The sticking problem during direct reduction of fine iron ore in the fluidized bed”. In: *Metalurgija* 10 (2004), pp. 309–328.

[21] S. He, H. Sun, C. Hu, J. Li, Q. Zhu, and H. Li. “Direct reduction of fine iron ore concentrate in a conical fluidized bed”. In: *Powder Technology* 313 (2017), pp. 161–168.

[22] P. Wong, M. Kim, H. Kim, and C. Choi. “Sticking behaviour in direct reduction of iron ore”. In: *Ironmaking & steelmaking* 26.1 (1999), pp. 53–57.

[23] J. Li, R. Wei, H. Long, P. Wang, and D. Cang. “Sticking behavior of iron ore–coal pellets and its inhibition”. In: *Powder technology* 262 (2014), pp. 30–35.

[24] S. Li, D. Sanned, J. Huang, E. Berrocal, W. Cai, M. Aldén, M. Richter, and Z. Li. “Stereoscopic high-speed imaging of iron microexplosions and nanoparticle-release”. In: *Optics Express* 29.21 (2021), pp. 34465–34476.

[25] P. Tóth, Y. Ögren, A. Sepman, P. Gren, and H. Wiinikka. “Combustion behavior of pulverized sponge iron as a recyclable electrofuel”. In: *Powder Technology* 373 (2020), pp. 210–219.

[26] C. Xu and J. Zhu. “Experimental and theoretical study on the agglomeration arising from fluidization of cohesive particles—effects of mechanical vibration”. In: *Chemical Engineering Science* 60.23 (2005), pp. 6529–6541.

[27] Y. Zhong, Z. Wang, Z. Guo, and Q. Tang. “Prediction of defluidization behavior of iron powder in a fluidized bed at elevated temperatures: Theoretical model and experimental verification”. In: *Powder technology* 249 (2013), pp. 175–180.

[28] J. Seville, C. Willett, and P. Knight. “Interparticle forces in fluidisation: a review”. In: *Powder Technology* 113.3 (2000), pp. 261–268.

[29] G. C. Kuczynski. “Self-diffusion in sintering of metallic particles”. In: *Sintering Key Papers*. Springer, 1990, pp. 509–527.

[30] P. Knight, J. Seville, H. Kamiya, and M. Horio. “Modelling of sintering of iron particles in high-temperature gas fluidisation”. In: *Chemical engineering science* 55.20 (2000), pp. 4783–4787.

[31] K. Kuwagi, T. Mikami, and M. Horio. “Numerical simulation of metallic solid bridging particles in a fluidized bed at high temperature”. In: *Powder Technology* 109.1-3 (2000), pp. 27–40.

[32] S. Ergun. “Fluid flow through packed columns”. In: *Chem. Eng. Prog.* 48 (1952), pp. 89–94.

[33] P. Buffat and J. P. Borel. “Size effect on the melting temperature of gold particles”. In: *Physical review A* 13.6 (1976), p. 2287.

[34] Y. Dai, P. Lu, Z. Cao, C. T. Campbell, and Y. Xia. “The physical chemistry and materials science behind sinter-resistant catalysts”. In: *Chemical Society Reviews* 47.12 (2018), pp. 4314–4331.

[35] N. A. Dharanipragada, M. Meledina, V. V. Galvita, H. Poelman, S. Turner, G. Van Tendeloo, C. Detavernier, and G. B. Marin. “Deactivation study of Fe2O3–CeO2 during redox cycles for CO production from CO2”. In: *Industrial & Engineering Chemistry Research* 55.20 (2016), pp. 5911–5922.

[36] Y. Hidaka, T. Anraku, and N. Otsuka. “Deformation of iron oxides upon tensile tests at 600–1250 C”. In: *Oxidation of Metals* 59.1 (2003), pp. 97–113.

[37] L. Choisez, N. E. van Rooij, C. J. Hessels, A. K. da Silva, I. R. Souza Filho, Y. Ma, P. de Goey, H. Springer, and D. Raabe. “Phase transformations and microstructure evolution during combustion of iron powder”. In: *Acta Materialia* (2022), p. 118261.

[38] J. S. Marshall and S. Li. *Adhesive particle flow*. Cambridge University Press, 2014.

[39] G. C. Hadjipanayis and R. W. Siegel. *Nanophase materials: Synthesis-properties-applications*. Vol. 260. Springer Science & Business Media, 2012.

[40] A. Atkinson and R. Taylor. “Diffusion of 55Fe in Fe2O3 single crystals”. In: *Journal of Physics and Chemistry of Solids* 46.4 (1985), pp. 469–475.

[41] L. Himmel, R. Mehl, and C. E. Birchenall. “Self-diffusion of iron in iron oxides and the Wagner theory of oxidation”. In: *Jom* 5.6 (1953), pp. 827–843.

[42] D. Chicot, J. Mendoza, A. Zaoui, G. Louis, V. Lepingle, F. Roudet, and J. Lesage. “Mechanical properties of magnetite (Fe3O4), hematite (α-Fe2O3) and goethite (α-FeO·OH) by instrumented indentation and molecular dynamics analysis”. In: *Materials Chemistry and Physics* 129.3 (2011), pp. 862–870.

3

EXPERIMENTS ON REDUCTION

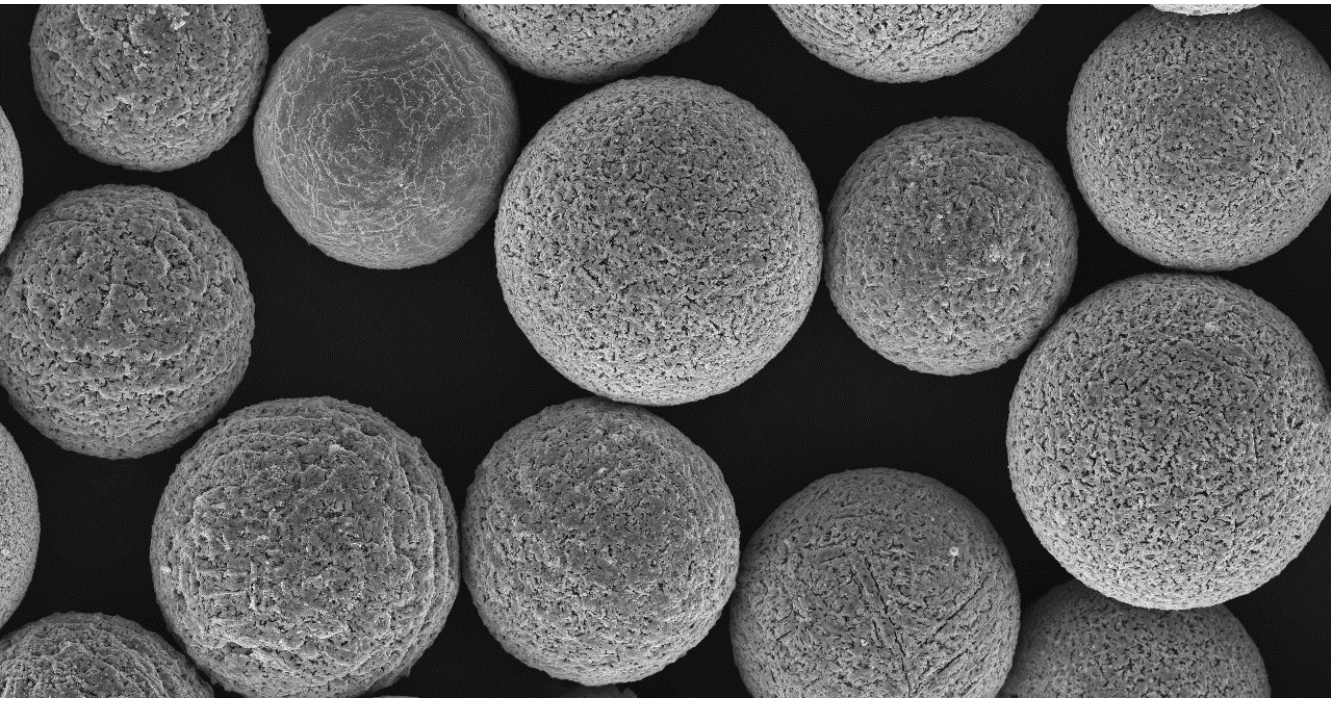

This chapter is based on: X. Liu, X. Zhang, J. Li, Q. Zhu, N. G. Deen, Y. Tang: Regeneration of iron fuel in fluidized beds Part II: reduction experiments. Powder Technology, 2023, https://doi.org/10.1016/j.powtec.2022.118183.

Abstract

Direct reduction of combusted iron powders using renewable energy is one of the keys to ensure a carbon-neutral iron fuel cycle. Based on (de-)fluidization experimental study in Chapter 2, reduction experiments of micron-sized combusted iron powders using hydrogen in a lab-scale gas-fluidized bed are conducted at temperatures ranging from 500 °C to 650 °C. The effects of temperature, hydrogen velocity and concentration on the reduction performance (including reduction degree, particle morphology and size change) and sintering/defluidization behavior are investigated. Overall, a reduction degree higher than 90% is reached at a lower temperature of 500 °C, whereas at higher temperatures the serious problem of particle sintering is encountered, which leads to quick defluidization and thus a relatively low reduction degree. Temperature has been found to have a pronounced effect on the sintering and reduction behavior, while the effect of gas velocity on the reduction process is negligible. SEM images show that the reduced powders are porous with the pore size increasing with temperature. These experimental findings provide insights for the design of industrial process of hydrogen-based regeneration of iron fuels.

3.1. Introduction

The consumption and generation of energy are two of the most significant features of modern civilization. The ongoing transition to low-carbon energy systems has intensified the creation of clean energy solutions. However, this transition still faces great challenges in finding effective and efficient clean energy carrier alternatives. Recently, metal powder has been proposed as a promising energy carrier to fulfill the void of existing fuels in applications where high energy density, ease of transportation, and/or reliable availability are needed [1, 2]. Metal fuels react energetically with the oxygen in air releasing a huge amount of heat and the resulting metal oxides can be collected and reduced back to metal powder closing a metal fuel cycle.

Micron-sized iron powder has been considered a promising candidate for such a metal fuel cycle due to its high volumetric energy density and abundance features. The energy is generated by a 'clean' combustion process [3] with the only solid products, i.e., iron oxides. To fulfill a carbon-neutral fuel cycle, regeneration of the metallic iron from the combustion product (iron oxides) using renewable energy (e.g. green hydrogen) is crucial. Therefore, a fundamental understanding of the reduction mechanisms of the combusted iron powders becomes important.

Fluidization is a promising technology for thermochemical reduction of iron oxide powder because of its high fluid-solid contact efficiency, and excellent heat and mass transfer characteristics [4, 5]. Direct reduced iron (DRI) based on fluidized bed technologies has been developed over the last few decades in the iron and steel industries. Regarding the reducing agent, hydrogen has been proven to be a good reductive agent due to its environment-friendly feature [6–9], and has become more important in DRI processes [10–13]. A proven industrial direct reduction process is using hydrogen in a fluidized bed, i.e. the Circored® process [14].

Depending on the reaction temperature, the process of DRI with hydrogen occurs either in two or three steps. When the temperature is higher than 570 °C, the reduction process follows in three steps: hematite (Fe_2O_3) → magnetite (Fe_3O_4) → wüstite (FeO) → metallic iron (Fe). On the other hand, below 570 °C the reduction occurs in two steps: hematite (Fe_2O_3) → magnetite (Fe_3O_4) → metallic iron (Fe), owing to wüstite not being stable below 570 °C. It is generally accepted that the reduction takes place stepwise from iron with high valence to metallic iron [15]. Spreitzer et al. [11] studied the three-step reduction process of Fe_2O_3 to Fe, and theoretically derived the multistep analysis method in a temperature range 600 – 800 °C. Based on the multistep analysis method, He et al. [16] further established the detailed reaction kinetics. Extensive study has focused on the effect of temperature on the reduction performance. Many research reported that the reduction rate increases with the temperature [11, 16, 17].

High temperature however, also provides a favorable situation for the formation of agglomerates due to sticking or sintering behavior of solid particles, which may eventually lead to a defluidization of the bed [18–20]. For thermochemical reduction of iron oxides, previous research has reported the sintering and agglomeration issue [21–24]. These unintentional agglomerations occur when particles have a strong tendency to stick together due to certain harsh operation conditions [22, 25]. It is well accepted that the sticking occurs mostly during the metallization of iron ore, which highly depends on the properties of the raw materials. Previous efforts have been made on studying the factors that affect

the sticking problem [26–28]. These pointed out that the sticking issue would be affected by both the operation conditions (e.g., reducing gas, temperature, and velocity) and the physical properties of particles (e.g., composition, geometry, size, and morphology).

As mentioned in Chapter 2 of this work [29], existing studies are highly concentrated on the reduction and/or fluidization of raw iron ores (for applications in the iron and steel industries), which presents a wide variation in size, impurities contents, etc. However, for the application of metal fuel, iron oxides of micron size that are directly collected from iron combustion are of interest. These powders possess different properties from the materials (raw iron ores) studied in the existing literature. That is, the fine powder has a different size (in μm), composition (high purity oxides) and morphology (rather smooth). These unique characteristics make it necessary to focus on the study of combusted iron fines. Thus in this chapter, we aim to study the reduction behavior of combusted iron powders in a fluidized bed for regeneration of metal fuel. The objective of this analysis is to improve the understanding of the impact of different process parameters on the entire reduction process (fluidization behavior, reduction degree, and evolution of particle size and morphology), and therefore, provide some guidance on practical design of industrial process in the metal fuel cycle. The insights on (de-)fluidization behavior of the combusted iron powder gained from experimental study in Chapter 2 are used in the design of reduction experiments.

This Chapter is organized as follows: introduction of the setup and the experimental conditions in Section 3.2, followed by the results in Section 3.3 including reduction degree and characteristics of the reduced powder, and finally conclusions are presented in Section 3.4.

3.2. Experiments

3.2.1. Experimental materials

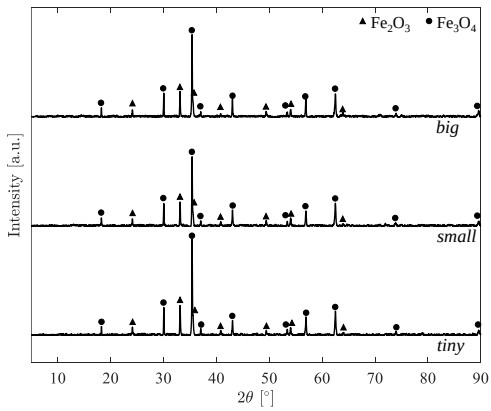

Figure 3.1: XRD partterns of the raw materials.

Table 3.1: Information of particle size, total iron content, and the minimum fluidization velocity of raw materials.

Particle size	d50 [μm]	W_0(TFe) [wt%]	u_{mf,H_2} [m/s]
tiny	33.7	72.19	0.0056
small	45.5	71.04	0.0095
big	58.0	71.93	0.0182

The particles used in this reduction investigation are identical to those used in Chapter 2 (i.e. *tiny*, *small*, and *big*). Figure 3.1 shows the XRD patterns of the raw materials, which indicates that the combusted powders are composed of hematite and magnetite in a weight ratio of roughly 40:60. The total iron content of the combusted powder is obtained by the titration method according to the Chinese standard of GB/T6730.65-2009. The obtained values are listed in Table 3.1.

3.2.2. Apparatus and procedures

A laboratory-scale quartz cylinder fluidized bed is employed to investigate the reduction behavior of combusted iron powder (see Figure 3.2). The cylindrical fluidized bed has a height of 960 mm and an inner diameter of 16 mm. A porous quartz plate with a uniform pore diameter of 0.15 mm is used as the gas distributor at the bottom of the reactor.

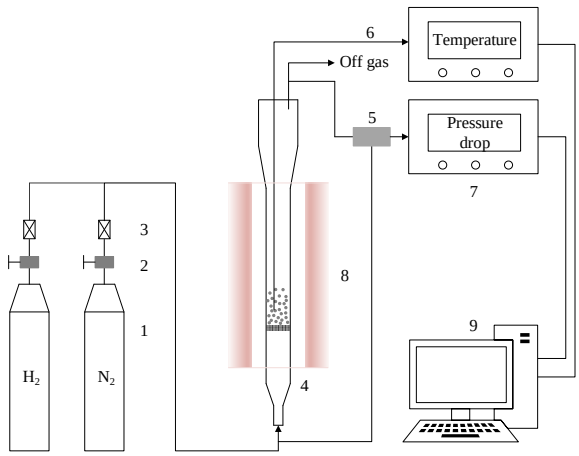

Figure 3.2: Schematic overview of the experimental setup for the reduction process (1-Gas cylinder; 2-Shut-off valve; 3-Mass flow controller; 4-Fluidized bed reactor; 5-Differential pressure sensor; 6-Thermocouple; 7-Display instruments; 8-Electric resistance furnace; 9-Data acquisition system).

Before the reduction experiments, the minimum fluidization velocities (u_{mf}) under 100% H_2 atmosphere at room temperature are measured, which is shown in Table 3.1. For all reduction tests, 10.0 g of combusted iron powders are first fed into the fluidized bed reactor at a lower temperature and purged with N_2 to remove air from the system. Then a furnace around the bed is switched on, heating up the bed to the desired temperature. Such heating process is conducted under N_2 atmosphere with a specific gas flow rate depending on the operation condition. When the temperature of the bed reaches the pre-set value,

the required gas (H_2) and its flow rate are switched to the required operation condition immediately, and the time of which is assumed as the starting point of the reduction process. After a specific reduction time or when the defluidization occurs (pressure drop decreases sharply), the experiments are terminated by switching the hydrogen supply back to nitrogen supply only. Then the reactor can be removed from the furnace and quenched directly by spraying water on its outer surface until room temperature is reached. The reduced sample is collected and stored in a ziplock bag for further measurements.

3.2.3. Experimental conditions

According to the outcomes in Chapter 2 [29], defluidization of the combusted iron powder may occur due to severe sintering effect at temperatures higher than 650 °C. Therefore, the reduction experiments are designed at temperatures ranging from 500 °C to 650 °C. Different gas velocities are used ranging from $8u_{mf}$ to $12u_{mf}$ with u_{mf} determined for the individual size of powder under H_2 environment at room temperature. With such hydrogen flow rates there is always an excess of hydrogen, since a full bed conversion consuming all hydrogen fed would require less than 10 minutes.

3.2.4. Calculation of the reduction degree

The reduction degree (RD) is defined as the ratio of actual mass loss and the theoretical maximum mass loss. Initially RD = 0, and for a complete conversion to metallic iron RD = 1. Due to the small amount of powder used in our experiments, direct weighing of the final product would induce large errors. Thus, the RD is determined via eq. (3.1) using the measured weight content of total iron content in the initial (W_0(TFe)) and reduced (W_{end}(TFe)) samples. Note that we assume that the sample only contains the elements of Fe and O, which is valid because of the high purity (> 99%) of the iron powder used in the combustion process.

$$\mathrm{RD} = \frac{1 - W_0(\mathrm{TFe}) \big/ W_{end}(\mathrm{TFe})}{1 - W_0(\mathrm{TFe})} \tag{3.1}$$

3.3. Results and discussions

3.3.1. Fluidization and reduction performance

In this section, we investigate the effects of operation conditions on fluidization and reduction performance of the combusted iron powders. To this end, we analyze the results in terms of defluidization time (t_{def}) and reduction degree (RD). Defluidization time is obviously defined as the period from switching on the reducing gas to the moment defluidization occurs indicating by a sharp decrease of the bed pressure drop (see Chapter 2). The reduction degree is determined for the reduced powder after completion of the experiments, which is either after the occurrence of defluidization or after a pre-set reaction time.

Effect of temperature

Figure 3.3 shows the reduction degree and defluidization time of the products of the reduced particles of different sizes at temperatures ranging from 500 °C to 650 °C using 100% H_2 and $u_0 = 8u_{mf}$ (0.0448 m/s for *tiny* powder, 0.076 m/s for *small* powder and 0.1456 m/s for *big* powder). Correspondingly, the XRD results of the reduced powder are shown in Figure 3.4. As expected, the temperature has a significant influence on the reduction process. For all particle sizes, defluidization occurs quicker with increasing temperature (see Figure 3.3(b)), resulting in a decreasing reduction degree (see Figure 3.3(a)). An almost complete reduction (RD ≈ 95%) is achieved for all the particle types at the relatively low temperature 500 °C when defluidization occurs. This is confirmed by the XRD results in Figure 3.4, where only at 500 °C all the reduced powder is pure iron. In contrast, particle sintering at higher temperatures hinders the process, resulting in a decreasing reduction degree when defluidization occurs.

Figure 3.3 shows that larger particles seem to be reduced much faster leading to higher reduction degrees at lower temperatures of 500 °C and 550 °C, whereas this is not very obvious at higher temperatures of 600 °C and 650 °C. Note that gas velocities used for experiments of different powder sizes are varied. Consequently, higher hydrogen flow rate for larger particles results in higher reduction degree at the same reduction time. However, at higher temperatures, the acceleration of reaction rate by temperature is more pronounced than the effect of hydrogen flow rate. Thus at 600 °C and above, the reduction degree of different powder sizes does not show significant variation as the reduction time is roughly equivalent.

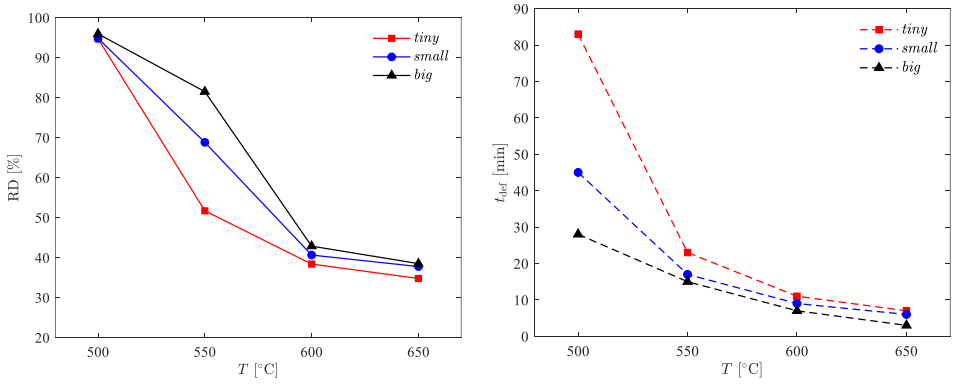

Figure 3.3: (a) Reduction degree (RD) as a function of operation temperature (T) at the moment defluidization sets in (t_{def}); (b) Time until defluidization (t_{def}) as a function of operation temperature (T). Using 100% H_2 with $u_0 = 8u_{mf}$. Specifically, 0.0448 m/s for *tiny* powder, 0.076 m/s for *small* powder, and 0.1456 m/s for *big* powder.

The observed trends can be explained as follows. Since the particles are quite small, the particle Reynolds numbers are rather small, i.e., $Re_p << 1$. This implies that the reduction degree is limited by external mass transfer. Increasing the specific surface area available for mass transfer (i.e. smaller particles) or increasing the mass transfer coefficient (i.e.

higher flow rates) should lead to faster reduction degrees. So far, the gas velocity is kept as $8u_{mf}$, so if the particle size is increased, simultaneously the particle specific surface area is reduced (RD should reduce) while the flow rate is increased (RD should increase). The net effect of these competing phenomena is that the RD reduces.

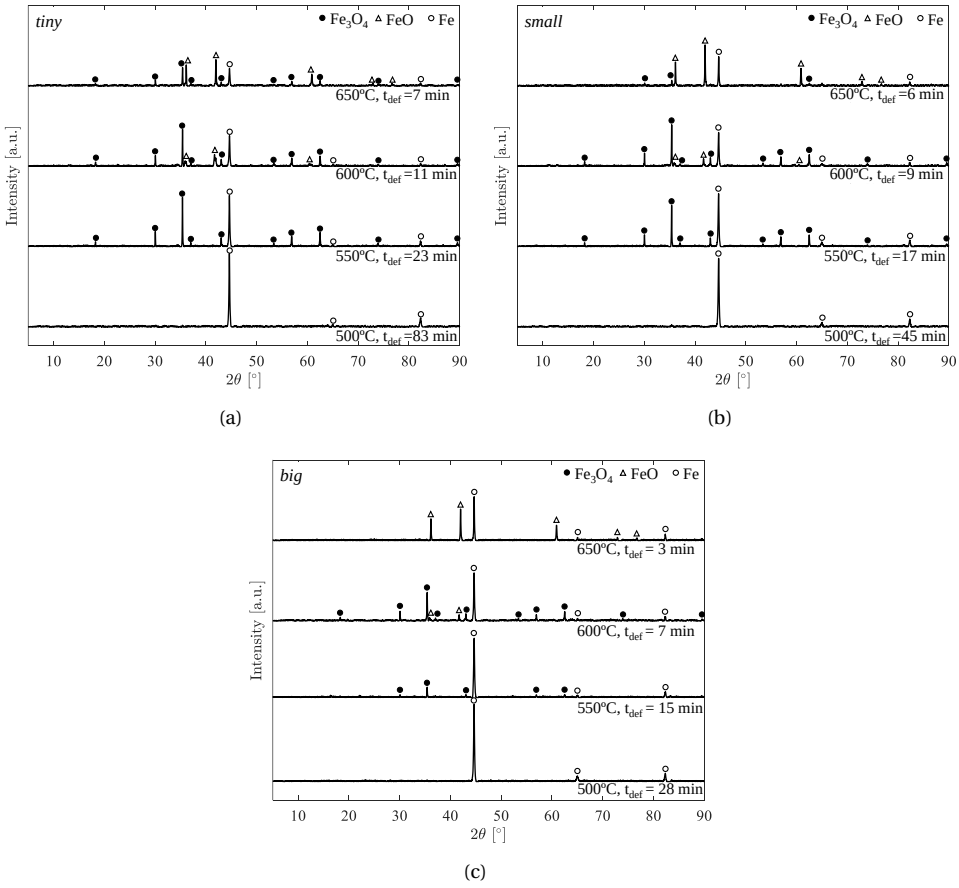

Figure 3.4: XRD patterns of the reduced particles at different operating temperatures for *tiny* (a), *small* (b) and *big* (c) particle sizes.

We further conduct several tests at 550 °C applying the same gas superficial velocity of 0.0448 m/s, to test if indeed the RD increases for smaller particles as expected. The results of reduction/defluidization time and reduction degree are given in Table 3.2. In this case, defluidization occurs earlier for larger particles, resulting in smaller reduction degree. Quantitatively, the increase of reduction degree from *big* to *small* to *tiny* particles is much more pronounced than the corresponding increase of reduction time. This may imply that smaller particles are indeed reduced in a faster rate as expected. Moreover, one-to-one comparison between Table 3.2 and Figure 3.3 for *small* and *big* particles indicates that when the gas velocity decreases (e.g. from 0.1456 m/s to 0.0448 m/s for *big* particles),

the defluidization time slightly decreases (15 min to 13 min), but the reduction degree is significantly decreased (81.49% to 21.09%). This confirms the effect of gas flow rate on the reduction process which was mentioned above for observation in Figure 3.3. As for the defluidization time, lower gas velocity would decrease the collision frequency and therefore increase the possibility to form agglomerates, thus slightly faster defluidization.

Table 3.2: Effect of the particle size on the reduction process.

Particle size [−]	H_2+N_2 [%]	Temperature [°C]	Velocity [m/s]	Reduction time [min]	RD [%]
tiny	100+0	550	0.0448	23 (defluidization)	51.69
small	100+0	550	0.0448	16 (defluidization)	30.73
big	100+0	550	0.0448	13 (defluidization)	21.09

Furthermore from the XRD analysis in Figure 3.4, we see that raw materials are mainly transformed into magnetite, wüstite and iron at temperatures of 600 °C and 650°C, whereas at the temperature of 500 °C and 550 °C there is no presence of intermediate phase wüstite (FeO). This is consistent with the literature with respect to the different reduction mechanisms below/above 570 °C. Another clear observation is that even at extremely short reduction times, e.g., 3 min for big particles at 650 °C, Fe_2O_3 does not exist anymore. This implies that the conversion from Fe_2O_3 to Fe_3O_4 is a very fast reaction. Assuming a theoretically full conversion of Fe_2O_3 to Fe_3O_4, the reduction degree is 11%. This could be achieved within a few minutes of reduction.

To further analyze how the temperature affects the reaction rate, more tests have been conducted at temperatures of 500 °C and 550 °C for *tiny* particles with 100% H_2 at different pre-set reduction times. The reduction time is defined as the period from switching on the reducing gas to the moment reaching the pre-set reduction time. The evolution of the reduction degree is shown in Figure 3.5, whereas the corresponding XRD results of the reduced powder are shown in Figure 3.6. The larger slope at 550°C indicates a faster reaction with a higher reaction rate. Thus, metallic iron would be emerging quicker at the outer surface of the particles. These newly generated metallic iron grains will accelerate particle sintering and eventually defluidization. Consequently, at temperature 550°C and above, defluidization always occurs earlier than the time required for a full reduction to metallic iron. Combining the results based on Figure 3.3 and Figure 3.5, we can conclude that a higher temperature can accelerate the reaction rate, while a lower temperature is beneficial to prevent accelerated sintering/defluidization. These conflicting effects of temperature should be carefully considered when designing the reduction process. Furthermore, at all the applied temperatures, defluidization occurred earlier than full reduction is reached.

The phase transformation over reduction time shown in Figure 3.6 again confirms the observations/conclusions from Figure 3.4: 1) below 570 °C there is no intermediate step of conversion to wüstite (FeO); 2) the conversion from hematite to magnetite is a very fast reaction step.

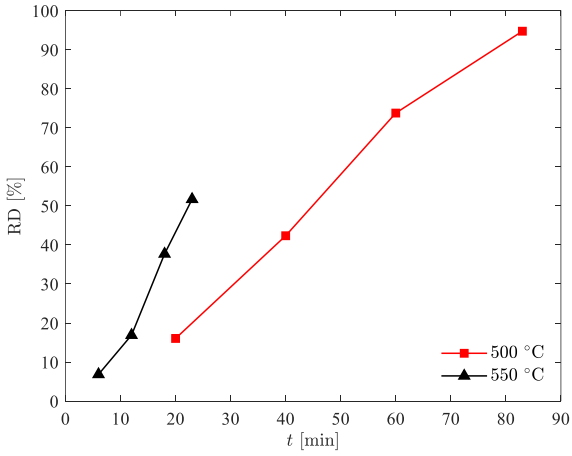

Figure 3.5: Reduction degree as a function of reduction time for *tiny* powder at 500 °C and 550 °C, using 100% H_2 with $u_0 = 8u_{mf}$ (=0.0448 m/s.)

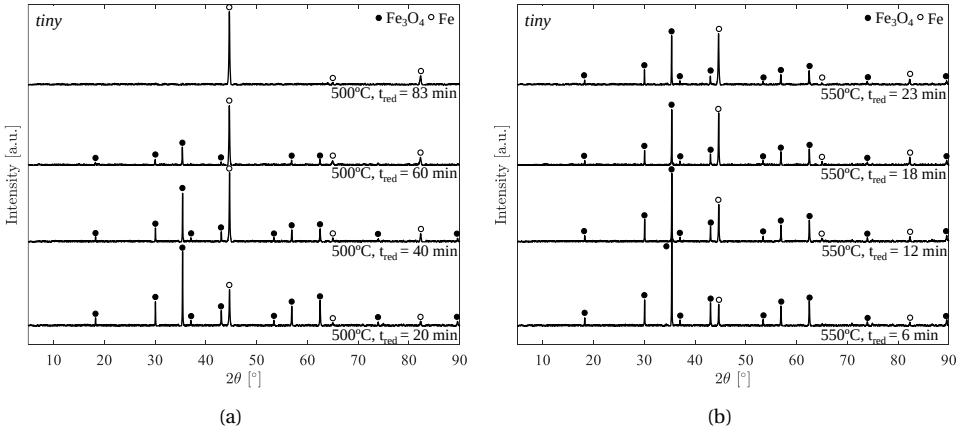

Figure 3.6: XRD patterns of the reduced particles at different reduction time for *tiny* powder, (a) 500 °C, (b) 550 °C.

Effect of hydrogen velocity and concentration

To analyze the effect of the gas velocity on the reduction process and the defluidization behavior, gas velocities i.e., $8u_{mf}$, $10u_{mf}$ and $12u_{mf}$ are tested in 100% H_2 atmosphere. The reduction temperature is chosen as 500 °C since at this temperature all particle sizes can fluidize for a relatively long time. Figure 3.7 compares the resulting reduction degree and the defluidization time for *tiny*, *small*, and *big* particles. It is observed that when increasing the gas velocity from $8u_{mf}$ to $12u_{mf}$, the maximum reduction degree slightly decreases, with a total change of roughly 6%. This decrease in reduction degree is attributed to the shorter reduction time (equivalent to the defluidization time as shown in Figure 3.7(b)).

The faster defluidization due to increasing gas velocity shown in this figure does not seem to match our findings for fluidization of combusted iron powder in Chapter 2 [29], where the defluidization is slightly influenced by gas velocity. Note that in the current experiments the reduction speed is also influenced by increasing gas velocity, especially at lower temperatures. As discussed in Section 3.3.1, increasing gas velocity at lower temperatures leads to a significantly higher reduction degree. This means the generation of metallic iron at the particle surface is faster at higher gas velocity, which thus accelerates the sintering when particles come into contact. To conclude, the overall fluidization behavior is determined by the competing effects of gas velocity (similar to temperature) on the chemical reaction and the hydrodynamic interactions. Finding an optimal gas velocity is critical to the entire reduction process as well as the fluidization behavior.

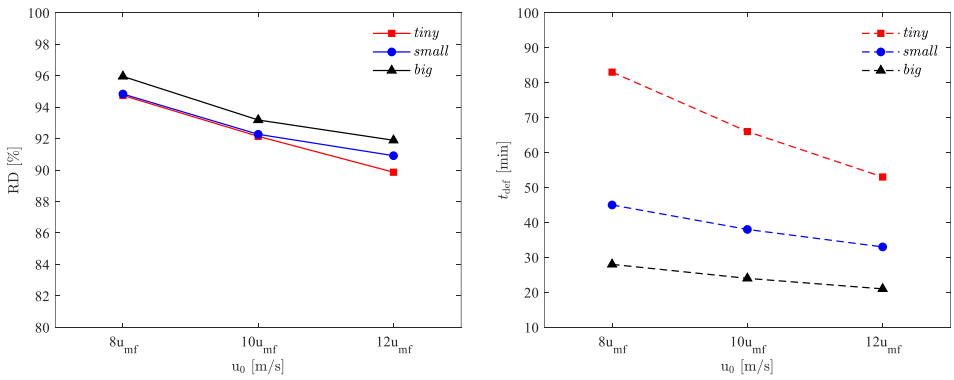

Figure 3.7: Maximum reduction degree (RD) and defluidization time (t_{def}) as a function of gas superficial velocity for all sizes of particles at 500 °C, using 100% H_2.

Table 3.3 compares results when applying 100% hydrogen and 50% hydrogen diluting in a nitrogen atmosphere. As expected, the partial pressure of hydrogen plays an important role in determining the reaction rate. The reduction degree of 100% H_2 reduction for 60 minutes reaches 73.77%, while the reduction degree of 50% H_2 reduction for 60 minutes is only 31.24%. This gives a dependence of reaction rate on hydrogen concentration with an order of 1.24, which is very closed to the order of 1.4 reported in the work of Hessels et al. [30].

Table 3.3: Effect of the hydrogen concentration on the reduction degree for *tiny* powders.

Particle size [−]	Temperature [°C]	Velocity [m/s]	H_2+N_2 [mol%]	Reduction time [min]	RD [%]
tiny	500	$8u_{mf}$	100 + 0	60	73.77
		$8u_{mf}$	50 + 50	60	31.24

Kinetics analysis

To retrieve kinetic data from the experiments, the approach developed by Hancock and Sharp [31] is applied. The benefit of this method is that the only data required to derive the reaction rate is conversion-time data, and this approach has been successfully used by many previous research related to the reduction of iron oxides [30, 32–34]. This model describes the solid-state reactions follow the form:

$$X = 1 - e^{-(kt)^n} \tag{3.2}$$

where X is the metal conversion at time t; k is the reaction rate constant; n is the kinetic exponent.

By integrating eq. (3.2) and plotting of ln[-ln(1-X)] against ln(t), the kinetic exponent (n) and reaction rate constant (k) can be obtained from the slope and intercept of a linear function, respectively:

$$\ln[-\ln(1-X)] = n\ln t + n\ln k \tag{3.3}$$

The kinetic exponent n depends on the mechanism of growth and the dimensionality of the nuclei. Generally when $n < 1$, the mechanism is diffusion controlled; when n is close to 1, the mechanism approaches a phase boundary reaction kinetic controlled mechanism, and when n is close to 2 the mechanism is well represented as a nucleation model.

At temperatures below 570 °C, the reduction follows $Fe_2O_3 \rightarrow Fe_3O_4 \rightarrow Fe$. Figure 3.6 shows that at the initial stage of the reduction process (i.e. t = 20 min at 500 °C and t = 6 min at 550 °C), the reduction of Fe_2O_3 to Fe_3O_4 has been already completed. Thus, after this point, the reduction process only follows single-step reaction from Fe_3O_4 to Fe. Fitting the experimental data shown in Figure 3.5, the kinetic exponent n is obtained 1.97 at 500 °C, and 1.75 at 550 °C as shown in Figure 3.8. Since the obtained values of n are close to 2, the reduction mechanism of Fe_3O_4 to Fe is concluded to be nucleation growth controlled.

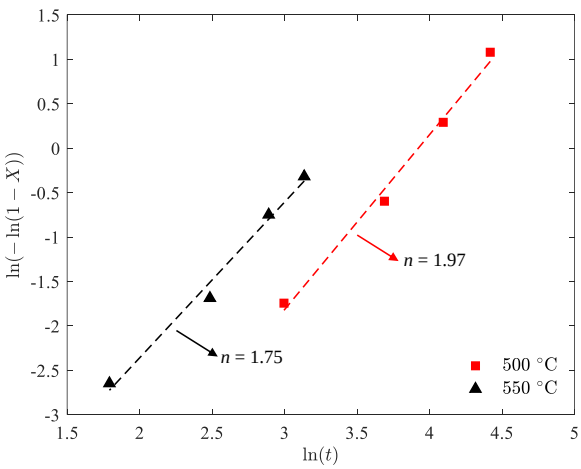

Figure 3.8: The curves of ln[-ln(1-X)] versus ln$t$ for extracting the kinetic exponent n for *tiny* powder.

Meanwhile, the obtained values ($n(T)$ and reaction rate constant $k(T)$) can be further used to determine the activation energy (E_a) of the reaction process according to an Arrhenius expression (eq. (3.4)). The resulting activation energy (E_a) is 61.02 kJ/mol, which is close to the results reported by previous studies [35, 36]. The obtained pre-exponent factor (k_0) is 4.37 s^{-1} for *tiny* particles.

$$k(T) = k_0 \exp\left(-\frac{E_a}{RT}\right) \tag{3.4}$$

3.3.2. Characteristics of reduced powder

Morphology

The structural changes at the outer surface and the internal structure of the particles during the reduction process can be analyzed by means of a scanning electron microscope (SEM). Figure 3.9(a)-3.9(h) show the morphology of samples (*tiny* powder) being reduced at different temperatures. The surface morphology of the raw *tiny* powder is shown in Figure 3.9(i) as reference, which presents a relatively smooth and dense surface structure. In contrast, the reduced particles generally present a porous structure due to the generated metallic iron crystals. The pore size highly depends on the reduction temperature, i.e., the pore size increases with increasing temperature. During the reduction process, the microstructure change is complex and can be influenced by two aspects: i) the decomposition rate of iron oxide (chemical reaction); ii) the migration of iron ions [37]. At low temperatures, the diffusion rate of iron ions is relatively lower than the decomposition rate of iron oxide occurring at the reaction interface, causing the increase in the surface Fe/O ratio. Thus, the surface becomes supersaturated with iron ions. Eventually a large amount of iron ions nucleate at the surface, which forms a relatively dense layer of metallic iron through growth and coalescence. As the temperature increases, the migration of iron ions goes faster, resulting in larger pores. Apart from that, wüstite is present as an intermediate product when the temperate is higher than 570 °C, which would influence the product morphology. Additionally, at high temperatures the surface structure seems rougher, which would increase the possibility of forming agglomerates.

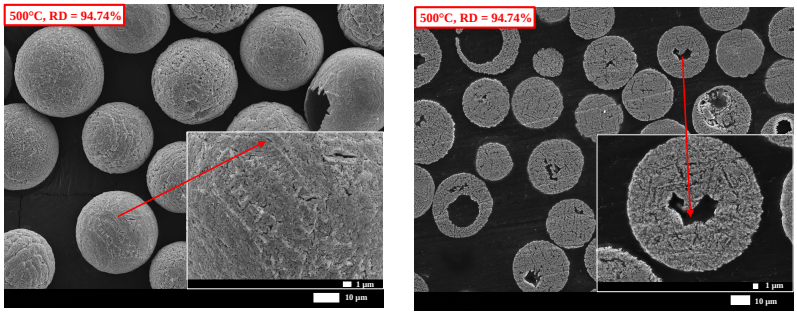

(a) (b)

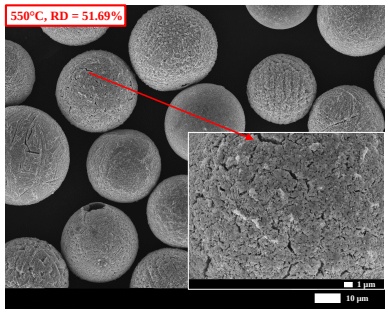

(c)

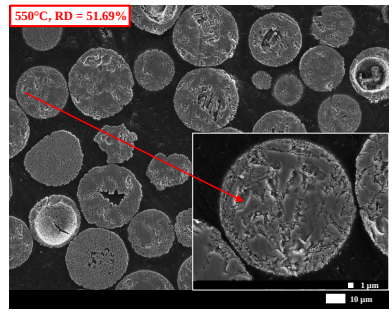

(d)

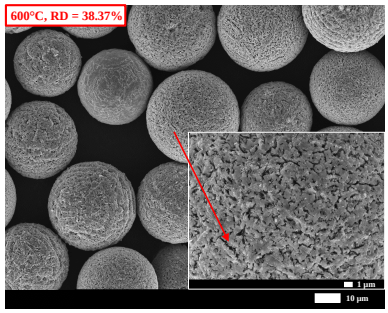

(e)

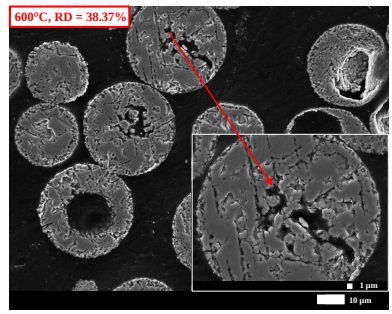

(f)

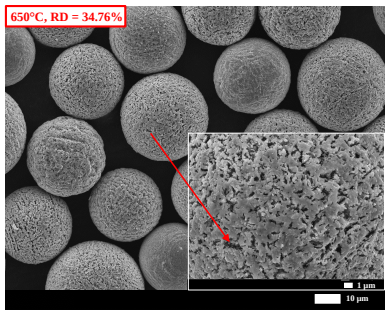

(g)

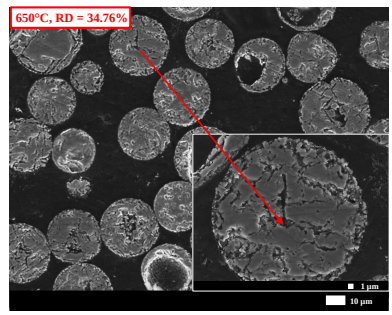

(h)

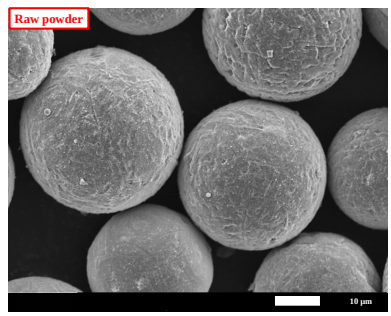

(i)

Figure 3.9: Effect of the reduction temperature on the surface morphology (left) and on the cross-section morphology (right) (samples of *tiny* powder).

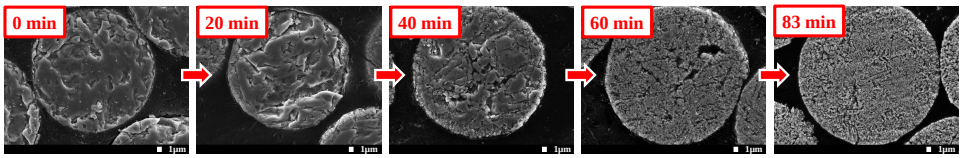

Figure 3.10: Effect of the reduction time on the cross-section morphology (*tiny* powder samples), at 500 °C.

Comparing the surface morphology (left figures) to the cross-section morphology (right figures) in Figure 3.9, we see that the particle surface becomes porous and rough as soon as the reaction takes place, whereas the particle inner structure remains dense and smooth and gradually becomes porous till a full conversion is reached. This can be further verified by the evolution of cross-section morphology shown in Figure 3.10 for the powder being reduced at 500 °C. It can be clearly seen that during the reduction, the generated metallic iron grains first emerge on the surface forming a thin porous layer. Then the inside dense (unreacted) part gradually becomes porous during the process of reduction. At the end of the reduction process, the particle becomes porous everywhere and the voids are mostly interconnected, indicating a complete reduction. This porous structure may slightly influence the subsequent combustion process. The general combustion process of the iron particle follows the main steps of 1) igniting the iron particles in the solid state; 2) melting of the particle and subsequent oxidation in the liquid state; 3) solidification of the iron oxide droplet [38]. Since the particle quickly liquefies, the effect of the porosity after reduction is limited to the ignition phase [39]. Future efforts are required to quantitatively measure the porosity evolution during the reduction.

Mean particle size of the reduced samples

A particle size analyzer (CAMSIZER X2) is applied to measure the size of raw and reduced powder. The CAMSIZER X2 produces a particle flow which is characterized by an optical system with high resolution. Since the resolution of the analyzer is 0.8 µm per pixel, which is much smaller than the particle size ($< 0.025 d50_{tiny}$), the measurement based on this analyzer can be applied to quantitatively analyze the particle size change during reaction. Figure 3.11 shows the mean particle size (d50) and its deviations (d10 and d90) normalized by the mean diameter of the raw powder ($d50_{raw}$) for the reduced samples with different sizes at different temperatures. Note that the results in the figure are obtained at $8u_{mf}$ until the defluidization point. Similarly, Figure 3.12 shows the normalized size of the three powders reduced with different times at 500 °C.

From Figure 3.11, we can see that when completely reduced to metallic iron at 500 °C, the size of the particles decreases, whereas the particle size slightly increases with an incomplete reduction at higher temperatures. Also in Figure 3.12 the size change of the *tiny* particles shows a first increase and then decrease at the reduction temperature of 500 °C. In literature the particle swelling phenomenon has been attributed to three mechanisms: crystal transformation theory, iron whisker theory, and the carbon deposition theory [40]. The carbon deposition theory can be excluded here obviously because no carbon is involved in our experiments. Zhang et al. [41] also reported that the iron whisker is commonly observed by CO reduction means and suppressed in the H_2 reduction condi-

tion. Therefore, the particle swelling observed in current study should be due to the varied structure of the crystal transformations.

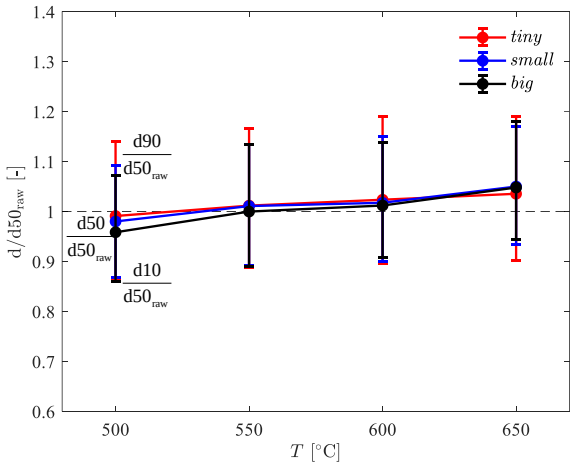

Figure 3.11: Particle size change ($d10/d50_{raw}$, $d50/d50_{raw}$, and $d90/d50_{raw}$) against temperature with deviations representing $d10/d50_{raw}$ and $d90/d50_{raw}$.

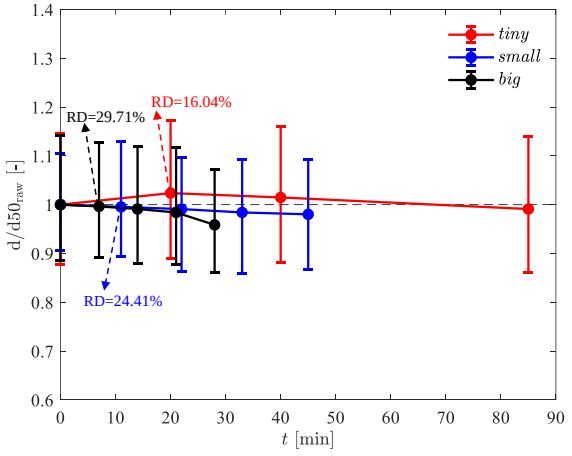

Figure 3.12: Particle size change ($d10/d50_{raw}$, $d50/d50_{raw}$, and $d90/d50_{raw}$) against reduction time at 500°C with deviations representing $d10/d50_{raw}$ and $d90/d50_{raw}$.

In the initial stage of the reduction, hematite is quickly reduced to magnetite, resulting in a lattice structure transforming from the hexagonal lattice structure to the cubic lattice structure. As a consequence, the volume increases, and cracks may occur in the outer surface due to this volume expansion. In the middle and the latter stage of the reduction process, oxygen diffuses from the iron/wüstite interface to the iron/gas interface through the dense iron layer. Such behavior would cause the fracture of the dense iron layer

and the disintegration of iron grains. Eventually, a large number of small fragments are formed which in turn continues the swelling process [42]. Additionally, such volume increase due to the disintegration is more notable at higher temperatures. This swelling behavior at high temperature situation can also explain that the outer surface structure becomes more porous at higher temperatures (see Figure 3.9). As the reduction reaction continues, the interconnection/bonding between the small fragments enhances the iron phase formation, and the accumulation of the dense iron phase leads to the volume contraction. This evolution of particle size (first swelling then shrinking) is particularly visible for the reduction of *tiny* powder at 500°C in Figure 3.12, where the entire reduction process is tracked. Unfortunately this transition is not visible for small and big powders in Figure 3.12, simply because the reduction degree at these first experimental points has largely exceeded the theoretical value (11%) assuming a complete conversion from hematite to magnetite only. Therefore, the densification of more newly generated metallic iron grains would eliminate the volume increase from the phase transformation, ultimately resulting in a slightly unchanged or smaller volume.

Overall, the completely reduced powder at 500 °C possesses less than 10% size shrinkage after undergoing through an evolution from volume swelling (Fe_2O_3 to Fe_3O_4 phase transform) to volume contraction (densification of generated metallic iron grains). However, we are not certain if the size reduction also applies to the completely reduced powder at higher temperatures, as of more pronounced volume expansion due to disintegration of iron grains at higher temperatures as mentioned above. This is also reflected by the results at higher temperatures in Figure 3.11, even though the RD has far exceeded 11% for a full conversion from Fe_2O_3 to Fe_3O_4. Unfortunately this cannot be investigated in current work because experiments at higher temperatures always encounter defluidization much earlier before a possible full reduction.

3.4. Conclusions

We have conducted reduction experiments of combusted iron powders in a lab-scale fluidized bed using hydrogen with the aim to provide insights on how the operation conditions affect the fluidization and reduction performance. The main conclusions are:

1. Operational temperature is crucial to both fluidization behavior and reduction performance. Increasing temperature has a dual effect, i.e., accelerating the reaction rate and accelerating the particle sintering or bed defluidization. As a consequence, a low reduction degree is usually obtained at high temperature condition because of early defluidization of the bed. For all particle sizes, a complete reduction to metallic iron can be achieved at 500 °C.

2. Similarly, there also exist competing effects of the reducing gas velocity on the process. A higher gas velocity can enhance the hydrodynamic interactions (particle collisions, drag force) which might break the agglomerates and thus delay the defluidization. On the other hand, especially at lower temperatures a higher gas velocity leads to a higher reduction degree, generating more metallic iron which accelerates the sintering and defluidization.

3. The reduction temperature shows an evident influence on the surface structure of the reduced particles. Specifically, the particles reduced at a higher temperature present rougher surfaces with larger pores, and this surface structure provides a favorable condi-

tion for the formation of agglomerates.

4. During reduction, the particle size first undergoes swelling (due to crystal transformation from Fe_2O_3 to Fe_3O_4 and disintegration of iron grains) and then shrinking (due to the densification of the newly produced metallic iron grains). The mean size of final reduced powder at temperature of 500 °C is slightly smaller than the original oxides.

Bibliography

[1] J. M. Bergthorson, S. Goroshin, M. J. Soo, P. Julien, J. Palecka, D. L. Frost, and D. J. Jarvis. “Direct combustion of recyclable metal fuels for zero-carbon heat and power”. In: *Applied Energy* 160 (2015), pp. 368–382.

[2] J. M. Bergthorson. “Recyclable metal fuels for clean and compact zero-carbon power”. In: *Progress in Energy and Combustion Science* 68 (2018), pp. 169–196.

[3] D. Ning, Y. Shoshin, J. A. van Oijen, G. Finotello, and L. de Goey. “Burn time and combustion regime of laser-ignited single iron particle”. In: *Combustion and Flame* 230 (2021), p. 111424.

[4] S. Cloete, S. T. Johansen, and S. Amini. “Grid independence behaviour of fluidized bed reactor simulations using the Two Fluid Model: Effect of particle size”. In: *Powder Technology* 269 (2015), pp. 153–165.

[5] S. Schneiderbauer, A. Aigner, and S. Pirker. “A comprehensive frictional-kinetic model for gas–particle flows: Analysis of fluidized and moving bed regimes”. In: *Chemical Engineering Science* 80 (2012), pp. 279–292.

[6] H. K. Pinegar, M. S. Moats, and H. Y. Sohn. “Process simulation and economic feasibility analysis for a hydrogen-based novel suspension ironmaking technology”. In: *steel research international* 82.8 (2011), pp. 951–963.

[7] F. Chen, Y. Mohassab, T. Jiang, and H. Y. Sohn. “Hydrogen reduction kinetics of hematite concentrate particles relevant to a novel flash ironmaking process”. In: *Metallurgical and Materials Transactions B* 46.3 (2015), pp. 1133–1145.

[8] K. Piotrowski, K. Mondal, H. Lorethova, L. Stonawski, T. Szymański, and T. Wiltowski. “Effect of gas composition on the kinetics of iron oxide reduction in a hydrogen production process”. In: *International Journal of Hydrogen Energy* 30.15 (2005), pp. 1543–1554.

[9] W. Liu, H. Zuo, J. Wang, Q. Xue, B. Ren, and F. Yang. “The production and application of hydrogen in steel industry”. In: *International Journal of Hydrogen Energy* 46.17 (2021), pp. 10548–10569.

[10] X. Zhang, S. He, H. Sun, Q. Zhu, J. Li, and H. Li. “Mechanism of surface morphology evolution in the reduction of fine iron ore in a conical fluidized bed reactor”. In: *Chemical Engineering Science* 220 (2020), p. 115468.

[11] D. Spreitzer and J. Schenk. “Iron ore reduction by hydrogen using a laboratory scale fluidized bed reactor: kinetic investigation—experimental setup and method for determination”. In: *Metallurgical and Materials Transactions B* 50.5 (2019), pp. 2471–2484.

[12] D. Spreitzer and J. Schenk. “Fluidization behavior and reducibility of iron ore fines during hydrogen-induced fluidized bed reduction”. In: *Particuology* 52 (2020), pp. 36–46.

[13] S.-H. Kim, X. Zhang, Y. Ma, I. R. Souza Filho, K. Schweinar, K. Angenendt, D. Vogel, L. T. Stephenson, A. A. El-Zoka, J. R. Mianroodi, et al. “Influence of microstructure and atomic-scale chemistry on the direct reduction of iron ore with hydrogen at 700°C”. In: *Acta Materialia* 212 (2021), p. 116933.

[14] D. Nuber, H. Eichberger, and B. Rollinger. “Circored fine ore direct reduction”. In: *Millen. Steel* 2006 (2006), pp. 37–40.

[15] D. Spreitzer and J. Schenk. “Reduction of iron oxides with hydrogen—a review”. In: *steel research international* 90.10 (2019), p. 1900108.

[16] K. He, Z. Zheng, Z. Chen, H. Chen, and W. Hao. “Kinetics of hydrogen reduction of Brazilian hematite in a micro-fluidized bed”. In: *International Journal of Hydrogen Energy* 46.5 (2021), pp. 4592–4605.

[17] L. Guo, J. Gao, Y. Zhong, and Z. Guo. “Flash suspension reduction of ultra-fine Fe2O3 powders and the kinetic analyzing”. In: *ISIJ International* (2015), ISIJINT–2014.

[18] L. Yi, Z. Huang, and T. Jiang. “Sticking of iron ore pellets during reduction with hydrogen and carbon monoxide mixtures: behavior and mechanism”. In: *Powder Technology* 235 (2013), pp. 1001–1007.

[19] C. Lei, Q. Zhu, and H. Li. “Experimental and theoretical study on the fluidization behaviors of iron powder at high temperature”. In: *Chemical Engineering Science* 118 (2014), pp. 50–59.

[20] J. Li, J. Kong, Q. Zhu, and H. Li. “Efficient synthesis of iron nanoparticles by self-agglomeration in a fluidized bed”. In: *AIChE Journal* 63.2 (2017), pp. 459–468.

[21] S. He, H. Sun, C. Hu, J. Li, Q. Zhu, and H. Li. “Direct reduction of fine iron ore concentrate in a conical fluidized bed”. In: *Powder Technology* 313 (2017), pp. 161–168.

[22] M. Komatina and H. W. Gudenau. “The sticking problem during direct reduction of fine iron ore in the fluidized bed”. In: *Metalurgija* 10 (2004), pp. 309–328.

[23] Y. Zhong, Z. Wang, X. Gong, and Z. Guo. “Sticking behavior caused by sintering in gas fluidisation reduction of haematite”. In: *Ironmaking & Steelmaking* 39.1 (2012), pp. 38–44.

[24] T. Mikami, H. Kamiya, and M. Horio. “The mechanism of defluidization of iron particles in a fluidized bed”. In: *Powder technology* 89.3 (1996), pp. 231–238.

[25] L. Guo, Q. Bao, J. Gao, Q. Zhu, and Z. Guo. “A review on prevention of sticking during fluidized bed reduction of fine iron ore”. In: *ISIJ International* 60 (2020), pp. 1–17.

[26] S. Hayashi and Y. Iguchi. “Factors affecting the sticking of fine iron ores during fluidized bed reduction”. In: *ISIJ international* 32.9 (1992), pp. 962–971.

[27] Y. Zhong, Z. Wang, Z. Guo, and Q. Tang. “Defluidization behavior of iron powders at elevated temperature: Influence of fluidizing gas and particle adhesion”. In: *Powder technology* 230 (2012), pp. 225–231.

[28] M. Gluckman, J. Yerushalmi, and A. Squires. “Defluidization characteristics of sticky or agglomerating beds”. In: *Fluidization technology*. Vol. 2. Hemisphere Washington DC, 1976, pp. 395–422.

[29] X. Liu, X. Zhang, J. Li, Q. Zhu, N. G. Deen, and Y. Tang. “Regeneration of iron fuel in fluidized beds Part I: defluidization experiments and theoretical prediction model”. In: *Powder Technology, (Accepted)* (2023).

[30] C. J. M. Hessels, T. A. M. Homan, N. G. Deen, and Y. Tang. “Reduction kinetics of combusted iron powder using hydrogen”. In: *Powder Technology* (2022), p. 117540.

[31] J. Hancock and J. Sharp. “Method of comparing solid-state kinetic data and its application to the decomposition of kaolinite, brucite, and BaCO3”. In: *Journal of the American Ceramic Society* 55.2 (1972), pp. 74–77.

[32] E. R. Monazam, R. W. Breault, and R. Siriwardane. “Kinetics of hematite to wustite by hydrogen for chemical looping combustion”. In: *Energy & Fuels* 28.8 (2014), pp. 5406–5414.

[33] E. R. Monazam, R. W. Breault, and R. Siriwardane. “Reduction of hematite (Fe2O3) to wüstite (FeO) by carbon monoxide (CO) for chemical looping combustion”. In: *Chemical Engineering Journal* 242 (2014), pp. 204–210.

[34] S. Nasr and K. P. Plucknett. “Kinetics of iron ore reduction by methane for chemical looping combustion”. In: *Energy & fuels* 28.2 (2014), pp. 1387–1395.

[35] A. A. El-Geassy. “Gaseous reduction of Fe2O3 compacts at 600 to 1050°C”. In: *Journal of materials science* 21.11 (1986), pp. 3889–3900.

[36] M. Sastri, R. Viswanath, and B. Viswanathan. “Studies on the reduction of iron oxide with hydrogen”. In: *International Journal of Hydrogen Energy* 7.12 (1982), pp. 951–955.

[37] S. P. Matthew and P. C. Hayes. “Microstructural changes occurring during the gaseous reduction of magnetite”. In: *Metallurgical Transactions B* 21.1 (1990), pp. 153–172.

[38] D. Ning, Y. Shoshin, M. van Stiphout, J. van Oijen, G. Finotello, and P. de Goey. “Temperature and phase transitions of laser-ignited single iron particle”. In: *Combustion and Flame* 236 (2022), p. 111801.

[39] X. Mi, A. Fujinawa, and J. M. Bergthorson. “A quantitative analysis of the ignition characteristics of fine iron particles”. In: *Combustion and Flame* 240 (2022), p. 112011.

[40] Y. Guo, K. Liu, F. Chen, S. Wang, F. Zheng, L. Yang, and Y. Liu. “Effect of basicity on the reduction swelling behavior and mechanism of limestone fluxed iron ore pellets”. In: *Powder Technology* 393 (2021), pp. 291–300.

[41] T. Zhang, C. Lei, and Q. Zhu. “Reduction of fine iron ore via a two-step fluidized bed direct reduction process”. In: *Powder technology* 254 (2014), pp. 1–11.

[42] A. A. El-Geassy, M. I. Nasr, and M. M. Hessien. “Effect of reducing gas on the volume change during reduction of iron oxide compacts”. In: *ISIJ international* 36.6 (1996), pp. 640–649.

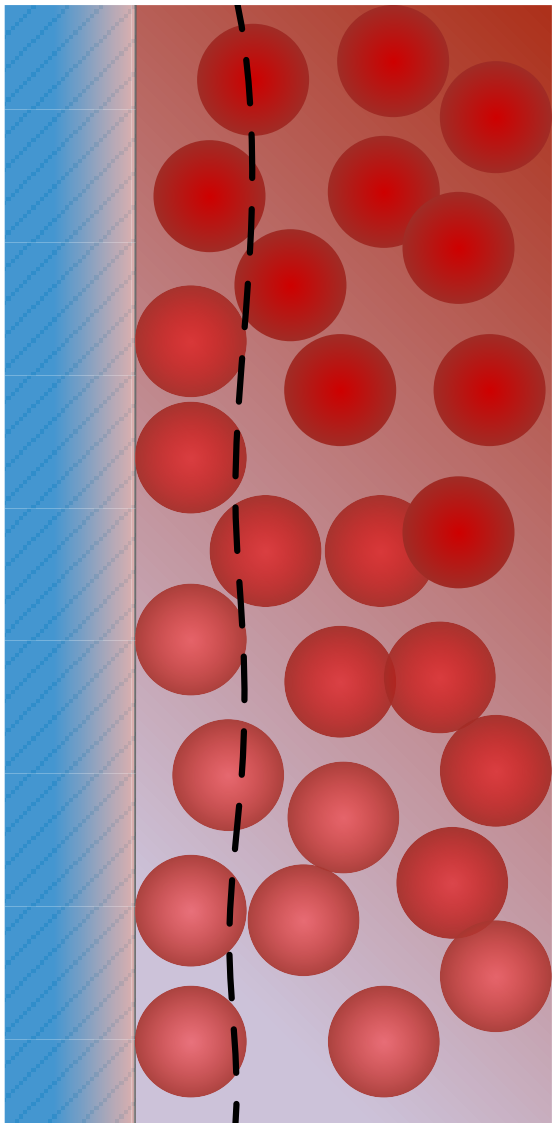

4

SIMULATION ON HEAT TRANSFER

This chapter is based on: X. Liu, N. G. Deen, Y. Tang:
On the treatment of bed-to-wall heat transfer in CFD-DEM simulations of gas-fluidized beds. Chemical Engineering Science, 2021, 236: 116492.

Abstract

Heat exchange through confining walls is an important feature of gas-fluidized beds. However, near the wall, most of the temperature gradient exists in a thin thermal boundary layer, which is typically smaller than the grid size in the computational fluid dynamics method (CFD). This makes it hard to resolve the temperature distribution near the wall in coupled computational fluid dynamics and discrete element method (CFD-DEM). To obtain a better understanding of the heat transfer mechanism near the confining walls in fluidized beds, we adopted two approaches, i.e., by imposing a thermal boundary condition for the gas phase energy equation and by implementing a particle-wall conduction model for the discrete particle phase. Both methods were first explained in detail and then validated by available experimental results. Finally, the two approaches were compared with respect to their performance on the prediction of the overall particle temperature distribution, parameter sensitivity, and mesh resolution.

4.1. Introduction

Gas-fluidized beds are widely employed in a variety of thermochemical processes mainly due to their excellent heat and mass transfer characteristics. In these applications, heat transfer usually plays a critical role when chemical reactions are involved. As such, heat transfer influences the reaction rate as well as the performance of the reactor. Among these applications, many involve heat transfer between the bed and the walls and/or internals, the understanding of which is of great importance to reactor design and dimensioning.

Experimental measurements are limited in understanding the details of heat transfer in bed due to the complex interactions between gas, particles, walls, and immersed tubes. Thus, numerical simulation has become an important tool to model and predict the flow and heat transfer behavior in fluidized beds. In particular, a coupled computational fluid dynamics and discrete element method (CFD-DEM) has been mostly used to study the details of transport phenomena prevailing in fluidized beds on a particle scale [1]. In this method, the gas phase is treated as a continuum by solving the volume-averaged Navier-Stokes equations, while the particles are tracked individually by solving Newton's equations of motion [2]. In recent years, CFD-DEM simulations have been extended to include heat transfer as well [3–7]. Patil et al. [3] studied the mechanisms of heat exchange in a pseudo-2D fluidized bed by comparing CFD-DEM simulations with infrared/visual measurements and pointed out that the convection heat transfer between two phases and the heat loss through the confining walls were both significant. Oschmann and Kruggel-Emden [6] performed CFD-DEM simulations including the particle-wall heat conduction and validated their model for rotating drum and packed bed cases. Immersed tubes have also been considered in the CFD-DEM for the comprehensive study on the heat transfer between tube surface and bed. Hou et al. [8, 9] have conducted simulations to study the effect of particle thermal conductivity, superficial gas velocity, and tube array settings on the heat flux between fluidized bed and tubes. Wahyudi et al. [5] applied 3D CFD-DEM simulations to examine the heat transfer in fluidized beds with an immersed tube. It was pointed out that the maximum heat transfer coefficient was a result of the competition between tube–particle conduction and tube–fluid convection. At low superficial gas velocity the tube–particle conduction was the dominant heat transfer mode, whereas at high gas velocity tube–fluid convection dominated.

In the CFD-DEM, the fluid phase is resolved using a grid size larger than the size of a particle (typically $2-4$ times particle diameter). However, in fluidized beds, due to the vigorous mixing of gas and solids, most of the temperature gradient and heat transfer resistance lies very close to the wall. In other words, the resistance to heat transfer lies within a thin layer, which is approximately one particle diameter. Obviously, the grid size is much larger than the thermal layer thickness. Thus, the thermal layer is unresolved, which does not allow for a straightforward treatment of heat flux through the walls. Instead, additional models/treatments are required to account for the bed-to-wall heat transfer. A variety of methods to describe the bed-to-wall heat transfer have been developed for CFD-DEM simulations [7, 10–13]. There is no consensus on the most appropriate/accurate model. The existing bed-to-wall thermal models in literature can be roughly categorized into two approaches. The first approach describes the heat exchange from the view of the fluid phase by imposing a thermal mixed boundary condition at the solid walls. A common feature of this approach is that a scaling/correction factor is required in order

to obtain a good fit to experimental data. In the work of Lichtenegger et al. [10], a factor ($\Delta x/2\delta_l$) was chosen to scale up the temperature gradient obtained from the CFD grid to achieve the physical result, where Δx is the grid spacing and δ_l is the boundary layer thickness. Similarly, Forgber et al. [11] adjusted the bed-to-wall heat transfer coefficient by accounting for the thermal boundary layer near the wall. In the study of Forgber et al. [11] and Patil et al. [3], the effective gas phase thermal conductivity was used in the thermal boundary condition. However, Li et al. [7] mentioned that the more accurate way of treating the heat loss through the walls was accounting for the solids phase contribution, indicating that the effective bed thermal conductivity models were crucial in the near-wall region. Therefore, a much higher value of the effective thermal conductivity would be obtained compared to that only accounting for the pure gas phase contribution. Previous efforts have been made for studying the effective bed conductivity in fluidized beds based on the two-fluid model (TFM) [14–16]. Within the TFM model, the thermal conductivity of the gas and solids phase are treated with effective thermal conductivity in the energy equation separately. Zehner and Schlünder [17] proposed the effective thermal conductivities for gas and solids phases on the basis of packed beds. Later, this model was used to study the heat transfer in fluidized beds and extended to the heat transfer for the near-wall region [14, 15]. From the approach proposed by Hunt [18], the effective solids phase conductivity should also consider the contribution arising from the streaming of the particles, which was referred to the kinetic conductivity. TFM studies from Schmidt and Renz [19] and Patil et al. [16] investigated the influence of the kinetic contribution on the effective solids phase conductivity, and draw the conclusion that the bed-to-wall heat transfer coefficients were strongly overestimated when accounting for the kinetic contribution to the effective solids phase conductivity. Patil et al. [16] explained the reason might be an over-prediction of the granular temperature at the walls. Since then, there is no solid evidence to explain the fundamental reason for such an over-predicted heat transfer phenomenon, which thus requires further investigation.

The second approach describes the heat exchange from the view of the solids phase, taking into account the detailed heat transfer mechanisms at the particle level. In this case, the entire particle-wall heat transfer includes two mechanisms, i.e., the particle-wall direct conduction and the indirect heat transfer from particles to the walls through a thin gas layer [12, 13]. Regarding the second mechanism, the particle-fluid-wall conduction model has been proposed. The particle-fluid-wall conduction model proposed by Rong and Horio [20] is widely used to account for the heat removal through walls [12, 13, 21–24]. This model assumes that each particle is surrounded by a fluid lens (r_{lens}), and when the wall-particle distance is smaller than the thickness of this fluid layer thickness, such conduction between the particle and the wall through the fluid lens initiates. Additionally, a minimum separation distance is required to prohibit the perfect contact, which would result in an infinite rate of conduction heat flux between the particle and the wall. Morris et al. [23] studied the effect of input parameters on particle-fluid-wall conduction for a static, single-particle system and concluded that the indirect conduction was sensitive to the minimum conduction distance but not to the gas layer lens. Later, Lattanzi and Hrenya [21] carried out CFD-DEM simulation to evaluate these effects for dynamic, multiparticle systems and draw the conclusion that the dynamic system was more sensitive to the gas layer lens. Based on the indirect conduction model, Lattanzi and Hrenya [12] proposed a numerical method for modeling constant heat flux boundary condition in

DEM simulations. Recently, Zhang and Lu [22] extended this numerical technique by considering the gas heat transfer resistance lying in the thin thermal film. It was pointed out that the proposed method predicted more accurate hear transfer coefficients than the previous method obtained by Lattanzi and Hrenya [12]. Additionally, Lu et al. [13] added the particle-fluid-wall conduction model to a coarse grained particle model and validated the method by comparing CFD-DEM results with experimental data. It was found that the proposed coarse grained method accurately simulated the heat transfer in large scale fluidized beds at low computational cost.

Both aforementioned approaches possess uncertainty due to some unknown parameters which can be considered as tuning factors in the model. These parameters are commonly chosen either by fitting parameters or from empirical correlations. However, the choice of these adjustable parameters is usually limited to particular experimental conditions. We have not yet found a constructive guidance on how to determine these parameters, nor how sensitive the model accuracy is to these parameters. In respect to the above considerations, the objective of the current study is to evaluate and compare both approaches for modeling bed-to-wall heat transfer in a fluidized bed using CFD-DEM simulations. The results of the simulations are compared to available experimental data. Additionally, the overall particle temperature distribution, parameter sensitivity, and mesh resolution of both models are investigated. For sake of clarity, we will denote to represent the thermal boundary condition approach by "tBC model" and use "PW model" to represent the particle-wall conduction model. The overall goal of this study is to provide some insights for general thermal CFD-DEM simulations of dense gas-solid flows.

This Chapter is organized as follows: Section 4.2 gives the details of the thermal CFD-DEM method as well as the constitutive equations for the two bed-to-wall heat transfer models. Subsequently, the description of the numerical geometry and parameters are given in Sections 4.3. In Section 4.4, results are presented with respect to the parameter sensitivity, grid dependency, and model performance. Finally, conclusions are given in Section 4.5.

4.2. Numerical model

The CFD-DEM method is implemented within the framework of CFDEMcoupling based on OpenFOAM and LIGGGHTS [25]. Since the current research is mainly focusing on the treatment methods of the bed-to-wall heat transfer, we only give a brief description of the CFD-DEM model here.

4.2.1. CFD-DEM model

In the CFD-DEM method, the gas motion described by the continuity equation and Navier-Stokes equations are expressed as:

$$\frac{\partial\left(\varepsilon_{\mathrm{f}}\rho_{\mathrm{f}}\right)}{\partial t}+\nabla\cdot\left(\varepsilon_{\mathrm{f}}\rho_{\mathrm{f}}\mathbf{u}_{\mathrm{f}}\right)=0 \tag{4.1}$$

$$\frac{\partial\left(\varepsilon_{\mathrm{f}}\rho_{\mathrm{f}}\mathbf{u}_{\mathrm{f}}\right)}{\partial t}+\nabla\cdot\left(\varepsilon_{\mathrm{f}}\rho_{\mathrm{f}}\mathbf{u}_{\mathrm{f}}\mathbf{u}_{\mathrm{f}}\right)=-\varepsilon_{\mathrm{f}}\nabla p_{\mathrm{f}}+\varepsilon_{\mathrm{f}}\nabla\cdot\tau_{\mathrm{f}}-\mathbf{S}+\varepsilon_{\mathrm{f}}\rho_{\mathrm{f}}\mathbf{g} \tag{4.2}$$

where ρ_f, $\mathbf{u}_\mathrm{f}$, and p_f are the density, velocity and pressure of the gas phase, respectively. Note that the gas density is calculated from the equation of state for ideal gas. ε_f is gas phase voidage of current computational cell. τ_f is the viscous stress tensor for the gas phase and for Newtonian fluid it can be evaluated as:

$$\tau_\mathrm{f} = \mu_\mathrm{f}\left[\left(\left(\nabla\mathbf{u}_\mathrm{f}\right)+\left(\nabla\mathbf{u}_\mathrm{f}\right)^\mathrm{T}\right)-\frac{2}{3}\mathbf{I}\left(\nabla\cdot\mathbf{u}_\mathrm{f}\right)\right] \tag{4.3}$$

where μ_f is the gas phase viscosity. $\mathbf{I}$ is a second order metric tensor. The sink term $\mathbf{S}$ accounts for the momentum exchange between particles and fluid:

$$\mathbf{S} = \frac{1}{\Delta\mathrm{V}}\sum_{i=1}^{n}\frac{\mathrm{V}_{p,i}\beta}{1-\varepsilon_\mathrm{f}}\left(\mathbf{u}_\mathrm{f}-\mathbf{v}_\mathrm{p}\right)D\left(\mathbf{r}-\mathbf{r}_i\right) \tag{4.4}$$

where n is the number of particles located in the Eulerian grid with cell volume $\Delta\mathrm{V}$. $\mathrm{V}_{p,i}$ and $\mathbf{v}_\mathrm{p}$ are the particle volume and velocity. β is the gas-particle drag coefficient. In this work, it is evaluated by the correlation proposed by Beetstra et al. [26]. D is the distribution function, which is used to distribute the force acted by the particles on the gas phase to the Eulerian grid. $\mathbf{r}$ and $\mathbf{r}_i$ are the position vector of the staggered velocity cell and the particle center of mass.

The thermal energy equation for the gas phase is given by:

$$C_\mathrm{p,f}\left[\frac{\partial\left(\varepsilon_\mathrm{f}\rho_\mathrm{f}T_\mathrm{f}\right)}{\partial t}+\nabla\cdot\varepsilon_\mathrm{f}\rho_\mathrm{f}\mathbf{u}_\mathrm{f}T_\mathrm{f}\right] = \nabla\cdot\varepsilon_\mathrm{f}k_\mathrm{f}^\mathrm{eff}\nabla T_\mathrm{f}+Q^\mathrm{p-f} \tag{4.5}$$

where $C_\mathrm{p,f}$ is the gas specific heat capacity. T_f is the temperature of the gas phase. $k_\mathrm{f}^\mathrm{eff}$ is the effective thermal conductivity of the gas phase, which can be expressed in terms of the intrinsic fluid thermal conductivity k_f [15] as follows:

$$k_\mathrm{f}^\mathrm{eff} = \frac{1-\sqrt{1-\varepsilon_\mathrm{f}}}{\varepsilon_\mathrm{f}}k_\mathrm{f} \tag{4.6}$$

The heat transfer of the particle to the fluid is the source term, which can be calculated as:

$$Q^\mathrm{p-f} = \sum_i \pi\mathrm{d}_{p,i}^2 h\left(T_{p,i}-T_\mathrm{f}\right)D\left(\mathbf{r}-\mathbf{r}_i\right) \tag{4.7}$$

where $T_{p,i}$ is the temperature of particle i. $\mathrm{d}_{p,i}$ is the diameter of particle i. h is the heat transfer coefficient, which is calculated from Nusselt number (Nu_p) by the empirical correlation given by Gunn [27]:

$$\mathrm{Nu}_\mathrm{p} = \left(7-10\varepsilon_\mathrm{f}+5\varepsilon_\mathrm{f}^2\right)\left(1+0.7\mathrm{Re}_\mathrm{p}^{0.2}\mathrm{Pr}^{0.33}\right)+\left(1.33-2.40\varepsilon_\mathrm{f}+1.20\varepsilon_\mathrm{f}^2\right)\mathrm{Re}_\mathrm{p}^{0.7}\mathrm{Pr}^{0.33} \tag{4.8}$$

and:

$$h = \frac{\mathrm{Nu}_\mathrm{p}k_\mathrm{f}}{\mathrm{d}_\mathrm{p}}, \mathrm{Re}_\mathrm{p} = \frac{\varepsilon_\mathrm{f}\rho_\mathrm{f}\mathrm{d}_\mathrm{p}\left|\mathbf{u}_\mathrm{f}-\mathbf{v}_\mathrm{p}\right|}{\mu_\mathrm{f}} \tag{4.9}$$

The Prandtl number Pr is given by:

$$\mathrm{Pr} = \frac{\mu_\mathrm{f}C_\mathrm{p,f}}{k_\mathrm{f}} \tag{4.10}$$

The DEM model is based on the soft sphere approach which has been implemented in the open source package LIGGGHTS [28]. Newton's 2nd law is used to solve the instantaneous motion of individual particles. The translational and rotational motions of a single particle i are governed by the following equations as:

$$m_i \frac{d\mathbf{v}_i}{dt} = m_i \mathbf{g} - \mathrm{V}_i \nabla p + \mathbf{F}_{\mathrm{d},i} + \mathbf{F}_{\mathrm{c},i} \tag{4.11}$$

$$I_i \frac{d\boldsymbol{\omega}_i}{dt} = \mathbf{T}_i \tag{4.12}$$

where m_i, I_i, $\boldsymbol{\omega}_i$ and $\mathbf{T}_i$ are the mass, the moment of inertia of the particle, the angular velocity and the torque resulting from the collision of the particles, respectively. The terms on the RHS represent the gravity force, the pressure gradient force, the drag force and the contact force. The contact force is approximated by the model as proposed by Cundall and Strack [29].

The heat balance for the internal (thermal) energy of particle i is:

$$m_i C_{p,i} \frac{dT_i}{dt} = \sum_{j \neq i} Q_{ij}^{\mathrm{p-p}} + Q_i^{\mathrm{p-w}} + Q_i^{\mathrm{p-f}} \tag{4.13}$$

The radiation heat transfer from particle to surroundings is not taken into account since the differences between the initial bed temperature and gas temperature are relatively small [30]. Thus, heat transfer of particle i surrounded by fluid and particles/walls includes: particle-gas convection ($Q^{\mathrm{p-f}}$), particle-particle/wall conduction ($Q^{\mathrm{p-p}}$, $Q^{\mathrm{p-w}}$). The conduction mechanisms can be subdivided into two categories: (1) direct conduction between two contact solids, i.e., particle-particle (Q^{pp}), particle-wall (Q^{pw}). (2) indirect conduction through a thin fluid layer between two particles, i.e., particle-fluid-particle (Q^{pfp}), particle-fluid-wall (Q^{pfw}). Note that the expressions for Q^{pp} and Q^{pfp} are very similar to those for Q^{pw} and Q^{pfw}, which will be introduced in Section 4.2.2. For simplification, we will not give these details because of our focus on bed-to-wall heat transfer.

4.2.2. Constitutive equations for bed-to-wall heat transfer

Thermal boundary condition approach

In the near-wall region of a fluidized bed, the particulate phase heat transfer becomes significant due to the frequent particle-wall collisions. The temperature gradient of the bed exists in a very thin thermal boundary layer of the order of one to two particle diameter [14, 19], see Figure 4.1. From a fluid point of view, the bed-to-wall heat transfer can be described by imposing a thermal boundary condition at the walls. Such boundary condition can be expressed as:

$$-k_b \frac{dT_{\mathrm{g}}}{dx/2} = h_{\mathrm{w}}(T_{\mathrm{ext}} - T_{\mathrm{g}}) \tag{4.14}$$

where k_b is the mixture conductivity or "effective bed conductivity". T_{ext} is the external temperature or the temperature deep in the wall. T_{g} is the gas temperature. h_{w} is the bed-to-wall heat transfer coefficient which is determined by the thickness of the thermal

boundary layer. By imposing this boundary condition, all the heat transfer mechanisms in the near-wall region are lumped together, including particle-wall conduction ($Q^{\mathrm{p-w}}$). Therefore, it is necessary to point out that the particle-wall (Q^{pw}) and particle-fluid-wall (Q^{pfw}) conduction are excluded from eq. (4.13) when imposing this mixed boundary condition. The heat transfer coefficient h_{w} is hard to determine either by experiments or an unresolved numerical approach. Hence, choosing it as a fitting parameter is logical when predicting the exact amount of heat loss from the bed. The calculation method for the effective bed thermal conductivities (k_b) and the heat transfer coefficient (h_{w}) are discussed in the following subsections.

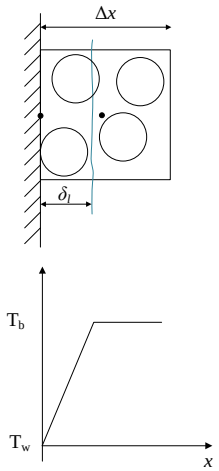

Figure 4.1: A schematic view diagram showing the bed temperature gradient in the near-wall region.

The effective thermal conductivities of the gas and solids phase

In the thermal boundary layer near the wall, both gas-wall and particle-wall conduction contribute to the total heat exchange at the walls. Fourier's law of heat conduction can be used to represent the conduction heat transport for both phases:

$$q_{\mathrm{f}} = -\varepsilon_{\mathrm{f}} k_{\mathrm{f}}^{\mathrm{eff}} \nabla T_{\mathrm{f}} \tag{4.15}$$

$$q_{\mathrm{s}} = -\left(1-\varepsilon_{\mathrm{f}}\right) k_{\mathrm{s}}^{\mathrm{eff}} \nabla T_{\mathrm{s}} \tag{4.16}$$

$$q_{\mathrm{total}} = q_{\mathrm{f}} + q_{\mathrm{s}} = -\left[\varepsilon_{\mathrm{f}} k_{\mathrm{f}}^{\mathrm{eff}} \nabla T_{\mathrm{f}} + \left(1-\varepsilon_{\mathrm{f}}\right) k_{\mathrm{s}}^{\mathrm{eff}} \nabla T_{\mathrm{s}}\right] \tag{4.17}$$

In case of thermodynamic equilibrium ($T_{\mathrm{f}} = T_{\mathrm{s}} = T$)

$$q_{\mathrm{total}} = -k_b \nabla T \tag{4.18}$$

where k_b is the "mixture conductivity" or effective bed conductivity. Combining eqs. (4.17) and (4.18), we can obtain:

$$k_{\mathrm{b}} = \varepsilon_{\mathrm{f}} k_{\mathrm{f}}^{\mathrm{eff}} + \left(1-\varepsilon_{\mathrm{f}}\right) k_{\mathrm{s}}^{\mathrm{eff}} \tag{4.19}$$

As shown in this expression, the estimation of both effective gas thermal conductivity and effective solids thermal conductivity is the key to determine the effective bed conductivity

in the thermal boundary layer. Zehner and Schlünder [17] proposed the effective thermal conductivities for gas and solids phases on the basis of packed beds, which has been used in many studies later [14, 16, 31–33]. In this model, the effective bed conductivity is a function of bulk voidage, pure thermal conductivity of the gas and solids phase, and the particle geometry. Later, this model was used to study the heat transfer in fluidized beds and extended to the heat transfer for the near-wall region [14, 15]. According to the effective bed conductivity model proposed by Zehner and Schlünder [17], the phase thermal conductivities are then obtained as:

$$k_{\mathrm{f}}^{\mathrm{eff}} = \frac{\left(1-\sqrt{1-\varepsilon_{\mathrm{f}}}\right)}{\varepsilon_{\mathrm{f}}} k_{\mathrm{f}} \tag{4.20}$$

$$k_{\mathrm{s}}^{\mathrm{eff}} = \frac{\{\omega A + (1-\omega)\,\Gamma\}}{\sqrt{1-\varepsilon_{\mathrm{f}}}} k_{\mathrm{f}} \tag{4.21}$$

with:

$$\Gamma = \frac{2}{1-\frac{B}{A}} \left\{ \frac{(A-1)}{\left(1-\frac{B}{A}\right)^2} \frac{B}{A} \ln\left(\frac{A}{B}\right) - \frac{B-1}{\left(1-\frac{B}{A}\right)} - \frac{1}{2}(B+1) \right\} \tag{4.22}$$

For spherical particles:

$$A = \frac{k_{\mathrm{s}}}{k_{\mathrm{f}}}, B = 1.25\left(\frac{1-\varepsilon_{\mathrm{f}}}{\varepsilon_{\mathrm{f}}}\right)^{10/9}, \omega = 7.26\times10^{-3} \tag{4.23}$$

Additionally, Natarajan and Hunt [34] proposed that the effective solids phase conductivity in eq. (4.21) needs to be extended to include kinetic conductivity (k_{s}^{kin}) due to the streaming of the particles in fluidized beds. Thus the total effective solids conductivity would be the sum of eq. (4.21) (referred as k_{s}^{mol}) and k_{s}^{kin}. Base on the expression for the kinetic conductivity derived by Hunt [18] and the self-diffusion theory given by Chapmann and Cowling [35], this kinetic conductivity can be expressed as:

$$k_{\mathrm{s}}^{kin} = \rho_{\mathrm{s}} C_{p,s} d_{\mathrm{p}} \sqrt{\Theta_s} \frac{\pi^{1/2}}{16} \tag{4.24}$$

where ρ_{s}, $C_{p,s}$, and Θ_s are the solids density, solids specific heat capacity, and the particle granular temperature, respectively.

Particle-wall conduction model

As said, the thermal boundary condition approach lumps all the heat transfer mechanisms. In contrast, the second approach decouples different contributions of the total bed-to-wall heat transfer, meaning that the gas-wall and particle-wall heat transfer are treated separately. The particle-wall conduction is accounted for in eq. (4.13) of individual particles, which includes both direct (Q^{pw}) and indirect (Q^{pfw}) conduction. In this paper the particle-wall direct conduction is implemented as Batchelor and O'brien model [36] :

$$Q_i^{\mathrm{pw}} = \frac{4 k_{p,i} k_{\mathrm{w}}}{k_{p,i} + k_{\mathrm{w}}} R_c \left(T_{\mathrm{w}} - T_{p,i}\right) \tag{4.25}$$

where $k_{p,i}$ and k_{w} are the thermal conductivity of particle i and the wall, respectively. R_c is the contact radius which relates to the overlap between the particle and the wall in the collision model, which can be calculated by:

$$R_{\mathrm{c}} = \sqrt{\mathrm{r_p^2} - (\mathrm{r_p} - \delta)^2} \tag{4.26}$$

where δ is the dynamic overlap between the particle and the wall. In the DEM model, usually a smaller Young's modulus is adopted to allow a larger time step and reduce the computational cost. As a consequence, a larger overlap displacement and larger contact radius are obtained, which results in overprediction of the conductive heat transfer between the particle and the wall. In order to compensate such overestimation, a correction factor c is adopted to correct the dynamic overlap displacement by $\mathrm{c}\delta$. Therefore, the corrected overlap is determined as:

$$R_c^{'} = \sqrt{\mathrm{r_p^2} - (\mathrm{r_p} - \mathrm{c}\delta)^2} \tag{4.27}$$

$$\mathrm{c} = \left(\frac{\mathrm{Y^*}}{\mathrm{Y_0^*}}\right)^{\mathrm{n}} \tag{4.28}$$

with:

$$\frac{1}{\mathrm{Y^*}} = \left(\frac{1-\nu_i^2}{\mathrm{Y}_i}\right) + \left(\frac{1-\nu_{\mathrm{w}}^2}{\mathrm{Y_w}}\right) \tag{4.29}$$

$$\frac{1}{\mathrm{Y_0^*}} = \left(\frac{1-\nu_i^2}{\mathrm{Y}_{0,i}}\right) + \left(\frac{1-\nu_{\mathrm{w}}^2}{\mathrm{Y}_{0,\mathrm{w}}}\right) \tag{4.30}$$

where Y, $\mathrm{Y_0}$, and ν are the Young's modulus applied in DEM, original particle Young's modulus, and the Poisson's ratio. The subscript i and w refer to particle i and the wall. The exponent n depends on the contact model, which is chosen 2/3 when applied a Hertz contact force model and 1 for Hook contact model.

Regarding particle-fluid-wall conduction, the model proposed by Rong and Horio [20] is used, as sketched in Figure 4.2. From case 1 to case 5, the particle is getting closer to the wall. In this model, each particle is surrounded by a static fluid layer which we will refer to as lens ($\mathrm{r_{lens}}$), and the thickness of the lens is smaller than the particle radius $\left(\mathrm{r_{lens}} - \mathrm{r_p} < \mathrm{r_p}\right)$. We assume that the temperature is uniform inside the particle. When the particle-wall distance is smaller than the fluid layer thickness (after case 1), a conduction heat flux through the fluid layer is calculated by:

$$Q_i^{\mathrm{pfw}} = \int_{r_{in}}^{r_{out}} \frac{2\pi k_{\mathrm{f}} r}{\mathrm{Max}(l, \mathrm{s})} \left(T_{\mathrm{w}} - T_{p,i}\right) dr \tag{4.31}$$

where k_{f} is the gas thermal conductivity. T_{w} and $T_{p,i}$ are the temperatures for the wall and particle i. l represents the particle skin -wall conduction distance. r_{in} and r_{out} are the lower and upper integration bound.

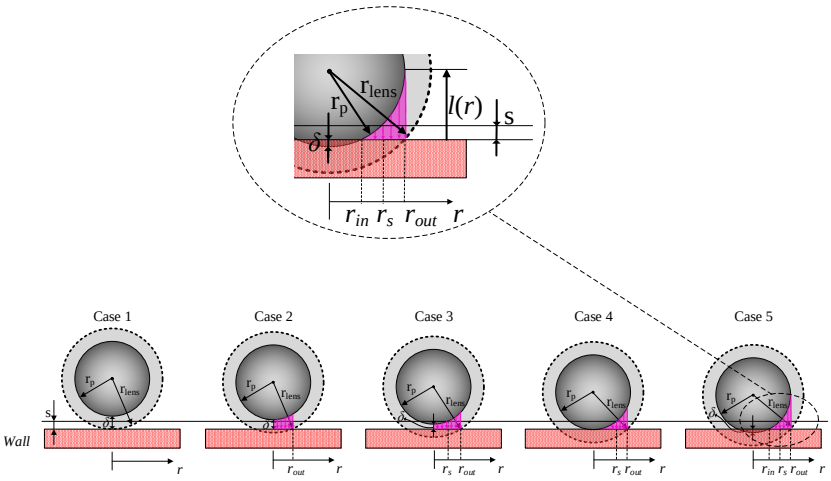

Figure 4.2: Illustration of particle-fluid-wall indirect heat transfer model. From case 1 to case 5, the distance between the particle surface to the wall surface is getting smaller. In case 1, the gas layer surface just touches the wall, so the particle-fluid-wall heat flux is 0; in case 2, the wall surface is overlapping with the gas layer and the distance between the particle surface and the wall surface is larger than s; in case 3, the bottom of the particle surface is inside the minimum conduction region but not in contact with the wall; in case 4, the bottom of the particle surface just touches the wall; in case 5, the particle is in contact with the wall. [20]

A minimum conduction distance (s) is introduced in order to avoid the appearance of the singularity in eq. (4.31) when the conduction distance l approaches to zero. From the perspective of physical explanation, the presence of surface asperities leads to a physical finite separation distance for particle-wall collision. For this reason, a minimum conduction distance can be employed based on the surface roughness of the solids body. Correspondingly, an extra heat flux due to the effect from the confining walls is applied for particles when the gas layer thickness is overlapping with the wall surface. eq. (4.31) is calculated through integration by parts based on different scenarios:

$$Q_i^{\mathrm{pfw}} = \begin{cases} 2\pi k_{\mathrm{f}}\left(T_{\mathrm{w}} - T_{p,i}\right)\int_0^{r_{out}} \frac{r}{l}\,dr & s \le \delta \le r_{\mathrm{lens}} - r_{\mathrm{p}} \quad \text{case 2} \\ 2\pi k_{\mathrm{f}}\left(T_{\mathrm{w}} - T_{p,i}\right)\int_0^{r_s} \frac{r}{s}\,dr + 2\pi k_{\mathrm{f}}\left(T_{\mathrm{w}} - T_{p,i}\right)\int_{r_{in}}^{r_{out}} \frac{r}{l}\,dr & 0 \le \delta < s \quad \text{case 3 \& 4} \\ 2\pi k_{\mathrm{f}}\left(T_{\mathrm{w}} - T_{p,i}\right)\int_{r_{in}}^{r_s} \frac{r}{s}\,dr + 2\pi k_{\mathrm{f}}\left(T_{\mathrm{w}} - T_{p,i}\right)\int_{r_s}^{r_{out}} \frac{r}{l}\,dr & \delta < 0 \quad \text{case 5} \end{cases} \tag{4.32}$$

with:

$$r_{in} = \sqrt{\mathrm{r_p^2} - \left(\mathrm{r_p} + \delta\right)^2} \tag{4.33}$$

$$r_s = \sqrt{\mathrm{r_p^2} - \left(\mathrm{r_p} - (s - \delta)\right)^2} \tag{4.34}$$

$$r_{out} = \sqrt{\mathrm{r_{lens}^2} - \left(\mathrm{r_p} + \delta\right)^2} \tag{4.35}$$

$$l = \left(\mathrm{r_p} + \delta\right) - \sqrt{\mathrm{r_p^2} - r^2} \tag{4.36}$$

Note that in case 5 the dynamic overlap from the collision model is corrected in the same way as in the above-mentioned particle-wall direct conduction model, i.e., using the thermal overlap ($c\delta$) instead of the dynamic overlap (δ) in eqs. (4.33) to (4.36). As can be seen from eq. (4.32), there are only two adjustable parameters, i.e., $\mathrm{r_{lens}}$ and s. But setting the values of these two parameters is not straightforward. As said earlier, the minimum conduction distance (s) is a cut-off distance, which can be related to the physical roughness of the solid surface. Whereas, $\mathrm{r_{lens}}$ is determined by estimation of the thermal boundary layer thickness. Xavier and Davidson [37] experimentally studied the surface-to-bed heat transfer and draw the conclusion that the gas film thickness was $\delta_{\mathrm{lens}} \approx 0.4\mathrm{r_p}$ for horizontal wall, whereas $\delta_{\mathrm{lens}} \approx 0.2\mathrm{r_p}$ for the vertical surfaces. In other works, the lens thickness was typically chosen $0.4\mathrm{r_p}$ [12, 23]. Morris et al. [23] conducted a static, single-particle system to study the sensitivity of indirect conduction to its input parameters, and it was found that increasing the gas film layer from $0.2\mathrm{r_p}$ to $0.41\mathrm{r_p}$ did not dramatically increase the overall heat transfer since most of the conduction heat transfer occurred in a small separation distance.

For completion, the gas-wall heat transfer should also be taken into account. This can be modeled by imposing a similar boundary condition as eq. (4.14), but with use of effective gas thermal conductivity and a gas-wall convective heat transfer coefficient. However, we do not include this for the (PW model) simulations of this work due to the following reasons: 1) In dense gas-fluidized beds, most of the bed-to-wall heat transfer is from contribution of solids phase [38]. The heat transfer coefficient at wall in the freeboard is more than two orders of magnitude smaller than that in the particle bed [14]; 2) The accurate value of the convective heat transfer coefficient is difficult to determine. In case of systems where the first reason is violated, i.e., the gas contribution is comparable to solids contribution to the overall bed-to-wall heat transfer, the above-mentioned boundary condition needs to be included.

4.3. Simulation setup

We set up simulations of a pseudo-2D fluidized bed (see Figure 4.3) as similar to the experiments done by Patil et al. [3]. In the fluidized bed, glass beads of initial temperature $T_{\mathrm{p}} = 363.15$ K are charged into the bed by gravity, and then they are fluidized with cold nitrogen gas with $T_{\mathrm{f}} = 273.15$ K through the bottom plane. The experimental setup has a small circular nozzle with a diameter of 1.3 cm at the bottom, where no gas enters during the experiments. In order to mimic this nozzle area of the setup, in the simulations a no-flow boundary condition is set for 5 × 4 grid cells which is 1.14 cm × 1 cm in size. The same treatment was employed in Patil et al. [3]. In the CFD-DEM model, the bed is divided into 35 × 6 × 110 grid cells in the x-, y-, and z- directions. The physical properties of the particle and the fluid along with the numerical settings are listed in Table 4.1. These correspond to the work by Lichtenegger et al. [10] and Deen et al. [39]. The mechanical and thermal properties of the particles and the walls which can be used for correcting the contact overlap displacement are listed in Table 4.2. Each simulation case is conducted for a total time of 15 s, and the data of the last 5 s are used to analyze the time-averaged variables (i.e. solids volumetric flux).

Table 4.1: Physical properties and settings used in the simulations.

Properties	Value
Particle	
Diameter d_p	0.001 m
Density ρ_p	2500 kg/m^3
Heat capacity $C_{p,p}$	840 J/(kg·K)
Thermal conductivity k_p	1.4 W/(m·K)
Normal spring stiffness k_n	7000 N/m
Tangential spring stiffness k_t	2250 N/m
Normal damping coefficient γ_n	0.00131 (N·s)/m
Tangential damping coefficient γ_t	0.0137 (N·s)/m
Coefficient of friction μ	0.1
Coefficient of rolling friction μ_r	0.125
Fluid	
Heat capacity $C_{p,f}$	1010 J/(kg·K)
Thermal conductivity k_f	0.026 W/(m·K)
Viscosity μ_f	2.0×10^{-5} kg/(m·s)
Density ρ_f	$p_f M / R T_f$
Simulation settings	
Bed mass m_b	75 g
Fluid inlet velocity u_f	1.33 m/s
CFD time step Δt_{CFD}	1.0×10^{-5} s
DEM time step Δt_{DEM}	1.0×10^{-6} s

Table 4.2: Mechanical and thermal properties of the particles and the walls used in the simulation.

Properties	Glass	Aluminum	Sapphire glass
Young's modulus Y (MPa)	5	5	5
Original Young's modulus Y_0 (GPa)	60	69	30
Poisson's ratio ν (-)	0.22	0.34	0.25
Thermal conductivity k (W/(m·K))	1.4	238	30

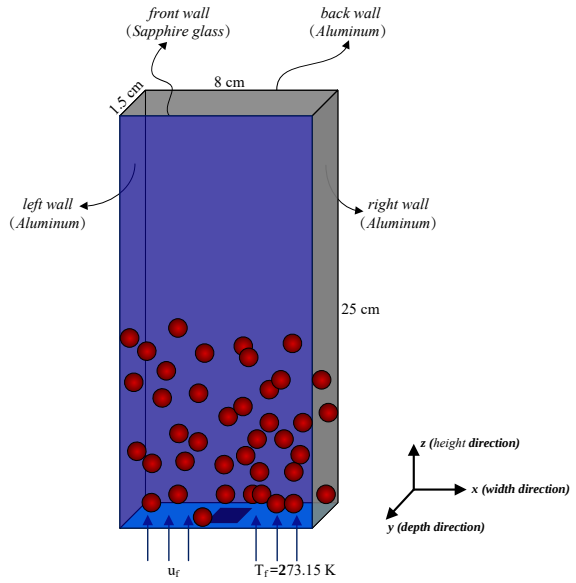

Figure 4.3: Experimental setup of Patil et al. [3] as adapted to CFD-DEM simulation.

4.4. Results and discussions

In this section, we discuss simulations performed using either the thermal boundary condition method or the particle-wall conduction model. Through a detailed discussion of the parameter sensitivity as well as grid dependency, we compare and evaluate these two approaches. The results are shown in the following subsections. Note that the average temperature of all particles in the bed (mean particle temperature) is chosen as an important analyzing result because it represents the overall heat transfer behavior of the studied fluidized bed system, which is also measured from experiments. In Appendix B, we also provide the results demonstrating the performance of these two approaches on predicting near-wall particle temperature distribution.

4.4.1. Thermal boundary condition approach

Overall particle temperature distribution

The particle temperature distribution based on the thermal boundary condition approach is shown in Figure 4.4. It shows a series of simulation snapshots of CFD-DEM particle temperature distribution predicted at several instances (0.5 s, 1 s, 3 s, 9 s, and 15 s). In this case, the bed-to-wall heat transfer coefficient is chosen as 350 [W/(m$^2 \cdot$K)] and the effective bed conductivity is taking the contribution of the solids kinetic conductivity into account. As shown in Figure 4.4, the particulate flow pattern and temperature distribution are transient. More specifically, particles located at the bottom of the bed are cooled down first, and then they are flowing upwards due to the drag. Because of the high particle movement and large gas-particle contact area, the whole bed is cooling down relatively fast.

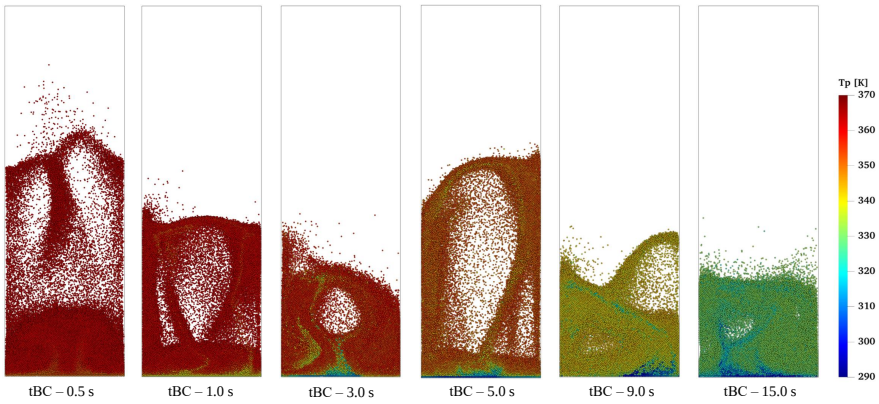

Figure 4.4: Snapshots showing the cooling process of an initially hot fluidized bed by cold gas introduced from the bottom plane using the thermal boundary condition approach.

Sensitivity analysis of k_b

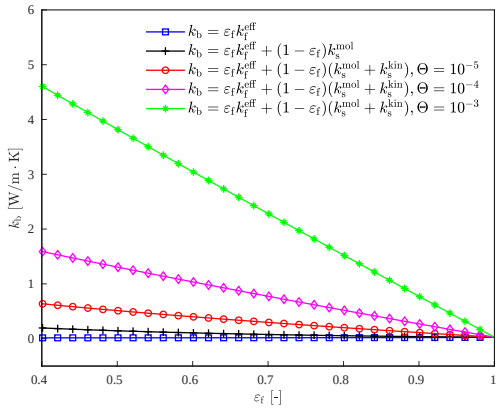

Figure 4.5: Comparison of the effective bed conductivity when considering the solids kinetic contribution, solids molecular contribution, and gas phase as a function of the gas phase void fraction.

As shown in eq. (4.14) for the mixed thermal boundary condition, k_b is a model parameter. In literature, there exist different definitions of k_b taking into account either solely the gas contribution or together with the solids contribution. Figure 4.5 compares the different treatments of k_b using the expression introduced in Section 4.2.2. It is clear that for all treatments, the effective bed conductivity decrease with an increase in the gas phase void fraction, particularly when considering the solids kinetic contribution. Additionally, it can also be seen that the solids phase contribution to the effective bed thermal conductivity is significantly larger than the contribution from the gas phase. For a granular temperature higher than 10^{-4} m^2/s^2, the solids kinetic contribution dominates in almost the entire

range of the gas phase void fraction. Thus, in the near-wall region, the contribution of the solids phase to the effective bed conductivity is relatively important.

Depending on the number of heat transfer mechanisms included, the overall heat transfer in bed is predicted with varying deviations, as shown in Figure 4.6. Note that when considering the contribution of solids kinetic conductivity, we calculate the granular temperature based on the particle velocity fluctuation in each Eulerian grid, which is defined as:

$$\Theta_s = \frac{1}{3} \sum_{k=x,y,z} \left[\frac{1}{n_\mathrm{p}} \sum_{i=1}^{n_\mathrm{p}} \left(v_{k,i} - \bar{v}_k \right)^2 \right] \tag{4.37}$$

with:

$$\bar{v}_k = \frac{1}{n_\mathrm{p}} \sum_{i=1}^{n_\mathrm{p}} v_{k,i} \tag{4.38}$$

where n_p is the number of particles in the Eulerian grid.

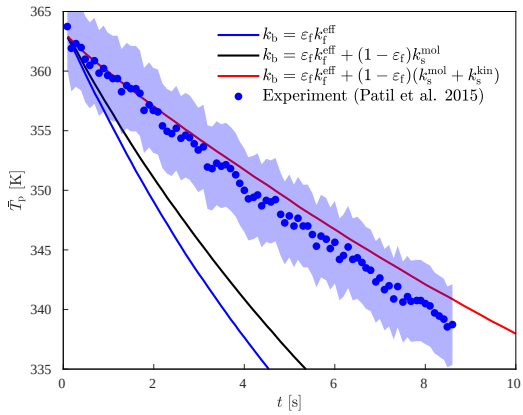

Figure 4.6: Results of the mean particle temperature evolution for considering different contributions of the bed thermal conductivity with applying a heat transfer coefficient of 350 [W/(m^2 · K)]. The granular temperature used in the k_s^{kin} is calculated based on the particle velocity fluctuation in each Eulerian grid. The blue shadow region indicates the ±99% confidence interval.

The blue shadow region in the figure represents the ±99% confidence interval of the experimental data. It is obviously observed that only considering the contribution of the gas phase or together with the contribution of solids molecular conductivity in the boundary condition results in a higher cooling rate of the averaged bed temperature. As shown in Figure 4.5, the contribution of solids kinetic conductivity to the effective conductivity is significantly larger than the other two (gas conductivity and solids molecular conductivity). Without taking it into account leads to a significantly higher cooling rate of the bed temperature. Thus, the only right way to determine k_b is to combine all the contributions including effective gas conductivity, solids molecular conductivity, and solids kinetic conductivity. We notice that there is still controversy about the methods for the estimation of the effective thermal conductivity, particularly within the TFM model [16]. In the TFM

model, the thermal conductivity of the gas and solids phase are treated with an effective thermal conductivity in the energy equation separately, and the granular temperature is solved as a transport equation. Given the complex boundary condition, there might be significant uncertainties in the calculated granular temperature and hence in the kinetic contribution. However, within the DEM method, the granular temperature can be directly obtained based on the individual particle motion in each Eulerian grid cell, resulting in a better prediction of the kinetic solids conductivity.

Sensitivity analysis of h_w

The heat transfer coefficient can first be estimated by the bed-to-wall heat transfer equation reported in Kunii and Levenspiel [40], which was derived as the wall to emulsion phase heat transfer. In the near-wall region of a fluidized bed, h_w was estimated in the range of $250-350$ [W/(m$^2\cdot$K)]. Figure 4.7 shows the results of the mean particle temperature evolution using different values of the bed-to-wall heat transfer coefficient with considering the contribution of the kinetic conductivity to the effective solids conductivity. It can be seen that when the bed-to-wall heat transfer coefficient is in the range of $250-350$ [W/(m$^2\cdot$K)], the simulation results match well with the experimental data with the deviation in an acceptable range since almost all the simulation results are located in the ±99% confidence interval. Moreover, the effect of the heat transfer coefficient on the bed temperature evaluation becomes smaller with an increase of the heat transfer coefficient.

Although the heat removal through the walls from the bed is predicted well in this case, the required parameters h_w is hard to tell with confidence since it is directly linked to the thickness of the thermal boundary layer as well as the specific experimental conditions. More accurate determination of this heat transfer coefficient requires future studies either by advanced experimental measurement or from more detailed simulations, such as fully resolved simulations, which can resolve the thermal layer.

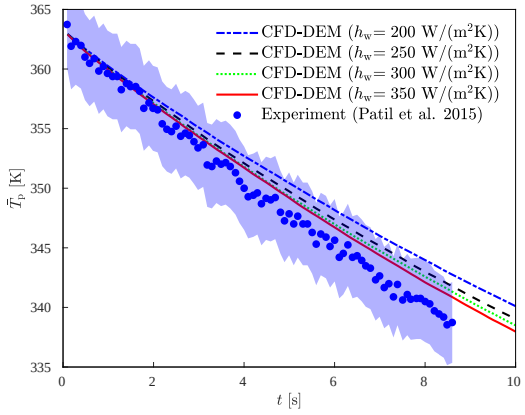

Figure 4.7: Results of the mean particle temperature evolution for different values of the heat transfer coefficient from the wall to bed with applying an effective bed conductivity of $k_b = \varepsilon_f k_f^{\text{eff}} + (1-\varepsilon_f)(k_s^{mol} + k_s^{kin})$). The blue shadow region indicates the ±99% confidence interval.

Sensitivity study of grid size

Last, we investigate the influence of grid size (dx as in eq. (4.14)) on the performance of the thermal boundary model. Simulations with only varying the grid size (see in Table 4.3) are performed with $k_b = \varepsilon_f k_f^{eff} + (1-\varepsilon_f)(k_s^{mol} + k_s^{kin})$ and $h_w = 350$ [W/(m$^2 \cdot$K)], which are the optimal choices from the above study.

Table 4.3: Specifications of the numerical CFD grids used in mesh independent analysis.

case	cell number ($x \times y \times z$) [-]	total cell number [-]	grid size ($\Delta x, \Delta y, \Delta z$) [mm]
Grid-1	$22 \times 4 \times 69$	6072	$3.64 \times 3.75 \times 3.62$
Grid-2	$26 \times 5 \times 81$	10530	$3.08 \times 3 \times 3.09$
Grid-3	$30 \times 6 \times 94$	16920	$2.67 \times 2.50 \times 2.66$
Grid-4	$35 \times 6 \times 110$	23100	$2.29 \times 2.50 \times 2.27$
Grid-5	$40 \times 7 \times 120$	33600	$2 \times 2.14 \times 2.08$

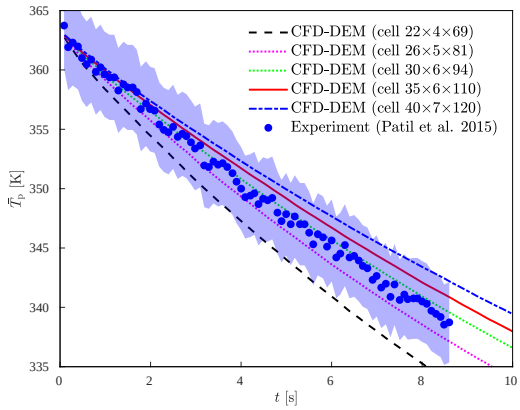

Figure 4.8: Results of the mean particle temperature evolution from simulations with the thermal boundary condition approach using different grid sizes. The blue shadow region presented indicates the ±99% confidence interval.

Figure 4.8 shows the evolution of mean particle temperature resulted from these simulations using five different grid sizes. Clearly, we can see that the grid size has a strong influence on the predicted bed temperature. With refining the grid, the bed particles are cooled slower. However, only from this observation here, it is not straightforward to tell that the influence of the grid size on the bed temperature is through the thermal boundary model, because we know that the grid resolution also influences the hydrodynamics of the bed. Therefore, in Figure 4.9 we examine the time-averaged solids volumetric flux from these simulations. Interestingly, no obvious trend can be observed for the solids volumetric flux from this figure as what is shown to the bed temperature in Figure 4.8. Simulations with grids 3 – 5 all result in a good agreement with the experimental data of

the solids volumetric flux. This is also expected since the grid size in these cases lies in the range of 2 – 3 times particle size, which is the rule of thumb for CFD-DEM simulations. Thus, we can conclude that the slight effect of grid resolution on hydrodynamics can be safely excluded from consideration. In other words, we can confirm that the effect of grid size observed on the bed heat transfer behavior in Figure 4.8 is due to its role in the thermal boundary condition. This reveals that when this thermal boundary model is used, care needs to be taken on the choice of grid size.

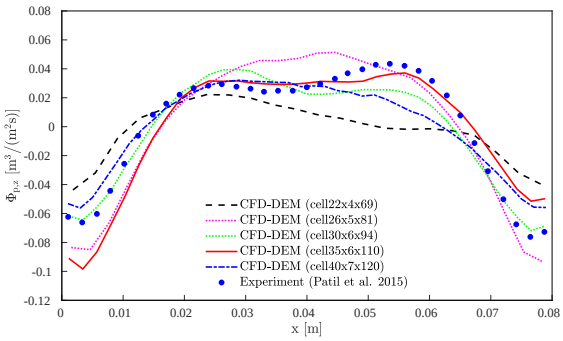

Figure 4.9: Plots of the solids volumetric flux at height z = 2.3 cm from simulations with the thermal boundary condition approach using different grid sizes.

4.4.2. Particle-wall conduction model

In the description of the particle-fluid-wall direct conduction model, two input parameters are required, i.e., the lens thickness (r_{lens}) and the minimum conduction distance (s). In this section, the sensitivity of these two input parameters is discussed by testing them in the above-mentioned pseudo-2D fluidized bed simulation. Detailed verification of the particle-wall direct and particle-fluid-wall indirect conduction models are given in Appendix B.

Overall particle temperature distribution

Figure 4.10 shows the visualization results of the instantaneous particle temperature distribution based on the particle-wall conduction model. In this case, r_{lens} and s are chosen as $1.2r_p$ and 1e-6 m separately. As shown in Figure 4.10, the entire bed is cooling down relatively fast due to the excellent contact between the gas and the particle phase. Reasonable similarity of the flow pattern and temperature distribution features for the thermal boundary condition approach (Figure 4.4) and particle-wall conduction model are observed, demonstrating the capability of both approaches in dealing with the entire heat removal from the bed.

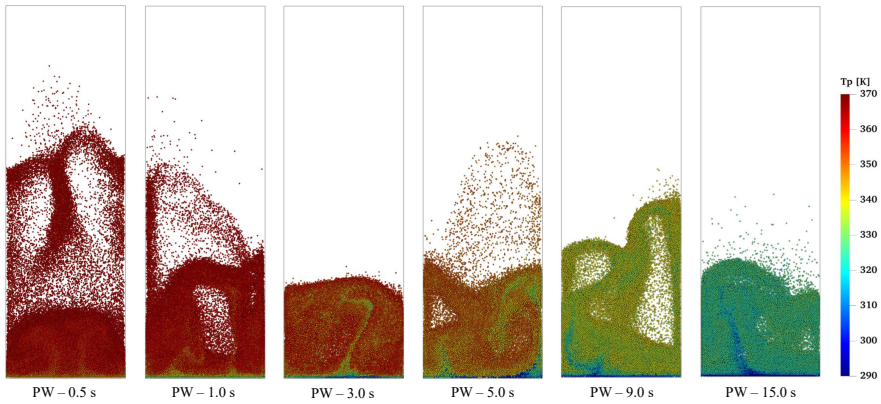

Figure 4.10: Snapshots showing the cooling process of an initially hot fluidized bed by cold gas introduced from the bottom plane using the particle-wall conduction model.

Sensitivity analysis of s

As explained earlier in Section 4.2.2, the minimum conduction distance (s) is introduced with the purpose of avoiding a singularity in eq. (4.31). The surface roughness of the particles is a good estimation of s. In the studied experiments, the particles are relatively smooth glass beads with a size of 1mm. Therefore, the value of s can be taken in the order of microns or smaller. Figure 4.11 shows the mean particle temperature evolution obtained from simulations with the PW model using three different values of s (1 micron, 0.1 micron, 0.01 micron). As can be seen from this figure, the difference in the resulted mean particle temperature in the bed is almost negligible, even though the chosen values of s cover 2 orders of magnitude.

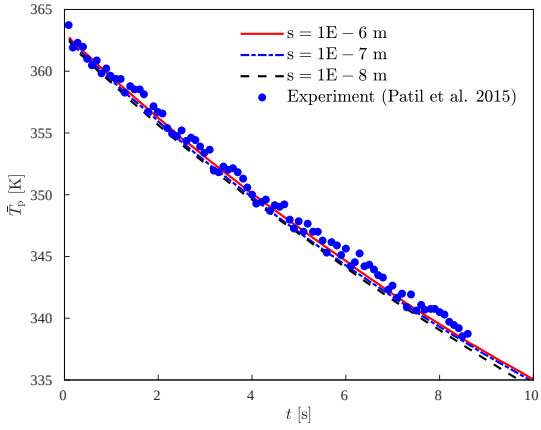

Figure 4.11: Parameter sensitivity study of s for the pseudo-2D fluidized bed simulation using $r_{lens} = 1.2r_p$.

This observation can be somehow understood from Figure 4.2 and eq. (4.31). The

influence of s in the PW model is a space integration, which only affects those particles in contact with the wall or with a particle-wall distance smaller than s. Since in DEM, we solve the contact behavior within the contact time which is very short for rigid particles, in general the effect of the time integrated s will not be significant. Therefore, we conclude that although there is uncertainty of the value of s, the overall performance of the PW model in predicting the particle-wall/particle conduction is almost insensitive to s.

Sensitivity analysis of r_{lens}

As another adjustable parameter, r_{lens} represents the thickness of the gas layer surrounding to the surface of the particle. Practically, the thickness of this thermal layer depends on the thermal condition around the particle, thus it is difficult to provide a priori. By empirical experience, r_{lens} ranges from 20% to 40% of the particle radius [23, 37]. Thus, simulations are performed with the PW model using three different values of r_{lens} (= $1.2r_p$, $1.3r_p$, $1.4r_p$) with s = 1e-6 m. Figure 4.12 shows the results of mean particle temperature evolution from these three cases together with experimental data. First of all, all the cases provide a good agreement with experimental results. Secondly, we do observe a slight influence of r_{lens}, for instance, increasing from $1.2r_p$ to $1.3r_p$. However, from $1.3r_p$ to $1.4r_p$, the influence of r_{lens} dramatically decreases. This indicates that up to $r_{lens} = 1.4r_p$ the results get converged and are not sensitive to the choice of r_{lens} anymore. Overall, when a reasonable range of thermal boundary layer thickness is estimated (see e.g. (Deen et al. [41])), the performance of the PW model for predicting the bed heat transfer is reliable and robust.

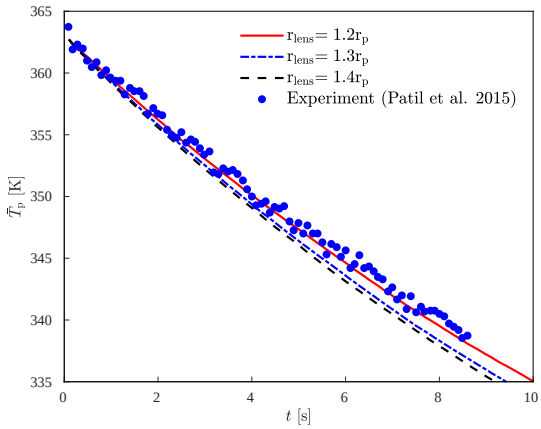

Figure 4.12: Parameter sensitivity study of r_{lens} for the pseudo-2D fluidized bed simulation using s=1e-6 m.

4.5. Conclusions

From an extensive literature review, it is found that there exist various treatments of the bed-to-wall heat transfer in CFD-DEM simulations of fluidized beds. Thus in this work, we take two kinds of mostly used approaches for a detailed analysis and comparison with reference to experimental data by Patil et al. [3]. These two approaches are i) the

thermal boundary condition approach and ii) the particle-wall conduction model. After a comprehensive study of parameter sensitivity, grid dependence, and overall performance of heat transfer, we conclude:

1. Both approaches require two input parameters, i.e., heat transfer coefficient (h_{w}) and effective bed conductivity (k_b) for the tBC approach, and cutoff distance (s) and gas layer thickness ($\mathrm{r_{lens}}$) for the PW model. Both h_{w} and k_b are very difficult to determine. Our analysis indicates that k_b needs to consider both contributions of the gas phase and solids phase (molecular and kinetic). The model applied in the current work for k_b is recommended for fluidized bed applications. Reliable estimation of h_{w} requires additional research either from experiments or detailed simulations. In contrast, the prediction of s and $\mathrm{r_{lens}}$ is much easier and reliable by estimating solid surface roughness and thermal layer thickness from empirical correlations.

2. Overall, when appropriate model parameters are used, both approaches can well describe the bed-to-wall heat exchange in CFD-DEM simulations of fluidized beds. However, the performance of the PW model is almost insensitive to the changes of the two model parameters, whereas the tBC approach shows more dependency on parameter values as well as the grid resolution.

With these conclusions, it becomes clear that caution needs to be paid for both approaches when applying them to thermal CFD-DEM simulations. For dense gas-fluidized beds, we recommend the PW model due to its robustness and the fact that detailed mechanisms are included.

Bibliography

[1] H. Zhu, Z. Zhou, R. Yang, and A. Yu. "Discrete particle simulation of particulate systems: theoretical developments". In: *Chemical Engineering Science* 62.13 (2007), pp. 3378–3396.

[2] Y. Tsuji, T. Kawaguchi, and T. Tanaka. "Discrete particle simulation of two-dimensional fluidized bed". In: *Powder technology* 77.1 (1993), pp. 79–87.

[3] A. Patil, E. Peters, and J. Kuipers. "Comparison of CFD–DEM heat transfer simulations with infrared/visual measurements". In: *Chemical Engineering Journal* 277 (2015), pp. 388–401.

[4] K. Zhang, S. Wang, B. Li, Y. He, and Y. Zhao. "Heat transfer in a pulsed fluidized bed by using coupled CFD-DEM method". In: *Powder Technology* (2020).

[5] H. Wahyudi, K. Chu, and A. Yu. "3D particle-scale modeling of gas–solids flow and heat transfer in fluidized beds with an immersed tube". In: *International Journal of Heat and Mass Transfer* 97 (2016), pp. 521–537.

[6] T. Oschmann and H. Kruggel-Emden. "A novel method for the calculation of particle heat conduction and resolved 3D wall heat transfer for the CFD/DEM approach". In: *Powder Technology* 338 (2018), pp. 289–303.

[7] Z. Li, T. Janssen, K. Buist, N. Deen, M. van Sint Annaland, and J. Kuipers. "Experimental and simulation study of heat transfer in fluidized beds with heat production". In: *Chemical Engineering Journal* 317 (2017), pp. 242–257.

[8] Q. Hou, Z. Zhou, and A. Yu. "Computational study of heat transfer in a bubbling fluidized bed with a horizontal tube". In: *AIChE journal* 58.5 (2012), pp. 1422–1434.

[9] Q. Hou, Z. Zhou, and A. Yu. "Gas–solid flow and heat transfer in fluidized beds with tubes: Effects of material properties and tube array settings". In: *Powder technology* 296 (2016), pp. 59–71.

[10] T. Lichtenegger, E. Peters, J. Kuipers, and S. Pirker. "A recurrence CFD study of heat transfer in a fluidized bed". In: *Chemical Engineering Science* 172 (2017), pp. 310–322.

[11] T. Forgber, P. Toson, S. Madlmeir, H. Kureck, J. G. Khinast, and D. Jajcevic. "Extended validation and verification of XPS/AVL-Fire™, a computational CFD-DEM software platform". In: *Powder Technology* 361 (2020), pp. 880–893.

[12] A. M. Lattanzi and C. M. Hrenya. "A coupled, multiphase heat flux boundary condition for the discrete element method". In: *Chemical Engineering Journal* 304 (2016), pp. 766–773.

[13] L. Lu, A. Morris, T. Li, and S. Benyahia. "Extension of a coarse grained particle method to simulate heat transfer in fluidized beds". In: *International Journal of Heat and Mass Transfer* 111 (2017), pp. 723–735.

[14] J. Kuipers, W. Prins, and W. P. M. Van Swaaij. “Numerical calculation of wall-to-bed heat-transfer coefficients in gas-fluidized beds”. In: *AIChE Journal* 38.7 (1992), pp. 1079–1091.

[15] M. Syamlal and D. Gidaspow. “Hydrodynamics of fluidization: prediction of wall to bed heat transfer coefficients”. In: *AIChE Journal* 31.1 (1985), pp. 127–135.

[16] D. Patil, J. Smit, M. van Sint Annaland, and J. Kuipers. “Wall-to-bed heat transfer in gas–solid bubbling fluidized beds”. In: *AIChE journal* 52.1 (2006), pp. 58–74.

[17] P. Zehner and E. Schlünder. “Wärmeleitfähigkeit von Schüttungen bei mäßigen Temperaturen”. In: *Chemie Ingenieur Technik* 42.14 (1970), pp. 933–941.

[18] M. Hunt. “Discrete element simulations for granular material flows: effective thermal conductivity and self-diffusivity”. In: *International journal of heat and mass transfer* 40.13 (1997), pp. 3059–3068.

[19] A. Schmidt and U. Renz. “Numerical prediction of heat transfer in fluidized beds by a kinetic theory of granular flows”. In: *International journal of thermal sciences* 39.9-11 (2000), pp. 871–885.

[20] D. Rong and M. Horio. “DEM simulation of char combustion in a fluidized bed”. In: *Second International Conference on CFD in the Minerals and Process Industries CSIRO, Melbourne, Australia*. 1999, pp. 65–70.

[21] A. M. Lattanzi and C. M. Hrenya. “Indirect conduction in gas–solids systems: Static vs. Dynamic effects”. In: *AIChE Journal* 63.10 (2017), pp. 4685–4693.

[22] T. Zhang and Y. Lu. “A method to deal with constant wall flux boundary condition in a fluidized bed by CFD-DEM”. In: *Chemical Engineering Journal* (2020), p. 126880.

[23] A. Morris, S. Pannala, Z. Ma, and C. Hrenya. “A conductive heat transfer model for particle flows over immersed surfaces”. In: *International Journal of Heat and Mass Transfer* 89 (2015), pp. 1277–1289.

[24] A. Morris, Z. Ma, S. Pannala, and C. Hrenya. “Simulations of heat transfer to solid particles flowing through an array of heated tubes”. In: *Solar Energy* 130 (2016), pp. 101–115.

[25] C. Goniva, C. Kloss, N. G. Deen, J. A. Kuipers, and S. Pirker. “Influence of rolling friction on single spout fluidized bed simulation”. In: *Particuology* 10.5 (2012), pp. 582–591.

[26] R. Beetstra, M. A. van der Hoef, and J. Kuipers. “Drag force of intermediate Reynolds number flow past mono-and bidisperse arrays of spheres”. In: *AIChE journal* 53.2 (2007), pp. 489–501.

[27] D. Gunn. “Transfer of heat or mass to particles in fixed and fluidised beds”. In: *International Journal of Heat and Mass Transfer* 21.4 (1978), pp. 467–476.

[28] C. Kloss, C. Goniva, A. Hager, S. Amberger, and S. Pirker. “Models, algorithms and validation for opensource DEM and CFD–DEM”. In: *Progress in Computational Fluid Dynamics, an International Journal* 12.2-3 (2012), pp. 140–152.

[29] P. A. Cundall and O. D. Strack. “A discrete numerical model for granular assemblies”. In: *geotechnique* 29.1 (1979), pp. 47–65.

[30] G. Flamant and T. Menigault. “Combined wall-to-fluidized bed heat transfer. Bubbles and emulsion contributions at high temperature”. In: *International journal of heat and mass transfer* 30.9 (1987), pp. 1803–1812.

[31] L. Armstrong, S. Gu, and K. Luo. “Study of wall-to-bed heat transfer in a bubbling fluidised bed using the kinetic theory of granular flow”. In: *International journal of heat and mass transfer* 53.21-22 (2010), pp. 4949–4959.

[32] R. Yusuf, B. Halvorsen, and M. C. Melaaen. “Eulerian–Eulerian simulation of heat transfer between a gas–solid fluidized bed and an immersed tube-bank with horizontal tubes”. In: *Chemical engineering science* 66.8 (2011), pp. 1550–1564.

[33] R. Yusuf, B. Halvorsen, and M. C. Melaaen. “An experimental and computational study of wall to bed heat transfer in a bubbling gas–solid fluidized bed”. In: *International Journal of Multiphase Flow* 42 (2012), pp. 9–23.

[34] V. Natarajan and M. Hunt. “Kinetic theory analysis of heat transfer in granular flows”. In: *International journal of heat and mass transfer* 41.13 (1998), pp. 1929–1944.

[35] S. Chapmann and T. Cowling. *The Mathematical Theory of Non-Uniform Gases. 1970.*

[36] G. K. Batchelor and R. O’brien. “Thermal or electrical conduction through a granular material”. In: *Proceedings of the Royal Society of London. A. Mathematical and Physical Sciences* 355.1682 (1977), pp. 313–333.

[37] A. Xavier and J. Davidson. “Heat transfer to surfaces immersed in fluidized beds, particularly tube arrays”. In: *Fluidization*. Cambridge University Press Cambridge, 1978, pp. 333–338.

[38] D. Kunii and O. Levenspiel. *Fluidization engineering*. Butterworth-Heinemann, 1991.

[39] N. Deen, M. V. S. Annaland, M. A. Van der Hoef, and J. Kuipers. “Review of discrete particle modeling of fluidized beds”. In: *Chemical engineering science* 62.1-2 (2007), pp. 28–44.

[40] D. Kunii and O. Levenspiel. “A general equation for the heat-transfer coefficient at wall surfaces of gas/solid contactors”. In: *Industrial & engineering chemistry research* 30.1 (1991), pp. 136–141.

[41] N. G. Deen, S. H. Kriebitzsch, M. A. van der Hoef, and J. Kuipers. “Direct numerical simulation of flow and heat transfer in dense fluid–particle systems”. In: *Chemical engineering science* 81 (2012), pp. 329–344.

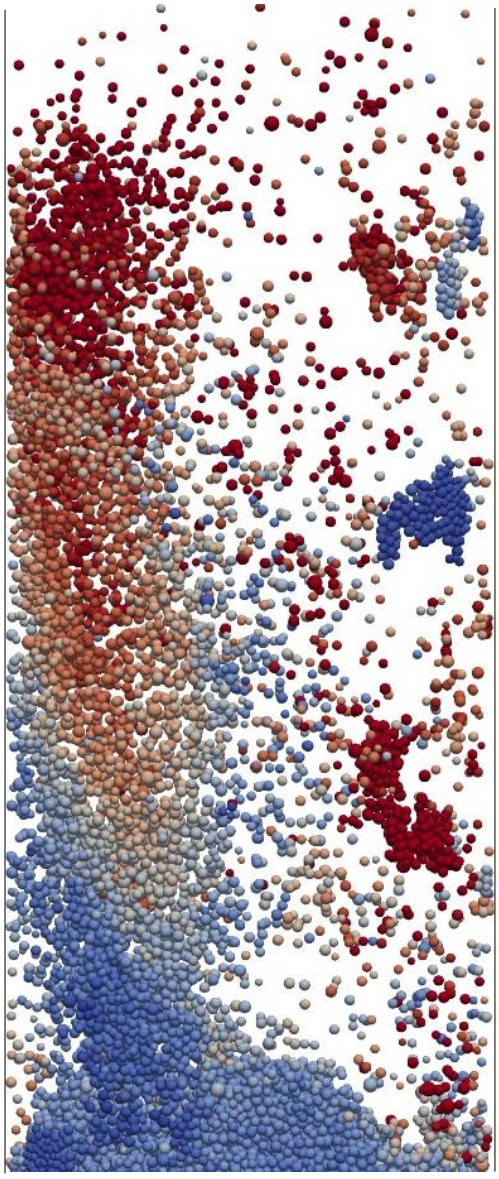

5

SIMULATION ON AGGLOMERATION

This chapter is based on: X. Liu, C. J. M. Hessels, N. G. Deen, Y. Tang:
CFD-DEM investigation on the (de-)fluidization behavior of combusted iron fines in a fluidized bed. Fuel, 2023. (Under review)

Abstract

The occurrence of agglomeration due to particle sintering is one of the most significant technical issues hindering the direct reduction process of iron oxide fines in a high-temperature fluidized bed. To get a better understanding of the agglomeration mechanism, the (de-)fluidization behavior of micron-sized iron oxide particles in a 3D fluidized bed is investigated using Computational Fluid Dynamics coupled with a coarse-grained Discrete Element Method (CFD-cgDEM). The inter-particle cohesive force is considered as a temperature-dependent solid bridge force. The coarse-grained method is first verified by comparing results for different scaling factors. Subsequently, the effects of temperature on the bed pressure drop, void fraction distribution, particle velocity distribution, and agglomerate size are investigated. In conclusion, the developed model shows the capacity for reliable prediction of particle agglomeration behavior, which can shed light on the design of the DRI process in high-temperature fluidized beds.

5.1. Introduction

Energy supply is an important commodity of our modern society. Based on the present situation of the world's energy supply, it is not doubted that our energy and transportation systems must transit away from fossil-fuel sources to zero-carbon clean and renewable energy sources to mitigate global climate change. Recently, metal fuels have been proposed as a promising clean energy carrier due to their high energy density and lack of carbon dioxide emissions [1, 2]. With the high volumetric energy density and abundant availability, (micron-sized) iron powders are first considered [3–6]. Iron powders are combusted to generate heat. After combustion, direct reduction of the iron oxides (DRI) using sustainable energy (e.g. H_2) is the key to closing this iron fuel cycle with CO_2-free characteristics [7, 8]. However, there is one problem: agglomeration due to particle sintering commonly occurs during the chemical reduction of iron oxides at elevated temperatures. This agglomeration/sintering behavior has also been observed in reactors such as fluidized beds that promote solid mixing and good mass/heat transfer [9]. Consequently, improper fluidization involving channelling or even de-fluidization occurs, which hinders the process efficiency. For an effective design of fluidized bed DRI, it is therefore crucial to understand the agglomeration and de-fluidization behavior of iron/iron oxide fines at elevated temperatures.

It is well known that agglomeration/defluidization is the result of interparticle forces [10–13]. These interparticle forces may be of several types including the van der Waals force, electrostatic force, and interfacial forces due to solid bridges or liquid bridges. Any of these interparticle forces may take a dominant role in particular circumstances. The formation of agglomerates via a solid bridge force is a well-recognized feature in high temperature fluidized bed during the reduction process of iron oxides [14]. Many factors may influence the agglomeration/sintering behavior of iron/iron oxide particles, including the physical properties of the particles and the operation conditions [15, 16]. The physical properties of particles include their composition, microstructure, size, and so on, whereas the operation conditions include the temperature, reducing gas composition, gas flow rate, etc. Therefore, this solid bridge induced agglomeration phenomenon is difficult to characterize.

Experiments on investigating the agglomeration phenomenon are quite expensive, and it is difficult to interpret the complex behavior of bubbles and agglomeration. Therefore, numerical simulations (e.g. coupled CFD-DEM method) provide a powerful tool to investigate the fluidization phenomenon inside a fluidized bed. Kuwagi et al. [12] developed a DEM model for metallic solid bridging by surface diffusion mechanism including the effect of surface roughness. In their model, the sintering forces are based on iron particles with the diameter of 200 μm. Mansourpour et.al [17, 18] investigated the sintering behavior based on the viscous mechanism for polyethylene particles by CFD-DEM simulations and the influence of gas velocity/temperature on the size of agglomerates. Although these studies have been made using CFD-DEM simulations for the study of sintering behavior in fluidized beds, few studies can be found for iron/iron oxides fines, particularly classified as group A or C particles in a fluidized bed.

The micron-sized cohesive iron/iron oxide powder provides a challenge for the computational simulation cost of the DEM due to the large number of particles particularly for modeling realistic industrial processes. To reduce the number of computational entities,

so-called coarse-grained DEM models have been developed [19]. The concept of coarse graining is that a group of the original particles is represented by large-sized coarse-grained particles (often called “parcels"), whose behavior is kept equivalent to the original particles by appropriate scaling. Previous efforts have been made for studying the cohesive systems with applying coarse-grained method. Chen et al. [20] derived the scaling law of the Johnson-Kendall-Roberts (JKR) contact model for adhesive viscoelastic particles. Sakai et al. [21] performed CFD-DEM simulations for fluidized beds dominated by van der Waals force, and the coarse-grained model shows very good agreement with the original simulations. These investigations on the dynamic behavior of agglomeration can handle large-scale systems. However, regarding the agglomeration/defluidization behavior in the reduction process of iron oxides, it is a severe problem that usually occurs in high temperature fluidized beds and differ with specific situations [14]. To this end, we need a better understanding of how the sintering behavior of iron/iron oxides (agglomerates' growth) is affected by the fluidizing conditions. Only then it is possible to develop strategies that prevent/limit such agglomeration issue.

In the present work, we perform numerical modeling of fluidization of micron-sized iron oxide particles in a fluidized bed at elevated temperature using a CFD-cgDEM method. We examine the effect of temperature and different sintering force models characterized by the surface roughness on the (de-)fluidization behavior, and different scaling factors are employed to verify the effectiveness of the coarse-grained method. This paper is organized as follows: Section 5.2 gives the details of the CFD-DEM method as well as implementation of the solid bridge. Subsequently, the description of the numerical geometry and parameters are given in Section 5.3. In Section 5.4, results are presented with respect to the verification of the scaling method and effects of temperature and sintering force models on the bed dynamics. Finally, conclusions are summarized in Section 5.5.

5.2. Numerical model

For the simulations in this work we use the unresolved discrete particle model, i.e., the open source CFD-DEM package CFDEM®coupling based on OpenFOAM [22] and LIGGGHTS [23].

5.2.1. CFD-DEM model

In the CFD-DEM method, the gas phase is described by the continuity and Navier-Stokes equations:

$$\frac{\partial\left(\varepsilon_{\mathrm{f}}\rho_{\mathrm{f}}\right)}{\partial t}+\nabla\cdot\left(\varepsilon_{\mathrm{f}}\rho_{\mathrm{f}}\mathbf{u}_{\mathrm{f}}\right)=0 \tag{5.1}$$

$$\frac{\partial\left(\varepsilon_{\mathrm{f}}\rho_{\mathrm{f}}\mathbf{u}_{\mathrm{f}}\right)}{\partial t}+\nabla\cdot\left(\varepsilon_{\mathrm{f}}\rho_{\mathrm{f}}\mathbf{u}_{\mathrm{f}}\mathbf{u}_{\mathrm{f}}\right)=-\varepsilon_{\mathrm{f}}\nabla p+\varepsilon_{\mathrm{f}}\nabla\cdot\tau_{\mathrm{f}}-\mathbf{S}+\varepsilon_{\mathrm{f}}\rho_{\mathrm{f}}\mathbf{g} \tag{5.2}$$

where ρ_{f}, $\mathbf{u}_{\mathrm{f}}$, and p are the gas density, gas velocity and pressure, respectively. ε_{f} is the gas phase voidage of current computational cell. $\mathbf{S}$ represents the source term accounting for the momentum exchange between particles and fluid:

$$\mathbf{S}=\frac{1}{\Delta\mathrm{V}}\sum_{i=1}^{n}\frac{\mathrm{V}_{p,i}\beta}{1-\varepsilon_{\mathrm{f}}}(\mathbf{u}_{\mathrm{f}}-\mathbf{v}_{\mathrm{p}})D(\mathbf{r}-\mathbf{r}_{i}) \tag{5.3}$$

where n is the number of particles located in the Eulerian grid with cell volume ΔV. $V_{p,i}$ and $\mathbf{v}_p$ are the particle volume and velocity. β is the gas-particle momentum exchange coefficient. In this work, the Beetstra drag force correlation [24] has been used to calculate the interphase momentum transfer coefficient. D is the distribution function, which is used to distribute the force exerted by the particles on the gas phase in the Eulerian grid cell.

τ_f is the viscous stress tensor for the gas phase assuming a Newtonian fluid:

$$\tau_f = \mu_f \left[\left((\nabla \mathbf{u}_f) + (\nabla \mathbf{u}_f)^T \right) - \frac{2}{3} \mathbf{I} (\nabla \cdot \mathbf{u}_f) \right] \tag{5.4}$$

where μ_f is the gas phase viscosity. $\mathbf{I}$ is the second order metric tensor.

The particles are individually tracked based on the soft sphere approach which has been implemented in the open source package LIGGGHTS [25]. The motion of a single spherical particle with mass m_i and moment of inertia I_i can be described by Newton's second law:

$$m_i \frac{d\mathbf{v}_i}{dt} = m_i \mathbf{g} - V_i \nabla p + \mathbf{F}_{d,i} + \mathbf{F}_{c,i} + \mathbf{F}_{coh,i} \tag{5.5}$$

$$I_i \frac{d\boldsymbol{\omega}_i}{dt} = \mathbf{T}_i \tag{5.6}$$

where $\boldsymbol{\omega}_i$ and $\mathbf{T}_i$ are the angular velocity and the torque resulting from the collision of the particles, respectively. The forces on the right-hand side are due to the gravity, the pressure gradient, the drag, the contact forces and the cohesive forces between colliding particles. A soft-sphere model is used to simulate the contact force as proposed by Cundall and Strack [26]. The cohesive force ($\mathbf{F}_{coh,i}$) is discussed in the following subsections.

5.2.2. Cohesive force

In gas-fluidized beds, besides contact forces, some other interparticle forces may also become noticeable in some certain circumstances, e.g., van der Waals force, electrostatic force, liquid bridge force and solid bridge force [13]. In current research, we are concerned with interparticle forces related to cohesive behavior for iron/iron oxides particles at elevated temperatures. Therefore, the inherent interparticle cohesive force considers only the temperature-dependent solid bridge force. The solid bridge force, i.e., a sintering force, usually occurs in the system where the bonding of two or more particles takes place with the application of heat and at temperatures below the melting point of any component of the system [27]. The reduction of iron oxides is normally conducted at high temperatures ($> 500\,^{\circ}C$), where particle surface becomes sticky and soft. Thus, it is easy to form permanent solid bridge between colliding particles. The study of Knight et al. [28] has shown that the sintering mechanism of iron powder follows surface diffusion due to the migration of the flow of atoms from the surface part to the junction. The solid bridge force between two particles in contact can be expressed as [29]:

$$\mathbf{F}_{sb,ij} = \pi \sigma x^2 \tag{5.7}$$

where σ is the tensile strength of a neck between particles. x is the neck radius. Kuczynski's [27] surface diffusion model describes the neck size due to solid bridge force between two particles:

$$x = \left(\frac{56\gamma\delta^4}{KT} D_s a^3 t \right)^{1/7} \tag{5.8}$$

where γ, δ, K, T, a, and t represent the surface tension, lattice constant, Boltzmann constant, temperature, curvature radius and contact time. D_s is the surface diffusion coefficient, which is calculated based on frequency factor $D_{o,s}$ and activation energy E_s:

$$D_s = D_{o,s} \exp\left(\frac{-E_s}{RT} \right) \tag{5.9}$$

The curvature radius depends on the particle's surface structure, and can be approximated by the particle's radius for a smooth-surface particle. The surface roughness is chosen as the curvature radius for non-smooth particles. The study of Kuwagi et al. [12] reports the solid bridge force models by a general equation:

$$\mathbf{F}_{\mathrm{sb},ij} = \mathrm{C}\pi\sigma_{neck} \left(\frac{56\gamma\delta^4}{KT} D_s \mathrm{r_p^3} t \right)^{2/7} \tag{5.10}$$

with C = 0.417, 1, and 1.251 representing the three-microcontact-point model, the smooth surface model, and the nine-microcontact-point model, respectively.

The contact time t is another key parameter in eq. (5.10). In our simulation, since solid bridge formation only occurs between particles in contact, at each time step (Δt_{DEM}) we can divide the cohesive behavior of the particles into two types, based on whether the particles have collided in the previous time step: (i) if the two particles did not contact in previous time step, the contact time is taken as Δt_{DEM}, and the contact time will be stored. (ii) If two particles remain in contact from the previous time step, the contact time is accumulated:

$$t_{\mathrm{con}}^{n+1} = t_{\mathrm{con}}^{n} + \Delta t_{\mathrm{DEM}} \tag{5.11}$$

where t_{con}^{n} is the previous contact time.

In the DEM model, usually a smaller Young's modulus is adopted to allow a larger time step and reduce the computational cost. As a consequence, a longer collision time (see eq. (5.12)) is obtained, which results in an overprediction of the contact time between the particles. In order to correct for this overestimation, a correction factor c is adopted to correct the contact time by ct when calculating the neck size (see eq. (5.13)). The corrected factor is determined as:

$$t = 2.868 \left(\frac{\mathrm{m}^{*2}}{\mathrm{Y}^{*2}\mathrm{r}^{*}\nu_{\mathrm{n,ij}}} \right)^{1/5} \tag{5.12}$$

$$x = \left(\frac{56\gamma\delta^4}{KT} D_s a^3 c t \right)^{1/7} \tag{5.13}$$

with:

$$c = \left(\frac{\mathrm{Y}^{*}_{\mathrm{DEM}}}{\mathrm{Y}^{*}_{\mathrm{real}}} \right)^{2/5} \tag{5.14}$$

where $v_{n,ij}$ is the particle relative velocity; r^*, Y^*, and m^* are the effective particle radius, effective elastic moduli, and effective particle mass, which are defined by:

$$\frac{1}{r^*} = \frac{1}{r_i} + \frac{1}{r_j}, \frac{1}{Y^*} = \left(\frac{1-\nu_i^2}{Y_i}\right) + \left(\frac{1-\nu_j^2}{Y_j}\right), \frac{1}{m^*} = \frac{1}{m_i} + \frac{1}{m_j} \tag{5.15}$$

where ν is the Poisson's ratio.

5.2.3. Scaling method

The scaling rules of particle contacts follow the approach proposed by Radl [30], namely, the normal spring and tangential spring constants are scaled by K (= $d_{parcel}/d_{particle}$), and the normal damping constant and tangential damping constant are scaled by a factor K^2. In this work we extend this scaling procedure with the cohesive force in eq. (5.10) by ensuring that an additional dimensionless group remains constant [19]:

$$\Pi = \frac{\mathbf{F}_{coh}}{r_p^2 \rho_p \mathbf{v}_0^2} \tag{5.16}$$

Since the sintering force ($\mathbf{F}_{coh}$) is time-dependent (eq. (5.10)), an additional dimensionless expression is required for the contact time to obtain an appropriate scaling:

$$t^* = t\mathbf{v}_o / r_p \tag{5.17}$$

Combining eqs. (5.10) and (5.17), the dimensionless group (eq. (5.16)) can be rewritten as:

$$\Pi = \frac{A t^{2/7}}{r_p^2 \rho_p \mathbf{v}_0^2} = \frac{A}{r_p^2 \rho_p \mathbf{v}_0^2} \left(\frac{r_p}{\mathbf{v}_0}\right)^{2/7} \left(\frac{t\mathbf{v}_0}{r_p}\right)^{2/7} = B\left(\frac{t\mathbf{v}_0}{r_p}\right)^{2/7} \tag{5.18}$$

with:

$$A = C\pi\sigma_{neck}\left(\frac{56\gamma\delta^4}{KT} D_s r_p^3\right)^{2/7}, B = \frac{A}{r_p^{12/7} \rho_p \mathbf{v}_0^{16/7}} \tag{5.19}$$

As can been seen from eq. (5.19), the constant A is determined by the material properties. A proper scaling would be obtained only if B is kept constant. Since the reference velocity ($\mathbf{v}_0$) is expected to be the same in both the original and scaled systems, matching Π (in eq. (5.18)) requires that the material property constant A should scale with $K^{12/7}$:

$$\frac{A_{prim}}{r_{prim}^{12/7}} = \frac{A_{parcel}}{r_{parcel}^{12/7}} \tag{5.20}$$

5.3. Simulation settings

5.3.1. Setup

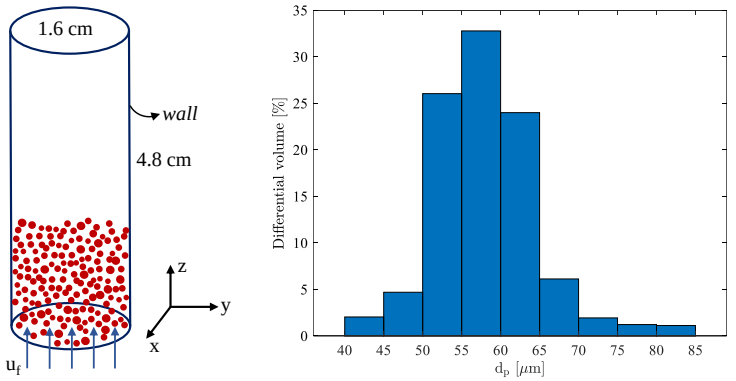

(a) (b)

Figure 5.1: (a) Simulation domain; (b) Original (unscaled) particle size distribution (d50 = 58 μm).

Simulations for the cohesive behavior are carried out in a gas-fluidized bed with an inner diameter of 1.6 cm, as shown in Figure 5.1(a), which is based on our previous lab-scale experimental work in Chapter 2. Experimentally, the height of the cylinder is quite large. To save simulation cost, a height of three and six times of the inner diameter (4.8 cm or 9.6 cm) is used in the numerical study depending on specific cases. A total of 0.01 kg polydisperse combusted iron particles are charged into the bed. The size distribution of primary particles with the corresponding volume fractions is given in Figure 5.1(b). The coarse-grained method has been used in this work due to the large number of the particles in the system. As such, the total number of particles reduces from 20M to 315K or 93K particles when applying a coarse-grained factor (K) of 4 or 6, respectively. To define the grid, an average grid to particle size ratio of 3 with respect to the scaled mean particle size (d50) is used, and a constant smoothing length of $3 \cdot d50$ is chosen to avoid any computational issues due to the rather fine grid.

5.3.2. Settings and parameters

In the simulations, the inlet gas (N_2) velocity is uniformly distributed, and the cylinder wall is regarded as an adiabatic boundary condition. The outlet condition is considered as ambient pressure to mimic the real experimental condition. The simulation settings and the properties of particles (combusted iron) are listed in Table 5.1. Note that in this study, the physical properties of the wall for the calculation of the sintering are chosen to be the same as that of the particles in order to simplify the particle-wall sticking. The material tensile strength depends on operating temperatures is chosen from the work of Hidaka et al. [31]. Gas phase properties, e.g., heat capacity, thermal conductivity, viscosity, and density are applied as constants based on the specific operating temperatures. The

Table 5.1: Physical properties and settings used in the simulations.

Particle properties	Value	Source
Coefficient of restitution e	0.9	
Coefficient of friction μ	0.5	
Density ρ_{p}	5240 kg/m^3	
Lattice constant δ	1.38×10^{-9} (m)	
Poisson's ratio ν	0.12	[32]
Young's modulus E	359 GPa	[32]
Surface tension γ	1 N/m	[33]
Frequency factor $D_{o,s}$	2.8×10^{-13} ($\leq 900\,^{\circ}$C) m^2/s	[34]
	1.6×10^{5} ($> 900\,^{\circ}$C) m^2/s	[34]
Activation energy E_s	1.74×10^{5} ($\leq 900\,^{\circ}$C) J/mol	[34]
	5.79×10^{5} ($> 900\,^{\circ}$C) J/mol	[34]
Simulation settings		
Bed mass m_{b}	10 g	
CFD time step Δt_{CFD}	5.0×10^{-5} s	
DEM time step Δt_{DEM}	5.0×10^{-7} s	
Scaling factor K	4, 6	

DEM timestep which is related to the contact time (eq. (5.11)) is one of the significant parameters to determine the sintering force. In order to well capture the sintering contact between particles, the DEM timestep is chosen as 5e-7 s, which is around 50 times smaller than the Hertz collision time (eq. (5.12)).

Simulations of fluidization/sintering are performed at temperatures ranging from 500 °C to 1000 °C without sintering force and with variant sintering force models (i.e. three-microcontact-point model (C = 0.417), smooth-surface model (C = 1), and nine-microcontact-point model (C = 1.251)). The cases without sintering force serve as benchmarks. Note that when performing the simulations, the sintering force is only activated after 1.0 s to avoid any artificial large bonding behavior during the initial packing stage. By comparing simulation results with available experimental data/observation, we can propose a methodology/model which can be applied to systems where complex agglomeration/defluidization is present.

5.4. Results and discussions

In this section, the results of simulation cases considering different magnitudes of sintering forces are discussed. The results are analyzed in the form of the bed pressure drop, particle velocity PDF, and agglomeration size. Additionally, snapshots of void fraction and particle velocity distribution are shown.

5.4.1. Validation/verification for the numerical settings

Prediction of minimum fluidization velocity

The prediction of the minimum fluidization velocity (u_{mf}) is considered to validate the CFD-DEM modeling of hydrodynamics of the combusted iron particles. The minimum fluidization velocity (u_{mf}) is defined as the superficial gas velocity at which the drag force of the upward moving gas becomes equal to the weight of the particles in the bed, which is one of the most important parameters associated with a fluidized bed system. Numerical simulations to determine u_{mf} are conducted under N_2 atmosphere at 20 °C in a similar way as in the experiment: the superficial gas velocity firstly increases to a high value where an obvious bubbling fluidization can be observed, and then decreases gradually from this point to zero in a total time period of 10 s. The u_{mf} is determined as the intersection point between the fixed bed pressure drop curve and the average pressure drop of the fluidized bed using decreasing velocities.

Figure 5.2 shows the u_{mf} obtained by simulation. The result shows that u_{mf} is about 0.101 m/s, which matches well with the theoretical results (0.0107 m/s) calculated using the Beestra correlation [24] (with $\varepsilon_{mf} = 0.4$). We do find that some differences between the simulation tests and our previous experimental results which is 0.091 m/s [14]. This might be due to slight differences of the particle size distribution between simulation and experimental study. When predicting u_{mf} by simulation, we remove those tiny/large particles from the distribution if their differential volume is less than 5% due to simulation limitation. In general, simulation results match well with the theoretical predictions, indicating the correct implementation of hydrodynamics.

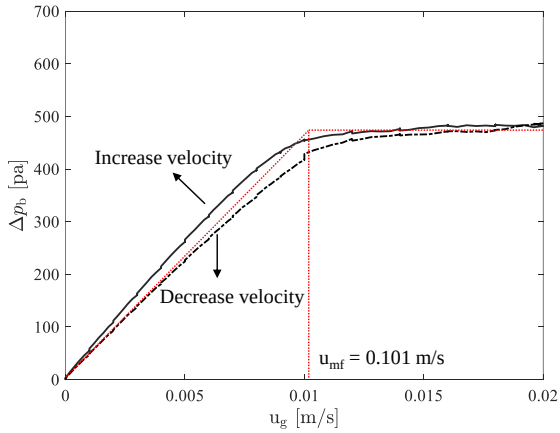

Figure 5.2: Minimum fluidization velocity tested by simulation.

Verification of the scaling method for sintering force

To verify the coarse-grained approach (particularly the scaling of the sintering force model), simulations employing different scaling factors of 4 and 6 have been compared. When K = 6 the total number of particles in the system is 3.4 times less compared to the case when K = 4. Figure 5.3 compares the bed pressure drop versus time for both cases for

different magnitudes of the sintering force model at a temperature of 1000 °C. Note that the standard deviation (STD) is calculated from 1.5 s to 5 s. It can be seen that, for both sintering force models, the bed dynamics indicated by the mean and standard deviation of the pressure drop predicted with both scaling factors agree well, indicating that the correct scaling is applied.

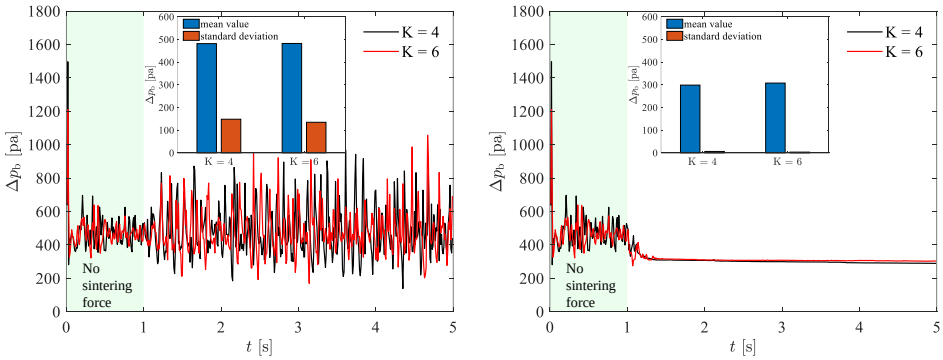

Figure 5.3: Verification of the scaling method based on different sintering force models at 1000 °C. (a) three-microcontact-point model (C = 0.417); (b) nine-microcontact-point model (C = 1.251).

5.4.2. Influence of the physical properties

Effects of the temperature and the strength of the solid bridge forces

With confidence in the coarse-grained CFD-DEM model, we now investigate the effect of the solid bridge strength (via different temperatures and sintering force models) on the bed dynamics. Figure 5.4 shows the bed pressure drop profiles in time using different sintering force models at temperatures 500 – 1000 °C. The standard deviation (STD) is calculated from 1.5 s to 10 s. Clearly, for all non-cohesive cases, the bed pressure drop slightly fluctuates around a mean value of 480 Pa, indicating a smooth bubbling fluidization. Additionally, the sintering force has a minor effect on the bed pressure drop at low temperature cases (i.e. 500 °C and 650 °C) since a similar bed pressure profile is obtained from the non-cohesive cases and the cohesive cases. When cohesiveness of the particles (C > 0) is considered at higher temperatures (i.e. 800 °C and 1000 °C), the fluctuations represented by the standard deviations (STD) first increase with increasing the magnitude of the sintering force, i.e., larger force at higher temperature (800 °C). With further increasing the magnitude of the sintering force, i.e., at 1000 °C when C ≥ 1, the bed pressure drop decreases immediately, indicating fast defluidization.

Looking at 800 °C, the standard deviation of pressure drop is much larger when the smooth-surface (C = 1) or nine-microcontact-point (C = 1.251) sintering force model is used compared to the pressure drop obtained from the three-microcontact-point (C = 0.417) sintering force model. This larger fluctuation indicates an increase of the bubble size, which induces more vigorous bed dynamics. The sintering force calculated by the smooth-surface/nine-microcontact-point model is essentially about 2.4/3 times larger

than the force calculated by the three-microcontact-point model (C = 0.417). Consequently, the degree of particle agglomeration increases, resulting in enhanced inhomogeneity in the bed. This enhancement is more significant at temperature of 1000 °C for three-microcontact-point sintering model, where the sintering force becomes dominant. With larger sintering force by the smooth-surface/nine-microcontact-point model at 1000 °C, the entire bed quickly freezes as de-fluidization occurs.

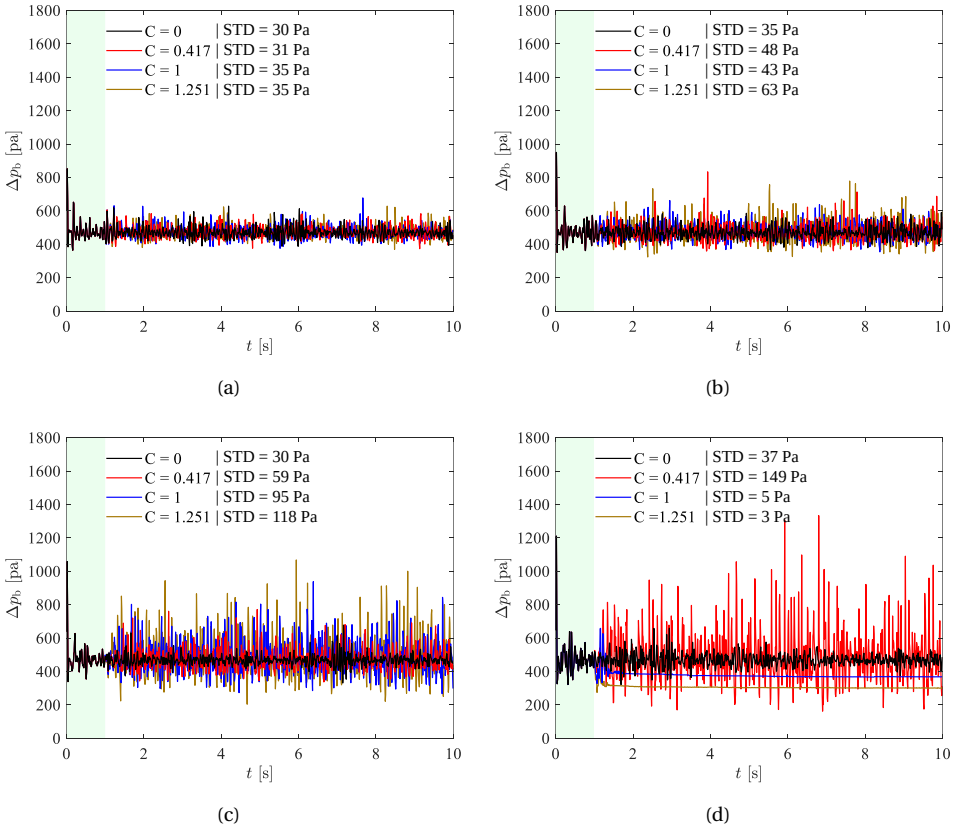

Figure 5.4: Pressure drop profiles over time for different cases. (a) 500 °C; (b) 650 °C; (c) 800 °C; (d) 1000 °C.

To support the discussion above, we show the instantaneous void fraction distribution and particle velocity distribution in Figures 5.5 and 5.6, respectively. The snapshots of instantaneous void fraction distribution from the non-cohesive cases at all temperatures clearly show a smooth and homogeneous fluidization with a fluid-like behavior of the solid phase. At lower temperatures (500 °C and 650 °C), with applying the sintering force model, the fluidization is still homogeneous. With an increase of the solid bridge strength by larger sintering force at a temperature of 800 °C, a clear decrease of the bed height and inhomogeneity of the flow can be observed from Figures 5.5(c) and 5.6(a). This indicates that the effect of the sintering force becomes pronounced.

Similar but more significant defluidization behavior can be observed at 1000 °C. At

this higher temperature, the magnitude of the sintering force is increased since the force is highly depending on the temperature. Therefore, a significant effect of particle sintering on the flow pattern can already be seen in the three-microcontact-point force model case. After about 1.5 s, the bed expansion significantly decreases, channeling flow occurs, and formation of agglomerates can clearly be seen in Figures 5.5(d) and 5.6(b). All these observations are in line with the large fluctuations of pressure drop presented in Figure 5.4. With increase of the solid bridge strength by larger sintering force to smooth-surface force model/nine-microcontact-point model, the bed quickly freezes after 1.5 s. From Figure 5.6, we can see the formation of much larger agglomerates and strong sticking of particles on the bed wall. This indicates that the solid bridge force predicted with this model at this temperature is very large such that once two particles come in contact a strong and permanent bond is immediately formed.

Earlier, we have done experiments of the fluidization of iron oxides powders at different temperatures with the same conditions as in the current simulations [14]. Overall, the results from these simulations reflect the experimental observations in Chapter 2. Experiments of fluidization at 500 °C and 650 °C can run for more than two hours without any indication of de-fluidization, whereas the experiments at 950 °C quickly show improper fluidization behavior and eventually de-fluidization occurs within a few minutes. Additionally, from Figure 5.6 we notice that the particles at the bottom show a lower velocity while the particles near the top of the bed show a higher velocity. This agrees with our experimental observation, i.e., the occurrence of the initial dead zone is always at the bottom of the bed. Overall, we believe the prediction of the solid bridge strength by the smooth-surface sintering model or the nine-microcontact-point sintering force model model gives best agreement with our experiments.

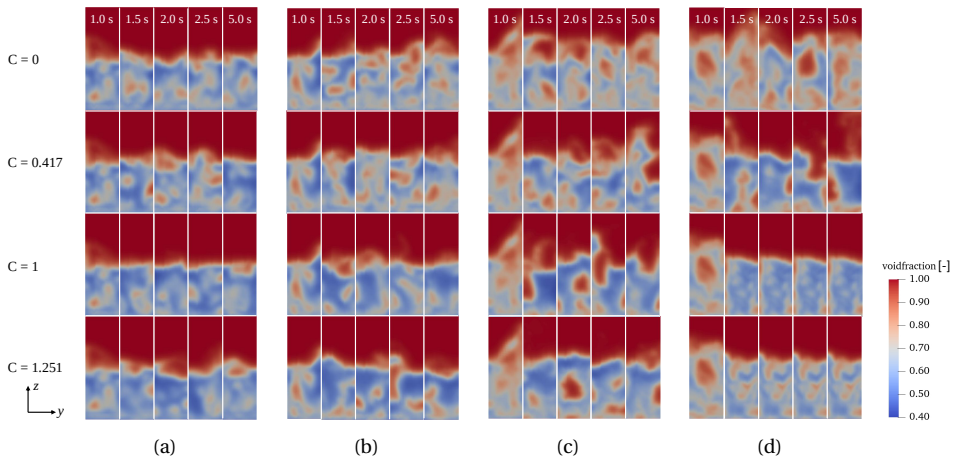

Figure 5.5: Snapshots of instantaneous void fraction distribution for different cases. (a) 500 °C; (b) 650 °C; (c) 800 °C; (d) 1000 °C.

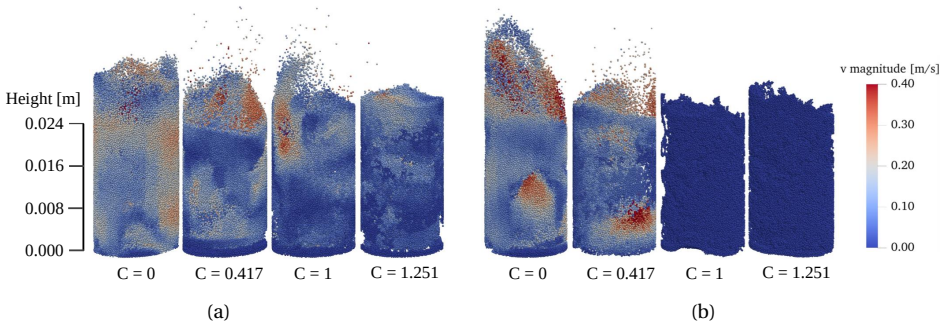

Figure 5.6: Snapshots of bed structure particle velocity distribution at t = 2.0 s for different cases. (a) 800 °C; (b) 1000 °C.

According to eq. (5.10), the solid bridge neck size increases with contact time and temperature of the particles. Regarding the effect of contact time, sintering/agglomeration initially occurs in the bottom region of the bed particular at the corner of the bed due to the high density, as shown in Figure 5.6. This will result in a longer contact time in these regions and formation of permanent agglomerates that grow bigger and bigger by sticking more particles/agglomerates. This leads to the initial dead/defluidized zone of the bed, which agrees well with the experimental observation. Higher temperatures can increase the diffusion rate of the atom migration from the surface area to the connecting point based on the surface diffusion mechanism, leading to a strong strength of solid bridge and increasing the possibility of forming permanent solid bride between colliding particles.

To get quantitative information of the sintering behavior, the particle velocity PDF is plotted at temperatures of 800 °C and 1000 °C, as shown in Figure 5.7. At a temperature of 800 °C, when applying the non-sintering/three-microconact model in the system, the particle velocity PDF distributes in a similar range for all instants, indicating a healthy and homogeneous fluidization behavior. Further increasing the sintering force (higher C) shows a distinct profile compared to the non-cohesive cases, since a severe unstable fluidization occurs. Agglomerates are forming and breaking frequently, and slugging might occur. We notice that comparing to the non-cohesive case, the entire particle velocity PDF region shifts to the low velocity region, indicating that the sintering force is pronounced. Such trends can clearly be seen in the cases of $C \geq 1$ at 1000 °C, i.e., the particle velocity PDF clearly shifts to the low velocity region with the increase of time. In the end, almost all the particle velocities are close to zero, meaning the occurrence of defluidization.

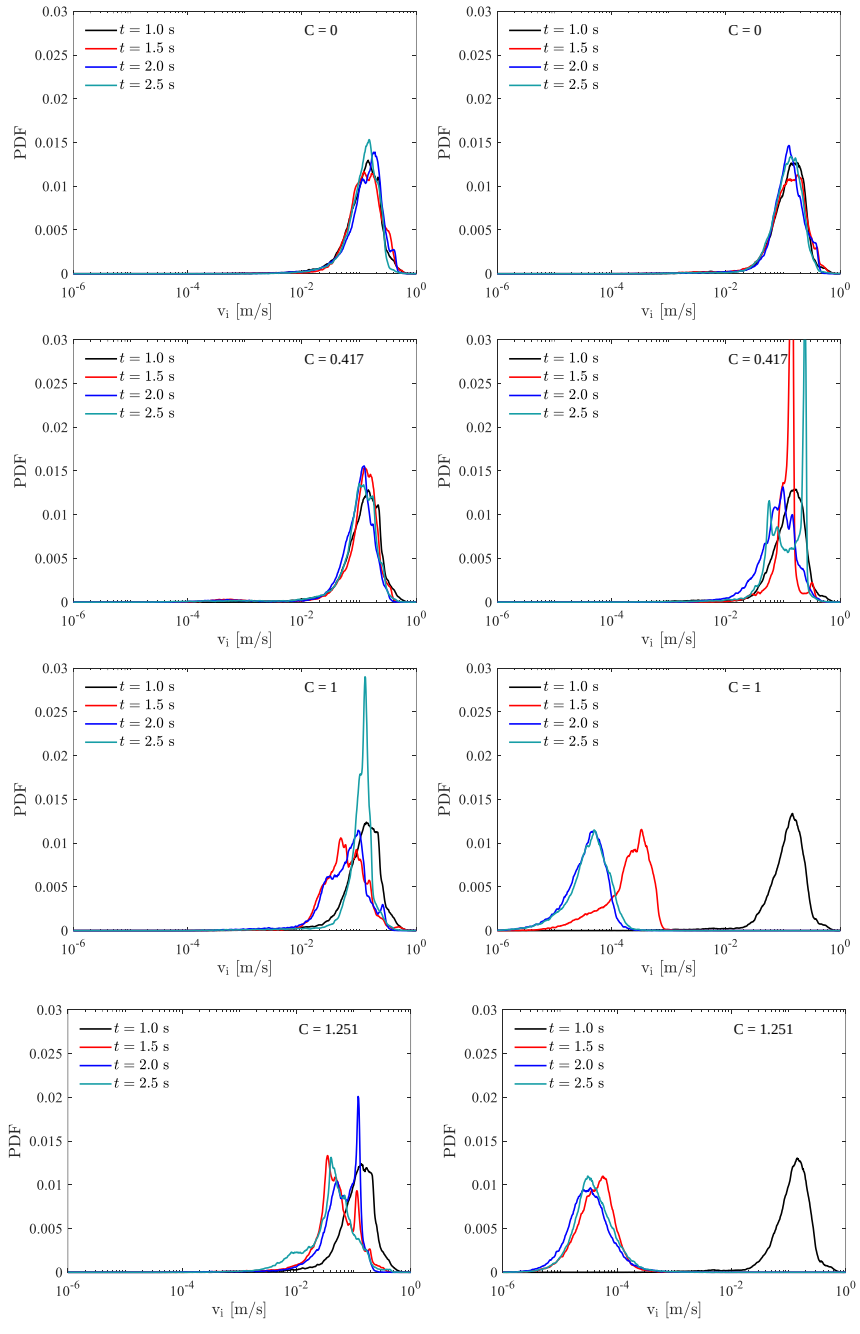

Figure 5.7: Particle velocity PDF at four instantaneous times when applying different models. (a) 800 °C; (b) 1000 °C.

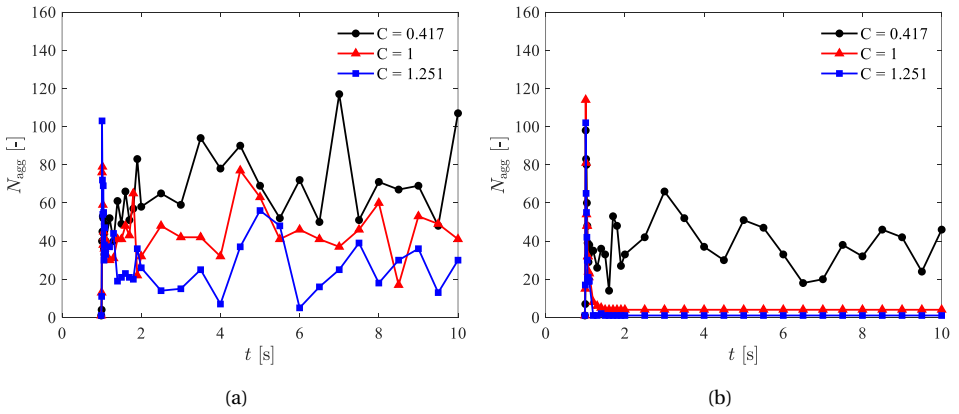

Figure 5.8: The number of agglomerates in the bed over time for kinds of sintering cases. (a) 800 °C; (b) 1000 °C.

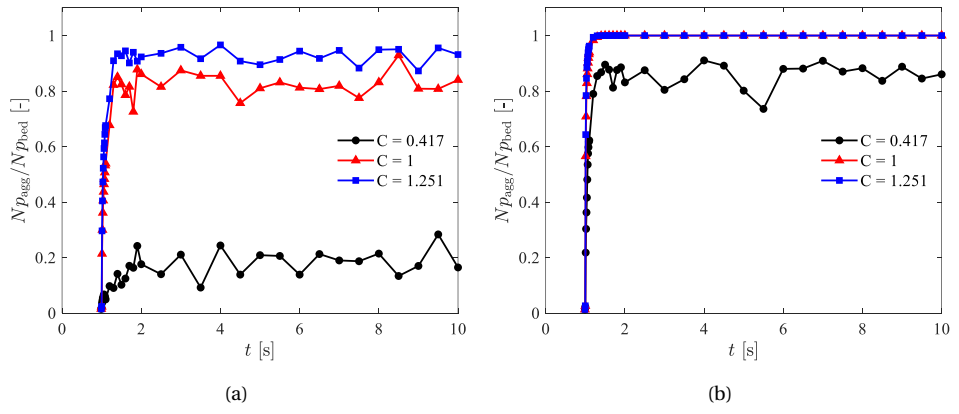

Figure 5.9: The fraction of the bed agglomerates (the number of particles in agglomerates divided by the total number of particles in the bed) over time for different kinds of sintering cases. (a) 800 °C; (b) 1000 °C.

In order to know how the agglomerates are formed, we further plot the number of the agglomerates formed in the system and the fraction of all particles in those agglomerates over time, as shown in Figures 5.8 and 5.9. To detect agglomerates, we use three criteria: (i) the distance between particles must be smaller than the sum of their particle sizes, meaning they are in contact. (ii) the contact period between two colliding particles should last for at least 0.01 s. This set of criteria ensures that any particles in contact are indeed firmly agglomerated and not just in collision. (iii) for an agglomerate to be counted, it needs to contain at least 5 particles. Obviously, except the case when C = 0.417 at 800 °C, all the other sintering cases shows that the number of the agglomerates first increase to a very large number, indicating more and more agglomerates formed in the system. However, after a certain period, the number of agglomerates starts to decrease due to the merger between agglomerates, particularly for the cases when C = 1/1.251 at 1000 °C. For relatively

less strong sintering cases (C = 1/1.251 at 800 °C and C = 0.417 at 1000 °C), the total number of agglomerates is fluctuating after 1.5 s. This is because the bed is undergoing unstable fluidization, the agglomerates are forming and breaking all the time in the bed. Furthermore, the moment when the number of agglomerates collapses represents the time at which the bed starts to defluidize. Furthermore, as shown in Figure 5.9, for the smooth-surface model and nine-microcontact-point model at 800 °C and all the sintering cases at 1000 °C, in the end, almost all the particles are in agglomerates, which also matches with our observations from Figure 5.5.

Effects of the gas superficial velocity

Occurrence of defluidization is determined by the competition between the solid bridge force and the breakage force in the system. The drag force and the collision force together act as a breakage force between particles. Increasing the gas superficial velocity leads to the increase of the breakage force and reduces the contact time between particles. Therefore, it has the opportunity to reduce agglomeration. In order to study the effect of the gas velocity on the defluidization behavior, simulation cases are carried out for different gas superficial velocities, namely, 0.12 m/s, 0.16 m/s, and 0.32 m/s at 1000 °C, using two different amounts of sintering (i.e. C = 1 and C = 1.251).

Figure 5.10 shows the bed pressure drop profile versus the operating time and its standard deviation (STD). Note that the standard deviation is calculated from 1.5 till 10 seconds. The STD1 for the case with u_g = 0.16 m/s and C = 1.251 is calculated from 1.5 s to 4 s, and STD2 is obtained from 4 s to 10 s. Obviously, the standard deviation increases with the increase of the gas superficial velocity for both models, indicating that breakage delays formation of large agglomerates.

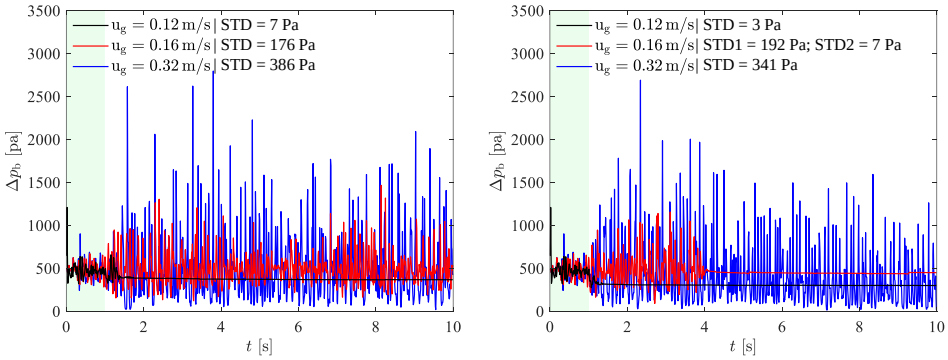

Figure 5.10: Effect of gas superficial velocity on bed pressure drop profile at 1000 °C. (a) smooth-surface model (C = 1); (b) nine-microcontact-point model (C = 1.251).

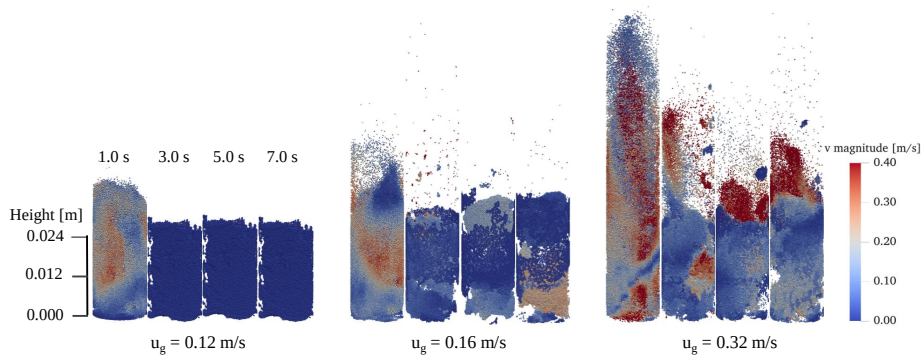

(a)

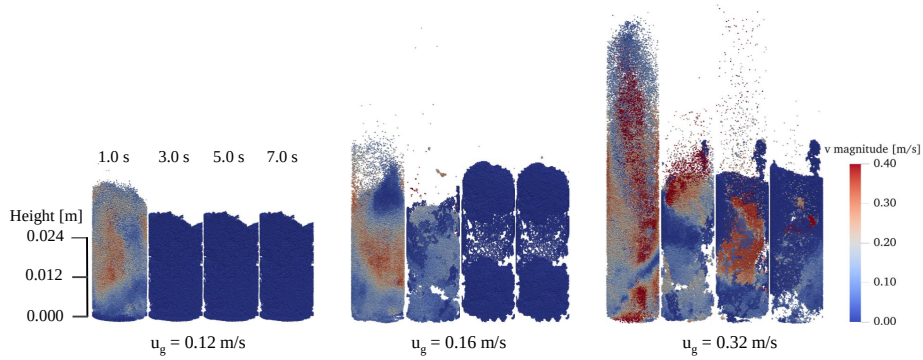

(b)

Figure 5.11: Effect of gas superficial velocity on bed structure and particle velocity distribution at 1000 °C. (a) smooth-surface model (C = 1); (b) nine-microcontact-point model (C = 1.251)

For more detailed information, instant snapshots of the bed structure and particle velocity distribution under three gas superficial velocities for both models at 1000 °C are shown in Figure 5.11. The particles are colored by the magnitude of their velocities. Obviously, for low gas superficial velocity cases (0.12 m/s), the entire bed quickly defluidizes for both cases, i.e., almost all particles are colored blue. For the smooth-surface model, with increasing the gas superficial velocity, clear agglomerates can still be found in the bed particularly when $u_g = 0.16\,m/s$. When further increasing the gas superficial velocity to 0.32 m/s, the bed looks more dynamic. For the nine-microcontact-point model, when increasing the gas superficial velocity to 0.16 m/s, the sintering region represented by the low velocity values concentrates in the bottom of the bed which lasts more than 3 s, after which the bed defluidizes. When further increasing the gas superficial velocity to 0.32 m/s, the rather healthy fluidization can last for a longer period. However, after 5 s, the sintering region from the bottom of the bed has spread to the entire bed, indicating a nearly completely defluidization. We can conclude from the results that higher gas superficial velocity

can increase the amount of gas passing through the bed in a certain period, which would cause large bubbles in the system and increase the collision frequency between particles. As a result, the contact time between colliding particles reduces, leading to a less strong solid bridge, which might postpone defluidization.

The discussion above is supported by the volume PDF distribution of particle velocity, which is shown in Figure 5.12. As can be seen in this figure, at low gas velocity ($u_g = 0.12\,m/s$), for all models, the particles velocity profile moves quickly to low values, indicating a sudden defluidization. With the increase of the gas superficial velocity, the particle velocity shifts slowly to low velocities for both sintering models. We do notice that at some instants, there exist some sharp peaks (i.e. when $t = 5.0$ s); this is because that at these moments, the agglomerate consists of a massive number of particles that move as one block. Additionally, for the case when applying the nine-microcontact-point sintering model, after 5.0 s, the particles velocity locates in a rather wide range, and several peaks can be noticed. This represents a very strong unstable flow behavior in the bed. Increasing the gas superficial velocity might partially break the agglomerate into a few fragments with different motions. However, since the sintering force is strong, agglomerates meet sooner or later, leading to permanent solid bridges.

Quantitative analysis of the agglomerate size can provide a clear insight in the agglomeration process. Figure 5.13 shows the normalized maximum agglomerate size vs. time. Note that the agglomerate size is normalized by the total number of particles in the bed system. As can be seen from the figure, the defluidization occurs suddenly in less than 0.1 s after activing the sintering force when $u_g = 0.12\,m/s$. Increasing the u_g to $0.16\,m/s$ has no effect for the nine-microcontact-point model case. When $u_g = 0.16\,m/s$ and C = 1, we do find that at some instants, the agglomerate size suddenly decreases. As discussed before, this is due to the unstable situation in the bed. Increasing the gas superficial velocity might break the big agglomerate into small fragments due to a higher drag/collision force. However, when those fragments meet each other at any later moment, permanent solid bridges will form again. Furthermore, the biggest agglomerate emerges later in the case when applying $u_g = 0.32\,m/s$ for both models. However, defluidization still occurs since a huge agglomerate containing more than about 80% particles is formed. From this point of view, increasing the gas superficial velocity in the tested region will hardly improve the fluidization. Future work requires focusing on the turbulent fluidization regimes to test whether it will improve the fluidization ability.

Based on the discussion above, we conclude that: an increase in the gas superficial velocity can decrease the rate of the formation of agglomerates, and therefore postpone defluidization. However, defluidization does not vanish within 10 seconds, even though the gas velocity is increased by a factor of 2.7. This result is consistent with our previous experimental findings in Chapter 2: temperature has the most pronounced influence on defluidization, while the gas superficial velocity is insensitive to defluidization. Therefore, further study of the iron/iron oxide particles at a higher gas superficial velocity, e.g., turbulent fluidized bed, may open new operation windows.

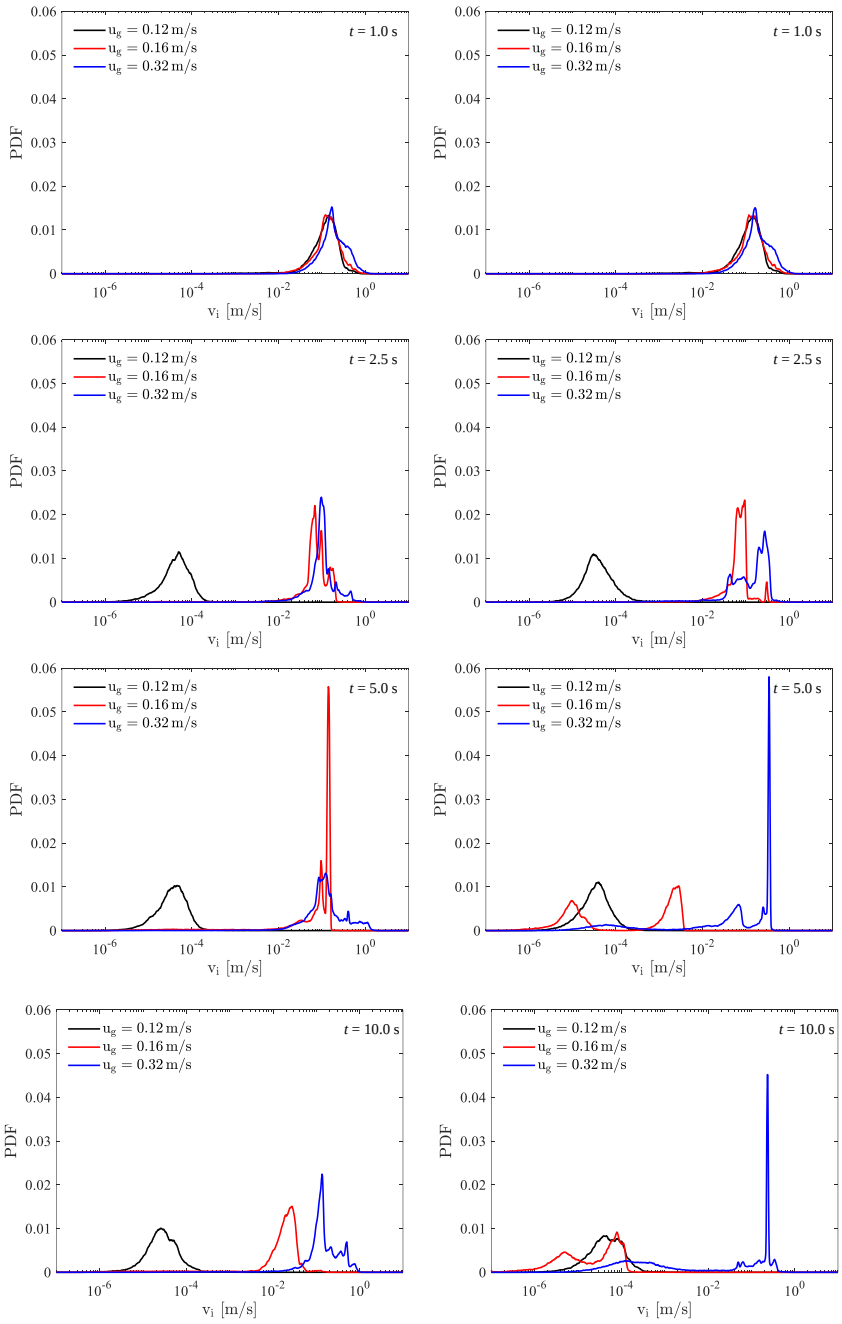

Figure 5.12: The number distribution of particle velocity when applying three kinds of gas superficial velocities for smooth-surface model and nine-contact-point model at temperature of 1000 °C at four instantaneous times.(a) smooth-surface model (C = 1); (b) nine-microcontact-point model (C = 1.251).

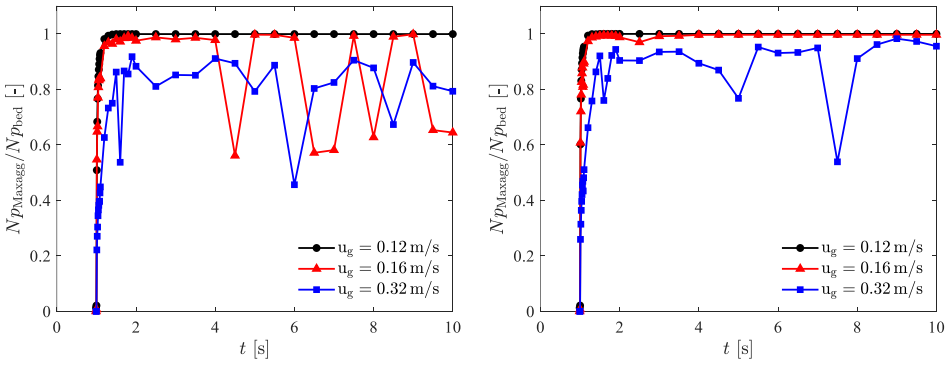

Figure 5.13: Normalized maximum agglomerate size in the bed over time at 1000 °C. (a) smooth-surface model (C = 1); (b) nine-microcontact-point model (C = 1.251).

5.5. Conclusions

The agglomeration/de-fluidization dynamics of combusted iron powders are numerically investigated in a fluidized bed at temperatures ranging from 500 – 1000 °C using a CFD-cgDEM method. The main conclusions include:

1. A coarse-grained method has been successfully extended to cohesive dense gas-solid flows by appropriate scaling of the temperature-dependent solid bridge (sintering) force.

2. The effect of particle sintering on the bed dynamics (agglomeration, de-fluidization) predicted from our model qualitatively agrees with our experiments. Temperature is a crucial parameter determining the strength of solid bridge, and thus the cohesiveness of the solid phase. While the gas superficial velocity within the studied range shows an insensitive effect on the defluidization behavior.

3. A simple scaling of 2.4/3 times of the solid bridge force using three-microcontact-point (C = 0.417) model to smooth surface/nine-microcontact-point (C = 1/1.251) model results in a significant change in fluidization behavior particularly at higher temperatures. For the combusted iron powder studied in this work, we found that the smooth-surface/nine-microcontact-point sintering force model represents better the realistic phenomena, and such model is suggested to be included in future chemical reaction studies (e.g. the reduction of the combusted iron fines).

Bibliography

[1] J. M. Bergthorson, S. Goroshin, M. J. Soo, P. Julien, J. Palecka, D. L. Frost, and D. J. Jarvis. “Direct combustion of recyclable metal fuels for zero-carbon heat and power”. In: *Applied Energy* 160 (2015), pp. 368–382.

[2] J. M. Bergthorson. “Recyclable metal fuels for clean and compact zero-carbon power”. In: *Progress in Energy and Combustion Science* 68 (2018), pp. 169–196.

[3] P. Julien and J. M. Bergthorson. “Enabling the metal fuel economy: green recycling of metal fuels”. In: *Sustainable Energy & Fuels* 1.3 (2017), pp. 615–625.

[4] D. Ning, Y. Shoshin, M. van Stiphout, J. van Oijen, G. Finotello, and P. de Goey. “Temperature and phase transitions of laser-ignited single iron particle”. In: *Combustion and Flame* 236 (2022), p. 111801.

[5] N. Poletaev and M. Khlebnikova. “Combustion of iron particles suspension in laminar premixed and diffusion flames”. In: *Combustion Science and Technology* 194.7 (2022), pp. 1356–1377.

[6] Y. Guo, K. Ren, A. Wei, C. Tao, W. Huang, P. Zhao, and D. Wu. “Iron dust explosion characteristics with small amount of nano-sized Fe2O3 and Fe3O4 particles”. In: *Fuel* 324 (2022), p. 124786.

[7] X. Liu, X. Zhang, J. Li, Q. Zhu, N. G. Deen, and Y. Tang. “Regeneration of iron fuel in fluidized beds Part II: reduction experiments”. In: *Powder Technology, (Accepted)* (2023).

[8] C. J. M. Hessels, T. A. M. Homan, N. G. Deen, and Y. Tang. “Reduction kinetics of combusted iron powder using hydrogen”. In: *Powder Technology* (2022), p. 117540.

[9] X. Liu, N. G. Deen, and Y. Tang. “On the treatment of bed-to-wall heat transfer in CFD-DEM simulations of gas-fluidized beds”. In: *Chemical Engineering Science* 236 (2021), p. 116492.

[10] P. Hartley, G. Parfitt, and L. Pollack. “The role of the van der Waals force in the agglomeration of powders containing submicron particles”. In: *Powder technology* 42.1 (1985), pp. 35–46.

[11] J. Staniforth. “Ordered mixing or spontaneous granulation?” In: *Powder technology* 45.1 (1985), pp. 73–77.

[12] K. Kuwagi, T. Mikami, and M. Horio. “Numerical simulation of metallic solid bridging particles in a fluidized bed at high temperature”. In: *Powder Technology* 109.1-3 (2000), pp. 27–40.

[13] J. Seville, C. Willett, and P. Knight. “Interparticle forces in fluidisation: a review”. In: *Powder Technology* 113.3 (2000), pp. 261–268.

[14] X. Liu, X. Zhang, J. Li, Q. Zhu, N. G. Deen, and Y. Tang. “Regeneration of iron fuel in fluidized beds Part I: defluidization experiments and theoretical prediction model”. In: *Powder Technology, (Accepted)* (2023).

[15] M. I. A. Barustan and S.-M. Jung. “Morphology of iron and agglomeration behaviour during reduction of iron oxide fines”. In: *Metals and Materials International* 25.4 (2019), pp. 1083–1097.

[16] J. Oh and D. Noh. “The reduction kinetics of hematite particles in H2 and CO atmospheres”. In: *Fuel* 196 (2017), pp. 144–153.

[17] Z. Mansourpour, N. Mostoufi, and R. Sotudeh-Gharebagh. “Investigating agglomeration phenomena in an air-polyethylene fluidized bed using DEM–CFD approach”. In: *Chemical Engineering Research and Design* 92.1 (2014), pp. 102–118.

[18] Z. Mansourpour, N. Mostoufi, and R. Sotudeh-Gharebagh. “A numerical study on agglomeration in high temperature fluidized beds”. In: *Journal of Chemical and Petroleum Engineering* 48.1 (2014), pp. 15–25.

[19] J. Tausendschön, J. Kolehmainen, S. Sundaresan, and S. Radl. “Coarse graining Euler-Lagrange simulations of cohesive particle fluidization”. In: *Powder Technology* 364 (2020), pp. 167–182.

[20] X. Chen and J. A. Elliott. “On the scaling law of JKR contact model for coarse-grained cohesive particles”. In: *Chemical Engineering Science* 227 (2020), p. 115906.

[21] M. Sakai, H. Takahashi, C. C. Pain, J.-P. Latham, and J. Xiang. “Study on a large-scale discrete element model for fine particles in a fluidized bed”. In: *Advanced Powder Technology* 23.5 (2012), pp. 673–681.

[22] H. G. Weller, G. Tabor, H. Jasak, and C. Fureby. “A tensorial approach to computational continuum mechanics using object-oriented techniques”. In: *Computers in physics* 12.6 (1998), pp. 620–631.

[23] C. Goniva, C. Kloss, N. G. Deen, J. A. Kuipers, and S. Pirker. “Influence of rolling friction on single spout fluidized bed simulation”. In: *Particuology* 10.5 (2012), pp. 582–591.

[24] R. Beetstra, M. A. van der Hoef, and J. Kuipers. “Drag force of intermediate Reynolds number flow past mono-and bidisperse arrays of spheres”. In: *AIChE journal* 53.2 (2007), pp. 489–501.

[25] C. Kloss, C. Goniva, A. Hager, S. Amberger, and S. Pirker. “Models, algorithms and validation for opensource DEM and CFD–DEM”. In: *Progress in Computational Fluid Dynamics, an International Journal* 12.2-3 (2012), pp. 140–152.

[26] P. A. Cundall and O. D. Strack. “A discrete numerical model for granular assemblies”. In: *geotechnique* 29.1 (1979), pp. 47–65.

[27] G. C. Kuczynski. “Self-diffusion in sintering of metallic particles”. In: *Sintering Key Papers*. Springer, 1990, pp. 509–527.

[28] P. Knight, J. Seville, H. Kamiya, and M. Horio. “Modelling of sintering of iron particles in high-temperature gas fluidisation”. In: *Chemical engineering science* 55.20 (2000), pp. 4783–4787.

[29] T. Mikami, H. Kamiya, and M. Horio. “The mechanism of defluidization of iron particles in a fluidized bed”. In: *Powder technology* 89.3 (1996), pp. 231–238.

[30] S. Radl, C. Radeke, J. G. Khinast, and S. Sundaresan. “Parcel-based approach for the simulation of gas-particle flows”. In: *8th International Conference on CFD in Oil & Gas, Metallurgical and Process Industries, Trondheim*. Vol. 23. 2011, pp. 1084–1098.

[31] Y. Hidaka, T. Anraku, and N. Otsuka. “Deformation of iron oxides upon tensile tests at 600–1250 C”. In: *Oxidation of Metals* 59.1 (2003), pp. 97–113.

[32] D. Chicot, J. Mendoza, A. Zaoui, G. Louis, V. Lepingle, F. Roudet, and J. Lesage. “Mechanical properties of magnetite (Fe3O4), hematite (α-Fe2O3) and goethite (α-FeO·OH) by instrumented indentation and molecular dynamics analysis”. In: *Materials Chemistry and Physics* 129.3 (2011), pp. 862–870.

[33] G. C. Hadjipanayis and R. W. Siegel. *Nanophase materials: Synthesis-properties-applications*. Vol. 260. Springer Science & Business Media, 2012.

[34] A. Atkinson and R. Taylor. “Diffusion of 55Fe in Fe2O3 single crystals”. In: *Journal of Physics and Chemistry of Solids* 46.4 (1985), pp. 469–475.

6

CONCLUSIONS AND RECOMMENDATIONS

6.1. Conclusions

This dissertation presents an experimental and numerical modeling study of the main phenomena and challenges in the regeneration of iron fuels in fluidized beds. The primary goal is to improve the reduction efficiency and ultimately close the iron fuel cycle. From this comprehensive study, the following main conclusions are drawn:

- Of the operational variables examined in this work, temperature and particle size have been shown to have the most pronounced influence on the agglomeration severity. This is characterized by two critical temperatures, i.e., the transition temperature (T_t) and the defluidiztaion temperature (T_d). Regarding the reduction performance, higher reduction rate/degree can be achieved by increasing the gas superficial velocities (particularly at a lower temperature) or increasing the reduction temperatures. However, such enhancement of the reduction rate/degree always hinders the further reduction process due to the early defluidization of the bed. In general, low-temperature reduction of the combusted iron powder is of great interest since a complete reduction to metallic iron can be achieved at 500 °C.

- Experimental measurements have been used to analyze the characteristics of reduced powder from the perspective of particle morphology and particle size changes. The reduction temperature shows an evident influence on the surface structure of the reduced particles. Specifically, the particles reduced at a higher temperature present rougher surfaces with larger pores, which provides a favorable condition for the formation of agglomerates. During reduction, the particle size first undergoes swelling (due to crystal transformation from Fe_2O_3 to Fe_3O_4 and disintegration of iron grains) and then shrinking (due to the densification of the newly produced metallic iron grains). Due to a nearly complete reduction at 500 °C the mean size of the final reduced powder is slightly smaller than the original oxides.

- By categorizing the existing treatments of the bed-to-wall heat transfer into two approaches (the thermal boundary condition approach and the particle-based conduction approach) and a detailed comparison of the sensitivity of the model-required parameters, our analysis shows that both approaches can well describe the bed-to-wall heat exchange in CFD-DEM simulations of fluidized beds if appropriate model parameters are employed. Since the performance of the particle-to-wall conduction model is almost insensitive to the changes of the model-required parameters, whereas the thermal boundary condition approach shows more dependency on parameter values as well as the grid resolution, we therefore recommend the particle-based model when simulating dense thermal gas-solid flows for e.g. fluidized bed applications.
- The coarse-grained method has been successfully extended to cohesive dense gas-solid flows with considering the temperature-dependent solid bridge (sintering) force. Temperature is a crucial parameter determining the strength of a solid bridge, while the gas superficial velocity within the studied range shows an insensitive effect on the occurrence of defluidization. For the combusted iron powder studied in this work, we found that the smooth-surface/nine-microcontact-point sintering force model represents better the actual sintering process, and such model is suggested to be included in further chemical reaction studies (e.g., the reduction of combusted iron fines).

To conclude, the experimental work focuses on how to optimize the operating parameters and particle size for the fluidization and reduction process. The numerical work fills in two gaps: 1) how to better model the particle-to-wall heat transfer; 2) a methodology for modeling micron-sized combusted iron sintering. These findings contribute to the regeneration stage of the iron fuel cycle and bring new insights to dense energy carrier research for future storage and transport of renewable energy.

6.2. Recommendations

In this work, we comprehensively discussed the challenges and phenomena associated with the hydrogen-based regeneration of iron fuels. Many important questions regarding the reduction process remain unanswered, which is recommended for future study; these include:

- Strategies need to be explored to counteract the sintering issue, e.g, from the perspective of reactor geometry (e.g. conical fluidized bed and/or rotary drum), fluidization regimes (e.g. turbulent fluidized beds), adding inactive particles, particle coating/doping, and optimizing the operating conditions (e.g. temperature/velocity/pressure). As such, a good/stable fluidization behavior may be achieved during the entire reduction process.
- In this work, we found that a nearly full conversion can be achieved at 500 °C. However, the reduction kinetics has not been comprehensively analyzed. To further analyze the reduction performance and obtain the reduction kinetics, it is suggested to carry out more quantitative measurements of the porosity via the Brunauer-Emmett-Teller (BET) method, in-situ phase transition and (off-)gas concentration.

- Research up to now has mainly focused either exclusively on combustion or on regeneration. However, investigations of multiple combustion-regeneration cycles are crucial for well establishing the knowledge of iron as recyclable fuel. Thus, cyclic experiments are recommended to be carried out to look into the entire efficiency and powder stability for both combustion and regeneration. Additionally, the morphology and the particle size change are also of great interest since they directly influence the subsequent combustion or regeneration steps in the iron fuel cycle.
- In this work, we have validated the coarse-grained method using experimental results from a lab-scale fluidized bed. It is also of great importance to developing a systematical modeling methodology to simulate the reduction. This requires extending the current model to include the chemical reaction kinetics (e.g. the reduction of the combusted iron fines). With such a model, the behavior towards the regeneration of iron fuel can be described, and ultimately the model can be coupled with the combustion modeling approach to represent the entire iron cycle in a realistic manner.

A

SUPPLEMENTARY OF CHAPTER 2

Fluidization regime of reduced iron

Our previous study shows that the fast defluidization temperature of the iron oxides usually occurs at a relatively higher temperature. However, we find that during the reduction process defluidization can occur at a relatively lower temperature (around 500 °C). It is known that defluidization behavior during the reduction process is due to the emergence of the iron on the outer surface of the particle. In order to further investigate the exact temperatures of the sticking of the iron powders, we have collected the produced samples with the reduction degree higher than 90% and conduct the fluidization experiments. Figure A.1 shows the typical pressure drop curve against the bed temperature for all size particles. It can be seen that for all size particles, defluidization occurs at the temperature in the range of 500 °C to 550 °C. Additionally, the pressure drop starts to decrease when the temperature is higher than 400 °C, indicating the particle becomes sticky at this point. Further increase the temperature or reaction time would cause a fully defluidzation behavior. Based on this, the emergence of the iron is indeed one of the important reasons to result in the sticking problem during the reduction process. Specifically, the surface structure of the newly formed fresh iron is crucial to the sticking behavior. From the results shown in the SEM image from Chapter 3, we found that during the reduction, particles surface becomes more porous. This would increase the roughness of the surface and form small iron grains. Such small iron grains exhibit lower melting points, and therefore leading to a lower Tamman temperature.

A

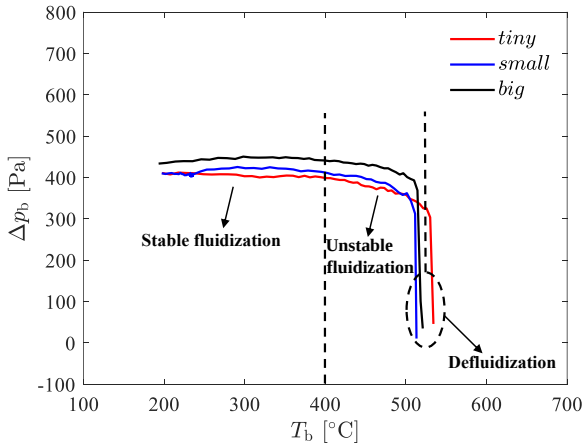

Figure A.1: The bed pressure drop against the bed temperature with $u_g = 4u_{mf}$ for reduced iron powder.

B

SUPPLEMENTARY OF CHAPTER 4

Near-wall particle temperature distribution

A quantitative analysis of the effect of the confining walls on the instantaneous particle temperature distribution in the near-wall region is presented by examining the PDF obtained from two approaches. Figure B.1 shows the PDF of the particles in the first/last layers of cells close to the front/back wall at time 3 s, 6 s, and 9 s. It is found that PDF data of the particles near the front/back walls based on the PW model include a slightly broader temperature range, especially at low temperatures, whereas for the tBC model, it includes a relative narrow temperature range. As discussed previously, for PW model, an extra heat flux is acting on those particles with particle-wall distance smaller than the thickness of the lens due to the particle-wall temperature difference. Therefore, particles in the very near-wall region cool down faster than those in the bed because the above-mentioned particle-fluid-wall conduction heat transfer. Moreover, the curve of PDF results with the tBC approach looks more symmetrical since the tBC approach imposes the heat loss through the walls on all the particles locating in the near-wall cells.

Verification of the particle-fluid-wall indirect conduction model

To verify the correct implementation of the particle-fluid-wall indirect conduction model, a single particle model is firstly numerically conducted and the results are compared with the analytical solution. Three verification cases are carried out to verify the implementation of the particle-fluid-wall indirect conduction model, i.e., case 2, case 3/4, and case 5 in Figure 4.2. The particle and fluid parameters used in the verification cases are the same as in the simulation parameters section. The particle-fluid-wall indirect conduction heat transfer for each case is verified with a single hot particle (363.15 K) and a cold wall with a constant temperature (293.15 K).

We first verify case 2, i.e., when the bottom of the gas layer is in contact with the wall but the particle-wall separation distance is larger than the minimum conduction region. In this case, the particle is cooling down due to the particle-fluid-wall heat transfer until reaching a steady temperature. The particle-fluid-wall indirect conduction heat transfer

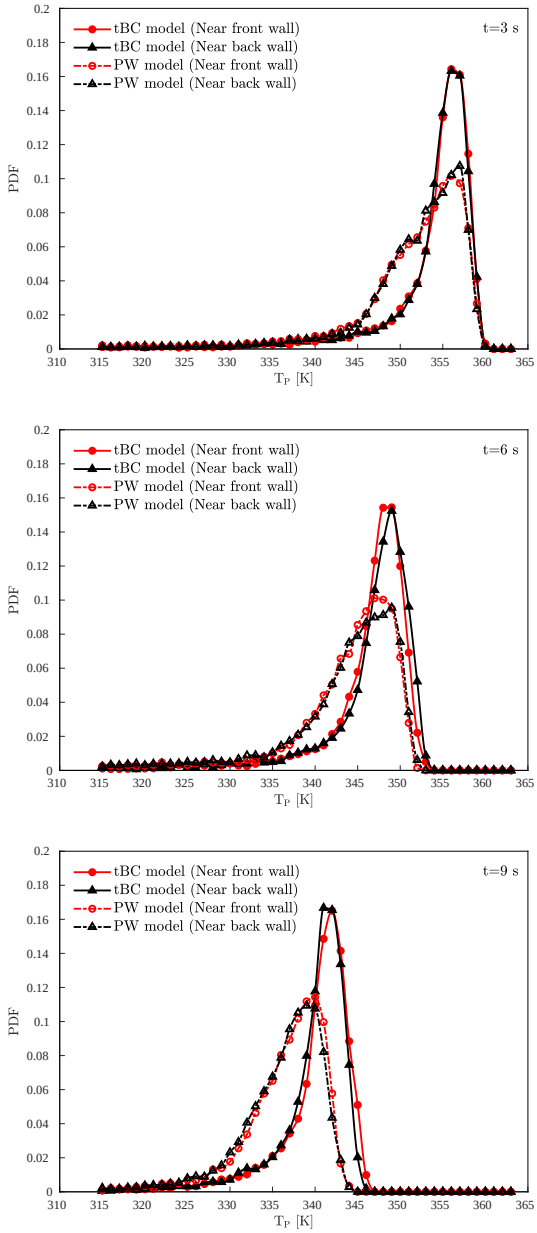

Figure B.1: Particle temperature PDF calculated from the particles in the first/last layers of cells close to the front/back walls at three instantaneous times.

in this case can be described by a one-dimensional unsteady heat conduction equation:

$$m_i C_{p,i} \frac{dT_{p,i}}{dt} = 2\pi k_f \left(T_w - T_{p,i}\right) \int_0^{r_{out}} \frac{r}{l} dr \tag{B.1}$$

The analytical solution can be easily obtained by solving the above differential equation. The CFD-DEM results are compared with the analytical solution with an overlap displacement from $0.002r_p$ to $0.02r_p$, which is shown in Figure B.2. The dimensionless temperature in Figure B.2 is defined as the difference of the particle current and initial temperature, divided by the difference of wall temperature and the particle initial temperature ($T_p - T_{p,0} / T_w - T_{p,0}$). As evident from Figure B.2, a good agreement between the numerical results and the analytical solution is obtained for case 2. The temperature of the particle gradually converges to a fixed value due to the indirect conduction heat flux. Moreover, the slope of the dimensionless temperature profile becomes steeper with the decrease of the overlap displacement, demonstrating the increase of indirect heat flux.

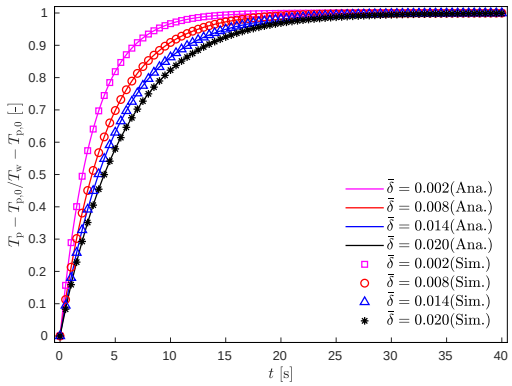

Figure B.2: Comparison of analytical solution and CFD-DEM simulation results of the dimensionless temperature for case 2 as a function of time.

Next case 3/4 and case 5 are verified, see Figure 4.2. In case 3/4 the bottom of the particle surface is inside the minimum conduction region but not in contact with the wall or just touches the wall, whereas in case 5 the particle is overlapping with the wall surface. Similarly, the indirect conduction heat transfer between the particle and the wall for case 3/4 and 5 can be expressed as eqs. (B.2) and (B.3), and the analytical solution is obtained in a similar way as for case 2:

$$m_i C_{p,i} \frac{dT_{p,i}}{dt} = 2\pi k_f \left(T_w - T_{p,i}\right) \left(\int_0^{r_{in}} \frac{r}{s} dr + \int_{r_{in}}^{r_{out}} \frac{r}{l} dr \right) \tag{B.2}$$

$$m_i C_{p,i} \frac{dT_{p,i}}{dt} = 2\pi k_f \left(T_w - T_{p,i}\right) \left(\int_{r_s}^{r_{in}} \frac{r}{s} dr + \int_{r_{in}}^{r_{out}} \frac{r}{l} dr \right) \tag{B.3}$$

The simulation results and analytical solutions for the particle-fluid-particle indirect conduction procedures are shown in Figures B.3 and B.4. It is observed that both cases are consistent at every overlap displacement. The dimensionless particle temperature

reaches 1 for a physical time of about 15 s for both cases. Interestingly, when the bottom of the particle is within the minimum distance region or in contact with the wall, the overlap displacement has almost no influence on the particle temperature evolution. This is because the variation of overlap displacement has little effect on the integration limit in eqs. (B.2) and (B.3) when the value of displacement approaches to zero or becomes negative.

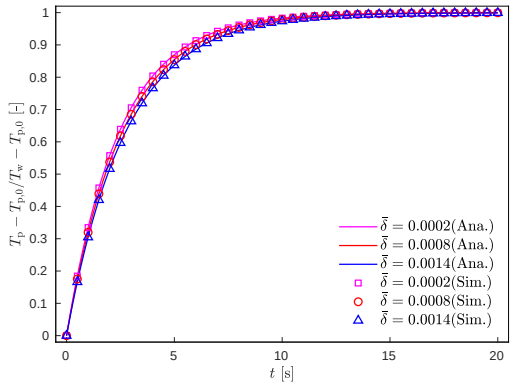

Figure B.3: Comparison of analytical solution and CFD-DEM simulation results of the dimensionless temperature for case 3/4 as a function of time.

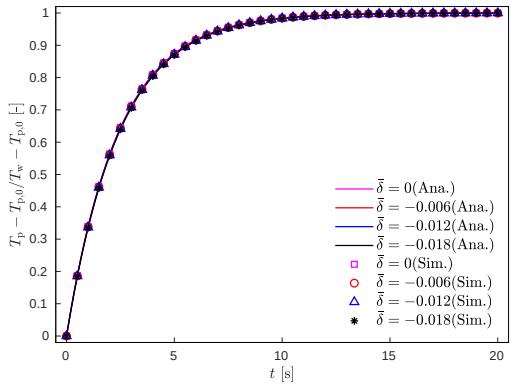

Figure B.4: Comparison of analytical solution and CFD-DEM simulation results of the dimensionless temperature for case 5 as a function of time.

Verification of the particle-wall direct conduction model

Similarly, the implementation of the particle-wall direct conduction model is verified in the same condition as the particle-fluid-wall conduction model. A single hot particle (363.15 K) is cooling down due to the contact with the cold aluminum wall (293.15 K).

The direct particle-wall conduction heat transfer can be expressed by a one-dimensional unsteady heat conduction equation:

$$m_i C_{p,i} \frac{dT_{p,i}}{dt} = \frac{4k_{p,i}k_{p,\mathrm{w}}}{k_{p,i}+k_{p,\mathrm{w}}} R_c^{'}(T_\mathrm{w} - T_{p,i}) \tag{B.4}$$

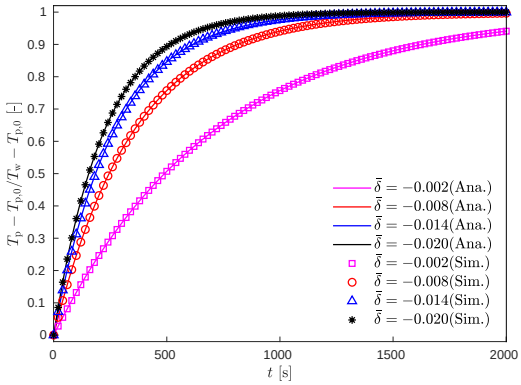

Figure B.5: Comparison of analytical solution and CFD-DEM simulation results of the dimensionless temperature for direct PW conduction model.

The analytical solution and CFD-DEM results are compared for various overlap displacements from -0.002r_p to -0.02r_p. The results are shown in Figure B.5. It is observed that the numerical results match very well with the analytical solution. Moreover, the effect of the overlap displacement becomes smaller as it increases. Additionally, the particle-wall direct conduction heat flux increases since the slope of the dimensionless temperature profile becomes steeper.

Acknowledgements

"Knowing yourself is the beginning of all wisdom."
—Aristotle

By starting to write this part, I am on the tail-end of my Ph.D. journey. I choose to write this part on the last day of 2022 since every year at this moment I recap things that have happened over the past year/years. And I do think acknowledgments are more or less like a 4-year-end review/recap. Looking back on this journey, it is all of the support of colleagues, friends, and families that make it possible. Here, I would like to express my sincere thanks to all of them.

The completion of this thesis could not have been possible without the help and guidance of my supervisor, **Niels**. I am extremely grateful for your patience, guidance, and support. Your immense knowledge and plentiful experience have encouraged me throughout my academic research and daily life. Moving to the Netherlands is a big change in my life. It took a long time for me to fit in. You could always notice the awkward situation I was in and tried to make me involved in the conversation and play jokes with me. Whenever I am stressed out, you would always help me lighten the burden. Every year on my birthday you always wish me a happy birthday even though it was on weekend. All of what you did to me really makes me braver and gives me the courage to speak up. I still remember those words you told me when I came back from China. You said to me that I should always speak up and take initiative when I thought I could benefit from it. Using your words, it would be "Put you at the top priority and think how you would make use of it the best way". Later, I did use such "principle" in many things, and they all worked very well. You make me realize that whom you are working with is more important than what you are working on.

I would like to express my gratitude to my daily supervisor **Yali** for the consistent support and guidance during my research. I have benefited greatly from your expertise, professional writing, and presentation skills. You are always there when I most need you. During the final stages of my Ph.D., we discussed more frequently just to make sure that I was on track with my research. Your dedication and involvement in every step of my research can always steer me in the right direction. I feel so lucky to be working with you on this project. You always asked me if I needed any help, and invited us to your house to have hotpots. Your thoughtfulness means a lot to me. It is your continuous encouragement, support, and care that allows me to live and work happily in the Netherlands.

In early 2020, we collaborated with Institute of Process Engineering (IPE), Chinese Academy of Sciences. I would also like to extend my gratitude to **prof. Qingshan zhu** for providing us with support for conducting experiments. Thanks to **prof. Jun Li**, and **Xu Zhang** for valuable discussion and feedback throughout the time when I did my experiments. Those experiments would not go smoothly without your expertise. Thanks to **Xue Wang** for helping me with my work and life during the period when I was in Beijing.

I would like to express my deepest appreciation to my committee members **prof.dr. Yurong He, Prof. Dr.-Ing. habil. Stefan Heinrich, Prof. Dr. Stefan Pirker, prof.dr.ir. Martin van Sint Annaland** for their thoughtful comments and recommendations on this dissertation. Thank you all for your valuable time in reviewing this thesis and participating in the defense ceremony.

I also sincerely acknowledge **Giulia** and **Tess** for your insightful comments and suggestions in our progress meeting. I would like to thank all members of **Metal Meet** for the valuable discussion on this project. Special thanks to **Niek** for providing the combusted powder for this research. My gratitude also goes to **Marjan** and **Linda** for their work in helping me with my work and life in the Netherlands.

From September 2018 to March 2020, I worked in office Gemini Noord 1.21. Thanks to my office mates from Gemini Noord 1.21, **Aromal**, **Shuli**, **Denis**, **Thijs**, **Chih-Chia**, **Conrad**, **Ravi**, **Pourya**, **Camila**, and **Robin**. I was so lucky to stay in such a nice office with you. Our office was always full of laughter, jokes, and discussions. I always call this office "party office" that is because I had a great time there. In early 2020, we could only work from home, and we still kept having online office chats every week. All of this made me feel we were still working together.

Thanks to all the intervision members, **Chih-chia**, **Conrad**, **Rahul**, **Aled**, **Akmal**, **Faeze**, **Xiaowei**, **Weidong**, **Tianqi**, **Camila**, **Qingrui**, **Dennis**, **Peter**, **Nicole**, and of course **Yali** and **Niels**. During the meeting, we talked about food, culture, research, and played games. We shared updates, brainstormed new ideas, asked for feedback, and built team relationships. All of these made me feel I was not working or staying alone. I really appreciate the happy lunchtime we have had.

Thanks to my Sunday party, movie party, Charlie's Angels girls, and board game and dumpling party members, **Ravi**, **Conrad**, **Abhijit**, **Helen**, **Vertika**, and **Nicole**. Especially **Nicole**, you are an amazing organizer! I really enjoyed the time I spent with all of you. Christmas market we visited. Card games we played. Dumplings we made together, and dinner we had outside/at home. These are all my precious memories. Thanks to my Chinese friends and colleagues, **Haiyu**, **Lingjie**, **Shuli**, **Jinlin**, **Hesheng**, **Weijie**, **Xi**, **Changliang**, **Tianqi**, **Qingrui**, **Weidong**, **Daoguan**, **Xiaowei**, **Yalin**, **Zhongcheng**, **Xiaocheng**, **Boyan**, **Huibo**, **Hao**, and **Xiaoxing**. There are lots of good memories with you of having hotpots and hanging out together. All of you made my life in the Netherlands more wonderful. Thanks to my friends and neighbors, **Lu**, **Tao**, **Mengting**, and **Xuan** for helping me move and taking care of me when I was sick. Thanks to my friends outside of the Netherlands, **Yun** and **Jiahuan** for always thinking of me and always being there when I want to talk.

Getting through this thesis required more than academic support, and I have many people to thank for listening to and having to tolerate me during all the ups and downs over the past years. Special thanks go to four colleagues and friends. Thanks to **Camila**. You are always willing to help me whenever I need it. I still remember those days when I struggled with the heat transfer problem in my research. You always came to me and discussed it with me, even for the whole day. Your dedication to helping others is truly inspiring, and it has helped me realize that helping others is life's greatest happiness and joy. I am so grateful to have you as a friend. Thanks to **Conrad**. We are not only colleagues or project partners but also friends. You make me feel sharing is truly caring. Your help is not only in sharing your thoughts and opinions on my research in "our" meetings but also in giving me advice on life-wise decisions. Thanks for giving me a one-day tour of

your farm. That was my first experience visiting a dutch village and farm, and it will be a precious memory for me. Thanks to **Ravi**. You have always been helpful. I really appreciate all the help you have given me, especially with shipping my experimental material to China. Your positive attitude and joy for life are truly infectious. It's rare to find someone who can take the best parts of their childhood and apply them to adulthood in such a natural way. Your optimistic mindset lets me know everything is temporary and will eventually work out for the best. **Vertika**, since September 2021, we started working in the same office. Since then I am working in a happy mood every day. I really enjoyed all the fantastic dinners/outings/movie nights we had together. Thank you for always surprising me on my birthday. I will always remember those memorable days and look forward to exploring more with you. You are such a strong and independent person who consistently inspires me to be fearless and take chances. You make me realize that being a strong girl is amazing!

In November 2022, I had the opportunity to work as a postdoctoral researcher in the Power and Flow group. Thanks to **Rob** for bringing me to the new field at the end of my Ph.D. research. Thanks to **Nithin** for your patience to share your knowledge with a non-combustion person. I will always remember the Christmas party we had together this year.

No words can express how thankful and grateful I am for having you, my caring, supportive boyfriend, **Xinsheng** (新升) . Thanks for giving me company, encouragement, and support over the past nine years. You have always been proud of even the smallest achievements in my life. Because of your encouragement and support, I decided to pursue Ph.D. abroad. I am very surprised that you could always find a way to stretch my thinking, development, and capabilities. Thanks for helping me keep being better. It is your unconditional love, care, and tolerance that made the hardship of this Ph.D. journey worthwhile. Your positive attitude, and desire to try new things and make a meaningful contribution to your field keep inspiring me. Thank you for motivating me throughout this endeavor! Thank you for enlightening my present and future!

Finally, I would like to give my deepest gratitude to my families: 爸爸，妈妈，哥哥，嫂嫂。感谢你们**,** 无论我做出什么样的决定，你们总是无条件的支持我。是你们一直以来的鼓励，支持和包容，才让我的求学之路没有那么艰辛。是你们的爱让我更加勇敢与坚定！我爱你们！

Xin Liu
Eindhoven, 31-12-2022

About the author

Xin Liu was born on the 20th of November, 1992 in Xi'an, China. From 2011 to 2015, she studied Chemical Engineering in Northwestern University in Xi'an, China. She was awarded National Scholarship in 2013 and university scholarship for four years in a row. When she completed her bachelor study in 2015, she obtained excellent graduate student and was recommended for admission to State Key Laboratory of Multiphase Flow in Power Engineering at Xi'an Jiaotong University. Upon completing her master degree with a thesis titled "Investigation on Heat Transfer and Flow Characteristics of Air Crossing Serrated Spiral Finned Tube Bundles" in 2018, she moved to the Netherlands to start her PhD in the Mechanical Engineering Department at Eindhoven University of Technology. Her Ph.D. project, "Regeneration of iron fuel", which is presented in this thesis, included both experimental study and numerical modeling. The experimental work collaborated with Institute of Process Engineering, Chinese Academy of Sciences from January to June 2021. From December 2022, she works as a postdoctoral researcher in the Power & Flow group at Eindhoven University of Technology under the supervision of Dr. R.J.M. Bastiaans. She works on numerical modeling of ammonia combustion.

List of Publications

Journals

[1] **X. Liu**, N. G. Deen, Y. Tang. On the treatment of bed-to-wall heat transfer in CFD-DEM simulations of gas-fluidized beds. Chemical Engineering Science, 2021, 236: 116492.

[2] **X. Liu**, X. Zhang, J. Li, Q. Zhu, N. G. Deen, Y. Tang. Regeneration of iron fuel in fluidized beds Part I: Defluidization experiments and theoretical prediction model. Powder Technology, 2023. (Accepted)

[3] **X. Liu**, X. Zhang, J. Li, Q. Zhu, N. G. Deen, Y. Tang. Regeneration of iron fuel in fluidized beds Part II: Reduction experiments. Powder Technology, 2023, https://doi.org/10.1016/j.powtec.2022.118183.

[4] **X. Liu**, C. J. M. Hessels, N. G. Deen, Y. Tang. CFD-DEM investigation on the (de-)fluidization behavior of combusted iron fines in a fluidized bed. Fuel, 2023. (Under review)

Conferences

Oral presentations

[1] **X. Liu**, N. G. Deen, Y. Tang. Investigating the (de-)fluidization behavior of combusted iron fines in a fluidized bed using coupled CFD-DEM. The 11th International Conference on Multiphase Flow (ICMF 2023), Kobe, Japan. April 2023.

[2] **X. Liu**, N. G. Deen, Y. Tang. CFD-DEM Investigation on the Reduction Behaviour of Combusted Iron Fines in a Fluidized Bed. The 17th OpenFOAM Workshop, Cambridge, UK. July 2022.

[3] **X. Liu**, X. Zhang, J. Li et al. Experimental study of regeneration of iron fuel using hydrogen in a lab-scale fluidized bed. The 1st International Workshop on Reacting Particle-Gas Systems, Bochum Germany. June 2022.

[4] **X. Liu**, N. G. Deen, Y. Tang. CFD-DEM investigation on the (de-)fluidization behavior of combusted iron fines in a fluidized bed. The 24th International Conference on Fluidized Bed Conversion, Gothenburg, Sweden. May 2022.

[5] **X. Liu**, N. G. Deen, Y. Tang. Investigation on the agglomeration behavior of iron particles in a fluidized bed at high temperature. The VII International Conference on Particle-Based Methods (PARTICLES 2021), Hamburg, Germany. October 2021.

[6] **X. Liu**, Y. Tang, N. G. Deen. The treatment method of bed-to-wall heat transfer in a fluidized bed using CFD-DEM method. The 14th International Conference on Computational Fluid Dynamics In the Oil & Gas, Metallurgical and Process Industries, Trondheim, Norway. October 2020.

[7] **X. Liu**, C. J. M. Hessels, N. G. Deen, Y. Tang. Regenerating iron for carbon-free energy storage, The Netherlands Process Technology Symposium (NPS16), Eindhoven, the Netherlands. September 2019. (dual oral presentation X. Liu and C. J. M. Hessels).

Poster presentations

[1] **X. Liu**, N. G. Deen, Y. Tang. Investigating the (de-)fluidization behavior of combusted iron fines in a fluidized bed, The Combura Symposium, Soesterberg, the Netherlands. November 2022. (First Poster Prize)

[2] **X. Liu**, N. G. Deen, Y. Tang. Regeneration of iron fuel in Fluidized Beds, The 1st Workshop on Metal-enabled Cycle of Renewable Energy (MECRE), Eindhoven, the Netherlands. October 2022.